Star formation in nearby early-type galaxies: the radio continuum perspective

Kristina Nyland, Lisa M. Young, Wrobel Joan, Timothy A. Davis, Martin Bureau, Katherine Alatalo, Raffaella Morganti, Pierre-Alain Duc, P.T. de Zeeuw, Richard M. Mcdermid, et al.

Monthly Notices
of the
ROYAL ASTRONOMICAL SOCIETY

MNRAS **464,** 1029–1064 (2017)
Advance Access publication 2016 September 22

doi:10.1093/mnras/stw2385

Star formation in nearby early-type galaxies: the radio continuum perspective

Kristina Nyland,[1,2★] Lisa M. Young,[3] Joan M. Wrobel,[4] Timothy A. Davis,[5] Martin Bureau,[6] Katherine Alatalo,[7†] Raffaella Morganti,[2,8] Pierre-Alain Duc,[9] P. T. de Zeeuw,[10,11] Richard M. McDermid,[12,13] Alison F. Crocker[14] and Tom Oosterloo[2,8]

Affiliations are listed at the end of the paper

Accepted 2016 September 21. Received 2016 September 14; in original form 2016 April 15

ABSTRACT

We present a 1.4 GHz Karl G. Jansky Very Large Array (VLA) study of a sample of early-type galaxies (ETGs) from the ATLAS^{3D} survey. The radio morphologies of these ETGs at a resolution of $\theta_{\rm FWHM} \approx 5$ arcsec include sources that are compact on sub-kpc scales, resolved structures similar to those seen in star-forming spiral galaxies, and kpc-scale radio jets/lobes associated with active nuclei. We compare the radio, CO, and infrared (IR) properties of these ETGs. The most CO-rich ETGs have radio luminosities consistent with extrapolations from H_2 mass derived star-formation rates from studies of late-type galaxies. These ETGs also follow the radio–IR correlation. However, ETGs with lower molecular gas masses tend to have less radio emission relative to their CO and IR emission compared to spirals. The fraction of galaxies in our sample with high IR-radio ratios is much higher than in previous studies, and cannot be explained by a systematic underestimation of the radio luminosity due to the presence extended, low-surface-brightness emission that was resolved out in our VLA observations. We find that the high IR-radio ratios tend to occur at low IR luminosities, but are not associated with low dynamical mass or metallicity. Thus, we have identified a population of ETGs that have a genuine shortfall of radio emission relative to both their IR and CO emission. A number of mechanisms may cause this deficiency, including a bottom-heavy stellar initial mass function, weak magnetic fields, a higher prevalence of environmental effects compared to spirals, and enhanced cosmic ray losses.

Key words: galaxies: elliptical and lenticular, cD – galaxies: star formation – radio continuum: galaxies.

1 INTRODUCTION AND MOTIVATION

Early-type (elliptical and lenticular) galaxies (ETGs) were once considered a homogeneous class of 'red and dead' systems devoid of cold gas and young stars, archetypes of the end point of hierarchical galaxy formation and evolution. However, evidence is mounting that a significant fraction of nearby ETGs are in fact still continuing to form stars. We now know that ETGs commonly host neutral hydrogen (H I) distributed in discs, rings, or disturbed structures, with masses ranging from $\sim 10^6$ to 10^8 $M_\odot$ (e.g. Morganti et al. 2006; Oosterloo et al. 2010). Recent statistical searches for H I have reported detection rates of ∼40 per cent in field ETGs, and ∼10 per cent in ETGs in more densely populated environments (Serra et al. 2014).

In addition to cold atomic gas, CO studies have found that many ETGs also harbour substantial reservoirs of molecular gas (e.g. Knapp & Rupen 1996; Welch & Sage 2003; Combes, Young & Bureau 2007). Recently, the first statistically complete single-dish CO survey of molecular gas in the ATLAS^{3D} galaxies quantified the prevalence of a molecular gas in ETGs, reporting a detection rate of 22 ± 3 per cent (Young et al. 2011). Interferometric molecular gas imaging studies have shown that ETG molecular gas reservoirs span a range of diverse morphologies and kinematics (Young, Bureau & Cappellari 2008; Crocker et al. 2011; Alatalo et al. 2013; Davis et al. 2013). While secular processes such as stellar mass-loss from asymptotic giant branch (AGB) or post-asymptotic giant branch (pAGB) stars may be responsible for the presence of the molecular gas in ETGs in some cases (Faber & Gallagher 1976;

★ E-mail: knyland@nrao.edu
† Hubble fellow.

Knapp, Gunn & Wynn-Williams 1992; Mathews & Brighenti 2003; Temi, Brighenti & Mathews 2007), the disturbed morphologies and kinematics of the gas in other cases point to an external origin (i.e. mergers; Sarzi et al. 2006; Young et al. 2008; Davis et al. 2011; Duc et al. 2015; Davis & Bureau 2016). Other authors have suggested that molecular gas in massive ETGs galaxies may originate from cooled gas from the hot X-ray haloes in which these galaxies typically reside (Werner et al. 2014).

While it has become clear that many ETGs contain significant cold gas reservoirs, the ultimate fate of this gas has remained a subject of debate. Whether the gas is actively engaged in star formation (SF), and the efficiency of that SF compared to spiral galaxies, is still unclear. The difficultly in addressing these questions largely arises from the fact that common SF tracers, such as ultraviolet (UV) and infrared (IR) emission, may be contaminated by emission from the underlying evolved stellar population in ETGs (Jeong et al. 2009; Temi, Brighenti & Mathews 2009; Sarzi et al. 2010; Davis et al. 2014). Emission from active galactic nuclei (AGNs) in ETGs can also contaminate many standard SF tracers.

Nevertheless, recent studies have argued in favour of the presence of ongoing SF in ETGs. The detection of young stellar populations through UV observations with the *Galaxy Evolution Explorer* and the *Hubble Space Telescope*, especially in gas-rich ETGs, has provided support for this scenario (Yi et al. 2005; Kaviraj et al. 2007; Ford & Bregman 2013). The UV emission re-processed by dust in star-forming galaxies and re-emitted in the IR provides another avenue for SF studies of ETGs, and is less susceptible to dust extinction compared to star-formation rate (SFR) tracers at shorter wavelengths. Although the possibility of contamination from old stars complicates the use of IR emission as an SFR tracer in ETGs, techniques for isolating the portion of IR emission associated with SF have shown promising results (e.g. Davis et al. 2014).

Another potential ETG SFR tracer is radio continuum emission. Unlike other tracers, such as optical or UV emission, centimetre-wave radio continuum emission is virtually unaffected by extinction or obscuration (Condon 1992). Recent upgrades at the Karl G. Jansky Very Large Array (VLA) offer the ability to obtain sensitive measurements over relatively short timespans, making radio continuum observations an efficient mean of detecting even weak SF in ETGs. Although radio continuum emission may be contaminated by AGNs, strong AGNs can be readily identified based on their radio morphologies (e.g. Wrobel & Heeschen 1991) and through comparisons with other SF and AGN diagnostics (e.g. Nyland et al. 2016).

Radio continuum emission is well established as an SF tracer in late-type galaxies. Studies of the relationship between radio continuum and IR emission have demonstrated a tight correlation between these two quantities, which extends over at least three orders of magnitude among "normal" star-forming galaxies (e.g. Helou, Soifer & Rowan-Robinson 1985; Condon 1992; Yun, Reddy & Condon 2001). This so-called 'radio-IR' relation is believed to be driven by SF in the host galaxy. The radio continuum emission is generated by massive stars as they end their lives as supernovae, accelerating cosmic rays and subsequently producing non-thermal synchrotron emission. Dusty H II regions in turn re-radiate optical and UV light emitted by young stars at IR wavelengths.

Numerous studies of the radio-IR relation for samples of star-forming spiral galaxies using IR data at both far-infrared (FIR) and mid-infrared (MIR) wavelengths (e.g. Yun et al. 2001; Condon, Cotton & Broderick 2002; Appleton et al. 2004; Sargent et al. 2010) have been performed. However, detailed studies of the radio-IR correlation in ETGs have been rare. Some authors have reported that ETGs closely follow the same tight radio-IR correlation as spiral galaxies (Walsh et al. 1989; Combes et al. 2007), while others have found that ETGs as a class tend to be systematically 'radio faint' (Wrobel & Heeschen 1991; Lucero & Young 2007; Crocker et al. 2011). A large, sensitive study of the radio continuum emission on kpc-scales of a statistical sample of ETGs is therefore needed to improve our understanding of the incidence and efficiency of SF in bulge-dominated galaxies.

Here, we present new 1.4 GHz VLA observations at 5 arcsec spatial resolution of a subset of the statistically complete ATLAS^{3D} survey. We combine these new VLA data with existing archival 1.4 GHz measurements to study the global relationship between the radio continuum and IR emission in ETGs. We also compare the radio continuum emission properties to those of the molecular gas in our sample galaxies, all of which have single-dish CO observations available, to study the star formation efficiency (SFE) in ETGs. In Section 2, we describe the ATLAS^{3D} survey. We explain the selection, observations, data reduction, and results of our new VLA observations in Section 3. Ancillary molecular and IR data are discussed in Section 4. In Section 5, we describe the radio–CO, radio–IR, and IR–CO relations and discuss potential explanations for the observed deficit of radio emission in Section 6. We summarize our results and provide concluding remarks in Section 7.

2 SAMPLE

Our sample is drawn from the ATLAS^{3D} survey. This volume- and magnitude-limited ($D < 42$ Mpc and $M_K < -21.5$) survey of 260 ETGs uses multiwavelength data (Cappellari et al. 2011a) and theoretical models (Bois et al. 2011; Khochfar et al. 2011; Naab et al. 2014) to characterize the local population of ETGs and study their formation histories. The ATLAS^{3D} sample includes ETGs from a variety of environments with diverse kinematics, morphologies, and interstellar medium (ISM) properties. The rich data base of optical observations includes two-dimensional integral field spectroscopy (IFS) with the SAURON instrument (Bacon et al. 2001) on the William Herschel Telescope. These data are used to classify the ATLAS^{3D} galaxies on the basis of their stellar kinematics as 'slow rotators' and 'fast rotators' (Emsellem et al. 2007, 2011). Slow rotators are generally massive ellipticals and have little ordered rotation in their stellar velocity fields, while fast rotators are characterized by regular rotation. The fast rotator class contains lenticulars and some lower mass ellipticals whose discy nature was not previously recognized.

The ATLAS^{3D} survey also includes ground-based imaging from the Sloan Digital Sky Survey (York et al. 2000) or Isaac Newton Telescope (Scott et al. 2013), as well as extremely deep optical observations with the MegaCam instrument at the Canada–France–Hawaii Telescope (Duc et al. 2011, 2015). Molecular gas observations are available for the full ATLAS^{3D} sample from single-dish ^{12}CO(1–0) and (2–1) observations with the Institut de Radioastronomie Millimétrique (IRAM) 30-m telescope (Young et al. 2011), and represent the first large, statistical search for molecular gas in a sample of ETGs. A variety of other large data sets covering subsets of the full ATLAS^{3D} sample are also available and include H I imaging from the Westerbork Synthesis Radio Telescope (WSRT; Serra et al. 2012, 2014), interferometric ^{12}CO(1–0) maps (Alatalo et al. 2013) from the Combined Array for Research in Millimeter Astronomy (CARMA), and high-resolution ($\theta_{FWHM} \sim 0.5$ arcsec) VLA observations of the nuclear radio emission at 5 GHz (Nyland et al. 2016).

Table 1. New VLA observations.

Project	Dates	Time (h)	Galaxies	BW (MHz)	SPWs	Frequency (GHz)
(1)	(2)	(3)	(4)	(5)	(6)	(7)
10C-173	2011 March 13–31	10	20	256	2	1.39
12A-404	2012 June 5–August 9	23	52	1024	16	1.50

Notes. Column 1: Project ID. Column 2: Observing dates. Column 3: Total project length. Column 4: Number of galaxies. Column 5: Total observing bandwidth per polarization. Column 6: Number of spectral windows. Column 7: Central observing frequency.

3 RADIO CONTINUUM DATA

3.1 VLA sample selection

We obtained new 1.4 GHz VLA observations of 72 ETGs drawn from the ATLAS^{3D} survey (Cappellari et al. 2011a). Since our primary goal was to study SF in ETGs, we included as many of the 56 CO-detected ATLAS^{3D} galaxies as possible in our new observations. Of the 72 ETGs that we observed at 1.4 GHz, 52 have single-dish CO detections with IRAM at a spatial resolution of 22 arcsec (Young et al. 2011). The four CO-detected ATLAS^{3D} ETGs that we did not observe are NGC4283, NGC4435, NGC4476, and NGC4477. These galaxies were included in the Faint Images of the Radio Sky at Twenty Centimetres (FIRST; Becker, White & Helfand 1995) survey at 5 arcsec spatial resolution, though none were detected. In addition to the 52 CO-detected galaxies, we also observed 20 ATLAS^{3D} ETGs with CO upper limits only. These new observations of 20 molecular gas-poor ETGs, combined with archival observations from FIRST, thus provide a comparative 'control' sample for the VLA observations of the CO-detected ETGs.

3.2 Observations

We observed during the VLA B configuration at *L* band (1–2 GHz) over two projects, 10C-173 and 12A-404, spanning a total of 33 h. Our observational setup is summarized in Table 1. Project 10C-173 was observed as part of the Open Shared Risk Observing programme that offered 256 MHz of the total bandwidth. The full bandwidth for this project was split into two 128 MHz-wide spectral windows (SPWs), each containing 64 channels. We required 25 min of integration time per galaxy to achieve our desired rms noise of 25 μJy beam^{-1}. For Project 12A-404, we were able to utilize the full *L*-band bandwidth of 1024 MHz. We divided this bandwidth into 16 SPWs, each spanning 64 MHz and containing 64 channels. The wider bandwidth of project 12A-404 allowed us to reach an rms noise of 25 μJy beam^{-1} for each galaxy in about 15 min.

We divided each project into independent scheduling blocks (SBs) for flexible dynamic scheduling. We phase-referenced each galaxy to a nearby calibrator within 10°, and chose calibrators with expected amplitude closure errors of no more than 10 per cent to ensure robust calibration solutions. In addition, the positional accuracy of most of our phase calibrators was <0.002 arcsec. In order to set the amplitude scale to an accuracy of 3 per cent, as well as to calibrate the bandpass and instrumental delays, we observed the most conveniently located standard flux calibrator (3C286, 3C48, 3C147, or 3C138) once per SB (Perley & Butler 2013).

3.3 Calibration and imaging

Our data reduction strategy follows the higher resolution 5 GHz VLA study of the ATLAS^{3D} galaxies presented in Nyland et al. (2016), and we refer readers there for details. We flagged, calibrated, and imaged each SB using the Common Astronomy Software Applications (CASA) package (version 4.1.0) and the CASA VLA calibration pipeline version 1.2.0.[1] All of our SBs were Hanning smoothed prior to the pipeline calibration to minimize Gibbs ringing due to bright radio frequency interference. Nevertheless, typically one to three SPWs per SB in Project 12A-404 had to be flagged entirely from the data set to improve the quality of our images.

We imaged our data in CASA using the CLEAN task in the Multi Frequency Synthesis mode (Conway, Cornwell & Wilkinson 1990). Due to the large fractional bandwidths (∼67 per cent from 1 to 2 GHz), we imaged each galaxy with the parameter nterms = 2 (Rau & Cornwell 2011). We chose Briggs weighting (Briggs 1995) with a robustness parameter of 0.5 for the best compromise among sensitivity, sidelobe suppression, and spatial resolution. To correct for the effects of non-coplanar baselines, we set the parameters GRIDMODE = 'WIDEFIELD' and wprojplanes = 128. We produced large images covering the full *L*-band primary beam (30 arcmin) with a cell size of 0.75 arcsec. Self-calibration was performed when necessary following standard procedures. Sources with evidence of extended structures were imaged using the multiscale algorithm (Cornwell 2008).

3.4 Image analysis

Measurements of source fluxes, sizes, and their corresponding uncertainties follow the detailed description in Nyland et al. (2016). In brief, the rms noise of each image was determined by averaging the flux densities in several source-free regions. For detections, we required a peak flux density of $S_{\rm peak} > 5\sigma$, where σ is the rms noise. Upper limits for non-detections were set to $S_{\rm peak} < 5\sigma$. We also required radio sources to be spatially coincident with the host galaxy optical position to within 3 arcsec. For each radio source with a Gaussian-like morphology, we determined the source parameters (peak flux density, integrated flux density, deconvolved major and minor axes, and deconvolved position angle) by fitting a single two-dimensional elliptical Gaussian model using the JMFIT task in the 31DEC15 release of the Astronomical Image Processing System (AIPS).

For sources with more complex/extended morphologies, we measured the spatial parameters by hand using the CASA VIEWER and calculated the integrated flux density using the task IMSTAT. The image and source parameters are summarized in Tables A1 and A2. Maps of our detected sources are provided in Fig. B1 and relative contour levels are given in Table B1.

[1] https://science.nrao.edu/facilities/vla/data-processing/pipeline

3.5 Detection rate and morphology

The detection rates in projects 10C-173 and 12A-404 are 19/20 and 35/52, respectively, and the combined detection rate for both projects is 51/72 (71 ± 5 per cent). Including the galaxies with archival data at comparable spatial resolution from FIRST (see Section 3.6.2), the total detection rate of ATLAS^{3D} ETGs with kpc-scale 1.4 GHz emission is 79/252 (31 ± 3 per cent). This combined detection rate is likely a lower limit due to poorer sensitivity of FIRST compared to our new observations.

Many of the detected source morphologies resemble the resolved, disc-like radio structures present in typical star-forming spirals and span scales of 200–900 pc for the nearest (D = 11.1 Mpc) to the farthest (D = 45.8 Mpc) ETGs, respectively. The fraction of detected ETGs with resolved emission is 41/51 (80 ± 6 per cent; see Table A2). There are 19/51 sources (37 ± 7 per cent) with distinct multiple components or extended morphologies on scales of ∼1 kpc or larger. Optical images of these 19 sources overlaid with the radio contours are shown in Fig. B2. The source with the largest spatial extent spans ≈18 kpc and is characterized by prominent twin radio jets launched by the active nucleus hosted by NGC3665. In eight galaxies, the 1.4 GHz emission is distributed among multiple components. We summarize the flux and spatial properties of these multicomponent sources in Tables A3 and A5.

3.6 Comparison to previous studies

3.6.1 NVSS

All of the ATLAS^{3D} galaxies fall within the survey area of the 1.4 GHz NRAO VLA Sky Survey (NVSS; Condon et al. 1998). There are 54/260 (21 ± 3 per cent) ATLAS^{3D} ETGs detected in the NVSS catalogue (within a search radius of 10 arcsec) at a detection threshold of 2.5 mJy beam^{-1}. For most of these galaxies, the emission is unresolved at the low spatial resolution ($\theta_{\rm FWHM} \approx 45$ arcsec) of NVSS. Nevertheless, for the 32 ETGs detected in both NVSS and our new VLA observations, the flux densities are generally in good agreement. Accounting for the typical power-law dependence[2] of radio flux density with frequency, the median ratio between the NVSS and VLA flux densities is 1.13. We address the possibility of resolved-out radio emission and its influence on our analysis in Section 6.3.2.

3.6.2 FIRST

FIRST provides the largest compilation of 1.4 GHz images with spatial resolutions ($\theta_{\rm FWHM} \approx 5$ arcsec) comparable to the new VLA observations presented here. Although 239 (92 per cent) of the ATLAS^{3D} galaxies are included in the FIRST survey footprint, only 57 (24 ± 3 per cent) have flux densities above the 5σ detection threshold of 1 mJy beam^{-1} (within a search radius of 5 arcsec). Our new VLA data are typically a factor of 5 times more sensitive than FIRST, and this is reflected in our higher detection rate. We detect 1.4 GHz emission in 15 galaxies that were previously undetected in FIRST.

For ETGs detected in both our new 1.4 GHz data and FIRST, we find good agreement between the flux densities, with a median flux ratio of 0.98. The single significant outlier is NGC3665, however, the Gaussian-fit integrated flux density reported in the FIRST catalogue[3] substantially underestimates the total 1.4 GHz emission in this extended radio source (see Fig. B1) by over an order of magnitude. After re-measuring the integrated flux density in the NGC3665 FIRST image by hand, we found good agreement between the FIRST data and our new VLA observations.

3.6.3 Previous ETG surveys

Sadler, Jenkins & Kotanyi (1989) and Wrobel & Heeschen (1991) performed 5 GHz imaging studies of large samples of ETGs and concluded that the radio morphologies and multiwavelength source properties indicated that the radio emission in at least some ETGs is likely related to recent SF. The volume-limited study by Wrobel & Heeschen (1991) is the most comparable ETG survey to the 1.4 GHz study of the ATLAS^{3D} ETGs presented here. While sample sizes and spatial resolutions are similar, our new 1.4 GHz observations reach sensitivities nearly an order of magnitude deeper after adjusting the 5 GHz detection threshold of the Wrobel & Heeschen (1991) study to 1.4 GHz assuming a standard radio spectral index of $\alpha = -0.7$. The detection fraction in Wrobel & Heeschen (1991) is 52/198 (26 ± 3 per cent) galaxies, 7/52 (13 ± 5 per cent) of which display extended, disc-like morphologies strongly suggestive of an SF origin.

40 ETGs are included in the 1.4 GHz study presented here and in Wrobel & Heeschen (1991). The detection rates for these ETGs are 21/40 (53 ± 8 per cent) and 28/40 (70 ± 7 per cent) for the 5 GHz Wrobel & Heeschen (1991) observations and the 1.4 GHz observations presented here, respectively. If the ETGs with archival FIRST data are included along with our new 1.4 GHz observations, the overlap between the Wrobel & Heeschen (1991) and the ATLAS^{3D} samples increases to 143 galaxies. Of these, only 36/143 (25 ± 4 per cent) were detected by Wrobel & Heeschen (1991). The total (new + archival) 1.4 GHz detection rate of the ETGs common to both studies at 5 arcsec resolution is 40/143 (28 ± 4 per cent).

We also compare our new 1.4 GHz data to a higher resolution, complementary 5 GHz study of the nuclear emission in the ATLAS^{3D} ETGs (Nyland et al. 2016). There are 142 galaxies with both 1.4 GHz data at ≈5 arcsec resolution (this work) and 5 GHz data at ≈0.5 arcsec (∼25–100 pc) resolution (Nyland et al. 2016). Of these 142 ETGs, 74 (52 ± 4 per cent) are detected at each band, with 60 (42 ± 4 per cent) detected in both data sets. 54 (38 ± 4 per cent) ETGs are non-detections in both our new 1.4 GHz data and the 5 GHz data from Nyland et al. (2016). These galaxies may be genuinely quiescent ETGs with no measurable SF or AGN emission.

14 (10 ± 3 per cent) ETGs (see Table A6) were detected only in the high-resolution 5 GHz observations. This could be due to the higher sensitivity of these 5 GHz data. Another possibility is that the nuclear radio sources in these ETGs are associated primarily with low-luminosity AGNs (Ho 2008) rather than SF.

For a different set of 14 ETGs (see Table A6), we detect emission in our lower resolution 1.4 GHz data, but not in the high-resolution 5 GHz data presented in Nyland et al. (2016). In these galaxies, the majority of the radio emission is likely distributed on scales larger than ∼100 pc, and may have been resolved-out in the higher resolution data. The dominance of radio continuum emission on larger scales in these galaxies suggests that their radio emission is primarily associated with SF. This is supported by the fact that 11/14 (79

[2] $S \propto \nu^{\alpha}$, where S is the radio continuum flux density, ν is the frequency, and α is the radio spectral index. The radio spectral index is assumed to have a value of $\alpha \approx -0.7$ for unabsorbed, non-thermal, synchrotron emission (Condon 1992; Marvil, Owen & Eilek 2015).

[3] http://sundog.stsci.edu/index.html

± 11 per cent) of these galaxies also harbour molecular gas (Young et al. 2011). The three galaxies without molecular gas detections are NGC1023, NGC3193, and NGC6547, though NGC1023 does contain a large, disturbed H I reservoir (Serra et al. 2012).

4 MULTIWAVELENGTH DATA

A summary of the CO and IR data included in our analysis is provided in Table A6. In the remainder of this section, we describe the CO and IR data used to compute the CO-radio and IR-radio ratios.

4.1 Molecular gas data

As mentioned in Section 2, one of the most unique aspects of the ATLAS^{3D} survey of ETGs is the availability of CO data for the full sample (Young et al. 2011). This allows a direct measurement of the amount of raw material available for future SF. Nearly 25 per cent of the ATLAS^{3D} galaxies were detected in Young et al. (2011), with H_2 masses ranging from 1.3×10^7 to 1.9×10^9 $M_\odot$. We use these CO data in concert with our 1.4 GHz VLA data to investigate the relationship between radio luminosity and molecular gas mass in Section 5.1.

4.2 IR data

4.2.1 IRAS

The FIR luminosity provides an estimate of the integrated 42.5–122.5 μm emission (Helou et al. 1988), and is commonly defined as follows:

$$L_{\rm FIR}(\rm L_\odot) \equiv \left(1 + \frac{S_{100\,\mu\rm m}}{2.58\,S_{60\,\mu\rm m}}\right) L_{60\,\mu\rm m}, \quad (1)$$

where $S_{60\,\mu\rm m}$ and $S_{100\,\mu\rm m}$ are the *Infrared Astronomical Satellite* (*IRAS*; Soifer, Neugebauer & Houck 1987) 60 and 100 μm band flux densities are in Jy, respectively, and $L_{60\,\mu\rm m}$ is measured in solar luminosities (Yun et al. 2001).

We obtained the FIR data at 60 and 100 μm from NED. FIR measurements from *IRAS* were available for 195 of the ATLAS^{3D} galaxies, however, only 96 galaxies were detected at both 60 and 100 μm. We discuss the FIR data further in Section 5.2.1, where we study the global FIR–radio relation.

4.2.2 WISE

Sensitive MIR data from the *Wide-field Infrared Survey Explorer* (*WISE*; Wright et al. 2010) are available for the full ATLAS^{3D} sample, and we utilize these data in Section 5.2.2 to examine the relationship between the MIR and radio continuum emission. All of the ATLAS^{3D} galaxies are detected in the four *WISE* bands. In the *W*1, *W*2, and *W*3 bands at 3.4, 4.6, and 12 μm, respectively, all of the ATLAS^{3D} galaxies are robustly detected. In the *W*4 band at 22 μm, 29 galaxies have signal-to-noise ratios less than 2 in their profile fits. However, the aperture photometry fluxes measured within an area defined by the spatial properties of the near-IR emission from the Two Micron All Sky Survey (2MASS; Skrutskie et al. 2006) of each galaxy yield a measurement within the sensitivity limits of the *W*4 band. Thus, we consider these 29 galaxies as genuine, albeit weak, detections.

We extracted *WISE* photometry from the AllWISE source catalogue (Cutri & et al. 2013) and performed cross matching with the official ATLAS^{3D} positions (Cappellari et al. 2011a) within a search radius of 5 arcsec. The *W*4-band data provide a spatial resolution of $\theta_{\rm FWHM} \approx 11.8$ arcsec. Although most of the ATLAS^{3D} galaxies are only marginally resolved at 22 μm, we selected photometric measurements derived within the elliptical area of the 2MASS emission for each galaxy (*w4gmag*) when possible. If *w4gmag* magnitudes were unavailable, we used the Gaussian profile fit magnitudes instead (*w4mpro*).

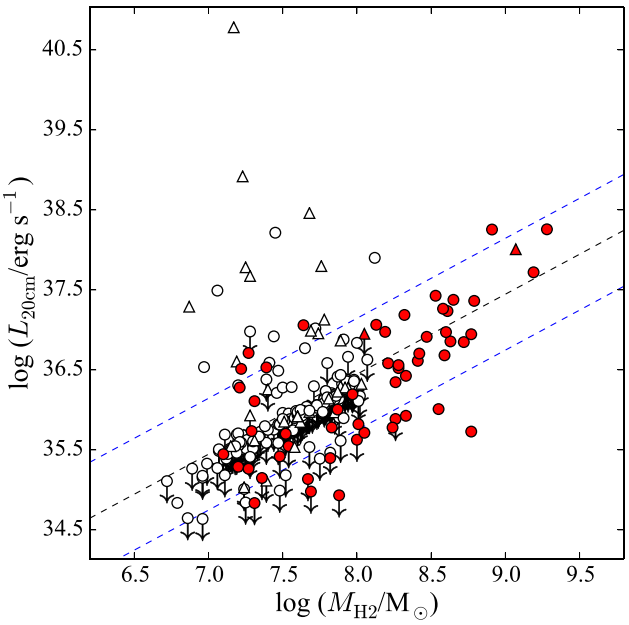

Figure 1. Global radio–M_{H2} relation for the ATLAS^{3D} survey. H_2 masses were derived from the single-dish IRAM CO measurements (Young et al. 2011). CO detections are highlighted by red symbols and CO upper limits are shown as white symbols. Upper limits to the 1.4 GHz luminosity are shown as downward-pointing arrows. Circles represent fast rotators and triangles represent slow rotators (Emsellem et al. 2011). The dashed black line represents the expected radio luminosity (equation 15; Murphy et al. 2011) if the SFRs of the ATLAS^{3D} ETGs agree with the SFRs predicted by the CO-derived H_2 mass. Assuming a conversion factor of $\alpha \equiv M_{\rm gas}/L_{\rm CO} = 4.6\,\rm M_\odot$ (K km s^{-1} pc^2)$^{-1}$ (Solomon & Vanden Bout 2005), this SFR relation is SFR $= 1.43 \times 10^{-9}$ ($M_{\rm H2}$/M$_\odot$) M$_\odot$ yr^{-1}. The upper and lower dashed blue lines denote $L_{20\rm cm}/M_{\rm H2}$ ratios of factors of 5 above and below the expected radio luminosity at a given molecular gas mass for typical star-forming galaxies.

5 GLOBAL RELATIONSHIPS

5.1 Radio–H_2 relation

Previous studies have found a strong correlation between the radio luminosity and CO luminosity in samples of spiral galaxies (e.g. Adler, Allen & Lo 1991; Murgia et al. 2002; Liu & Gao 2010; Liu, Gao & Greve 2015), with some studies reporting the correlation is as tight as the radio–FIR relation (e.g. Murgia et al. 2005). However, little information about whether molecular gas rich ETGs similarly follow this relationship is available.

In Fig. 1, we investigate the relationship between the molecular gas mass and radio luminosity. The dashed black line in this figure traces the expected 1.4 GHz luminosity based on the H_2-mass-derived SFR (Gao & Solomon 2004) and the calibration between the SFR and radio continuum luminosity from Murphy et al. (2011). In other words, this line denotes the radio luminosity one would expect

if the H_2–SFR and radio–SFR relationships previously established for star-forming spiral galaxies were also true for ETGs. Some of the most molecular gas rich ETGs shown in Fig. 1 have 1.4 GHz luminosities consistent with this extrapolation, suggesting they are forming new stars with efficiencies similar to those found in spiral galaxies. However, other ETGs in Fig. 1, particularly those with lower H_2 masses, appear to have less radio continuum emission than expected. In these galaxies, the radio emission may be genuinely suppressed. Alternatively, variations in the CO-to-H_2 conversion factor (X_{CO}) could cause the H_2 masses to be overestimated (see Section 6.1.1). Galaxies that are obvious outliers in Fig. 1, with high radio luminosities and only upper limits to their molecular gas masses, are likely massive ETGs dominated by AGN emission (see Section 6.2.2).

Of the 56 CO-detected and candidate star-forming ETGs shown in Fig. 1, at least 18 (32 ± 6 per cent) have 1.4 GHz luminosities a factor of 5 above/below the predicted radio luminosity indicated by the dashed line. The five CO-detected ETGs with radio emission exceeding the level expected from SF are NGC2768, NGC3245, NGC3665, NGC4111, and NGC4203. The enhanced radio emission in these galaxies may be the result of nuclear activity. A clear example of this is NGC3665, a low-power AGN host with prominent kpc-scale radio jets (see Fig. B1) that are responsible for the excess radio emission. Two other galaxies, NGC2768 and NGC4203, are classified as low-ionization nuclear emission-line regions based on their optical emission line ratios (Nyland et al. 2016), and may also be contaminated by nuclear activity at 1.4 GHz.

There are 13 CO-detected ETGs with radio luminosities deficient by at least a factor of 5 from the level predicted by the standard SF relations. Of these, seven have 1.4 GHz detections (NGC4150, NGC4429, NGC4459, NGC4753, NGC5273, NGC5379, and UGC09519), and six have upper limits only (NGC3156, NGC4119, NGC4324, NGC4596, PGC016060, and PGC061468). For the ETGs with the most extreme radio deficiencies, NGC4119 and UGC09519, the radio emission is deficient by factors of about 25 and 30, respectively. An additional six galaxies (NGC0509, NGC3073, NGC3599, NGC4283, NGC4476, and NGC4477) have radio upper limits within a factor of 5 above/below the dashed line in Fig. 1.

If the radio deficiency relative to the H_2 mass genuinely exists and is not the result of a varying X_{CO}, possible causes include reduced SFE, predominantly low-mass SF, weak galactic magnetic fields, and enhanced cosmic ray losses. We further discuss these potential explanations in Section 6. In the following section, we examine the relationship between the radio continuum and IR emission, another interesting proxy of the global SF conditions.

5.2 Radio-IR relation

5.2.1 Far-infrared

Many previous studies have explored the FIR–radio relation for various samples of galaxies (e.g. Yun et al. 2001; Condon et al. 2002). These studies have determined a range of average q-values characteristic of typical SF, where the q-value is defined as

$$q \equiv \log\left(\frac{\mathrm{FIR}}{3.75\times10^{12}\,\mathrm{W\,m^{-2}}}\right) - \log\left(\frac{S_{1.4\,\mathrm{GHz}}}{\mathrm{W\,m^{-2}\,Hz^{-1}}}\right), \quad (2)$$

and FIR is the standard FIR estimator defined as

$$\mathrm{FIR} \equiv 1.26\times10^{-14}\,(2.58\,S_{60\,\mu\mathrm{m}} + S_{100\,\mu\mathrm{m}})\,\mathrm{W\,m^{-2}}. \quad (3)$$

One of the most widely cited publications, Yun et al. (2001), reports an average q-value of 2.34, with $q < 1.64$ and $q > 3.00$ defining 'radio-excess' and 'FIR-excess' galaxies, respectively.

In the top-left panel of Fig. 2, we have plotted the 20 cm radio luminosity as a function of the FIR luminosity measured at 60 μm for the 94 ATLAS^{3D} galaxies with *IRAS* detections at both 60 and 100 μm. A few galaxies have excess radio continuum emission well beyond what would be expected if they were dominated by SF alone. These sources lie above the relationship for typical star-forming galaxies illustrated by the upper blue dashed line in the top-left panel of Fig. 2, and include many well-known AGNs in our sample. The top-right and bottom panels of Fig. 2 also clearly highlight these galaxies. The nine galaxies in the radio excess category are NGC3665, NGC3998, NGC4261, NGC4278, NGC4374, NGC4486, NGC4552, NGC5322, and NGC5353. Only two of these galaxies, NGC3665 (Young et al. 2011; Alatalo et al. 2013) and NGC3998 (Baldi et al. 2015), are known to harbour any molecular gas.

35 ETGs were detected at 1.4 GHz and have q-values consistent with typical star-forming galaxies, suggesting the presence of active SF in these systems (for alternative possibilities, see Section 6.4.2). These ETGs tend to have high FIR luminosities (top-left and right-hand panels of Fig. 2) and H_2 masses (bottom panel of Fig. 2). However, even among the ETGs with 'normal' q-values consistent with SF, there is still a tendency towards higher q-values. Most of our sample galaxies have systematically high FIR-radio ratios at a given 60 μm luminosity and H_2 mass, suggesting that star-forming ETGs are either overluminous in the FIR or underluminous at radio frequencies compared to typical star-forming spirals. This effect becomes more significant at low FIR luminosities, in-line with reports from previous studies of a possible steepening of the relation for galaxies with $L_{60\,\mu\mathrm{m}} < 10^9\,\mathrm{L_\odot}$ (Yun et al. 2001).

As shown in the top-right panel of Fig. 2, many of the ETGs in our study may be classified as FIR-excess sources based on their high FIR-radio ratios ($q > 3.00$; Yun et al. 2001). A total of 18 galaxies (19 per cent) are characterized by FIR-radio ratios in the FIR-excess regime (see Table A6). To put this into perspective, less than 1 per cent of the galaxies included in the study by Yun et al. (2001) fell into the FIR-excess category. An additional 32 galaxies in our study with q-values in the range of normal star-forming galaxies only have 20 cm upper limits, meaning their q-values are *lower limits* and may be even higher in reality.

The results of our FIR-radio analysis are generally consistent with previous studies. Wrobel & Heeschen (1991) reported that, while ellipticals tended to lie above the FIR–radio relation due to excess radio emission likely originating from AGNs, lenticular galaxies generally conformed to the relation. However, they also identified a population of FIR-excess lenticulars, most of which were non-detections in their 5 GHz radio continuum study. These results are consistent with our study, in which many of the radio-excess sources are classified kinematically as slow rotators (massive ellipticals) and all of the FIR-excess sources are fast rotators (lower mass ellipticals and lenticulars). The fraction of sources in the FIR-excess category in Wrobel & Heeschen (1991) is roughly 10 per cent, much more similar to the fraction found in our study (19 per cent) than in studies of normal star-forming spiral galaxies (e.g. <1 per cent; Yun et al. 2001).

More recently, Combes et al. (2007) presented a study of the molecular gas and SF properties of the galaxies included in the SAURON survey (de Zeeuw et al. 2002), a representative sample of 48 nearby ETGs with IFS observations. They concluded that

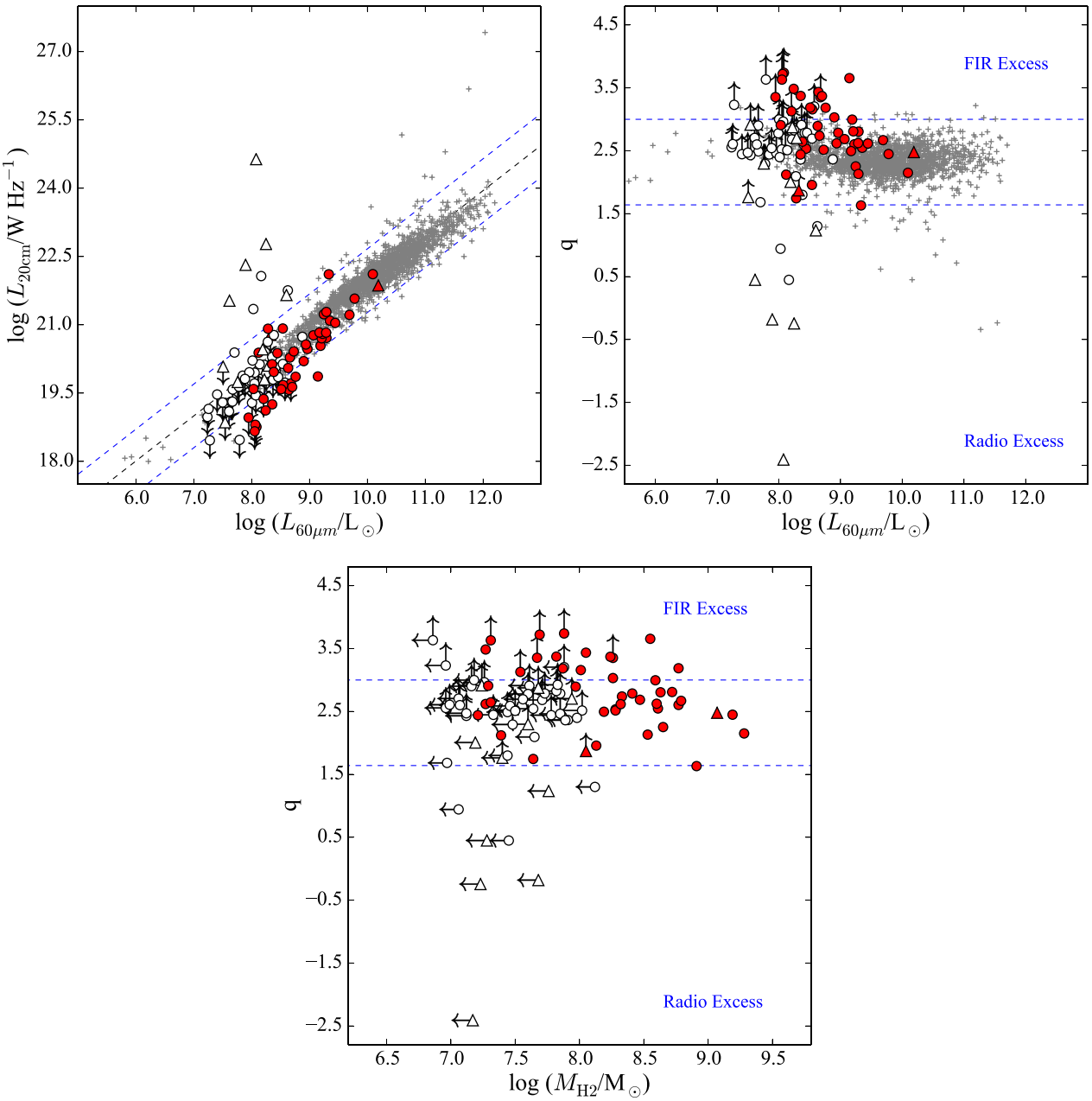

Figure 2. FIR–radio relation of the ATLAS^{3D} galaxies. Symbols filled in red represent the ATLAS^{3D} IRAM single-dish CO detections, while white symbols represent CO upper limits (Young et al. 2011). Circles represent fast rotators while triangles represent slow rotators (Emsellem et al. 2011). The gray symbols show the distribution of data points included in the analysis of the FIR–radio correlation presented in Yun et al. (2001). Top-left: the global radio–60 μm relation for the subset of the ATLAS^{3D} galaxies with *IRAS* 60 μm detections. The dashed black line is the formal fit to the relation defined in Yun et al. (2001). The dashed blue lines denote factors of 5 above and below the fit to the 20–60 μm relation. Upper limits to the 1.4 GHz luminosity are shown as downward-pointing arrows. Top-tight: the logarithmic FIR–radio flux density ratio, q, as a function of the 60 μm luminosity. The upper and lower dashed blue lines denote the classic divisions between sources with excess FIR ($q > 3.00$) and radio ($q < 1.64$) emission, respectively (Yun et al. 2001). Lower limits to the q-value are shown as upward-pointing arrows. Bottom: same as the top-right panel, except here the q-value is shown as a function of H_2 mass (Young et al. 2011). Upper limits to the H_2 mass are shown as leftward-pointing arrows.

the ETGs typically follow the radio–FIR relation, especially those with high H_2 masses. However, many of their FIR-radio ratio measurements were based on upper limits from FIRST, suggesting that some of the ETGs might actually reside in the FIR-excess regime. Additional studies (e.g. Lucero & Young 2007; Crocker et al. 2011) have confirmed that, while some ETGs are characterized by FIR-radio ratios consistent with star-forming spiral galaxies, many ETGs not dominated by AGNs show enhancements in their FIR emission relative to their emission at radio frequencies.

5.2.2 *Mid-infrared*

FIR emission is a robust SF tracer since it is sensitive to cool dust embedded deep within dense molecular cores present in

star-forming regions. However, only ∼36 per cent of the ATLAS^{3D} galaxies are detected in the FIR with *IRAS*. Detection rates in the MIR at 22 μm from the *WISE* All Sky Survey, on the other hand, are 100 per cent. MIR emission in star-forming galaxies arises from re-radiation of optical/UV emission by interstellar dust associated with newly formed massive stars. Unlike FIR emission, MIR emission traces warm dust, and as a consequence SFRs based on MIR data may be underestimated in purely star-forming galaxies (e.g. Calzetti et al. 2007; Jarrett et al. 2013). MIR emission may also arise from AGNs (e.g. Xilouris et al. 2004) and circumstellar dust associated with evolved stars that have passed through the (p)AGB phase (Knapp et al. 1992; Athey et al. 2002; Temi et al. 2009; Madau & Dickinson 2014). Thus, MIR emission may overestimate SFRs in ETGs hosting dusty AGNs and/or substantial circumstellar dust from an underlying evolved stellar population.

While separating the SF/AGN contributions to the MIR is not possible given sensitivity and spatial resolution limitations, removing the contamination to the MIR due to evolved stars is more straightforward. We use the relation between the 2MASS K_s-band luminosity and the *WISE* 22 μm luminosity from Davis et al. (2014) to estimate the portion of the MIR emission produced by old, passively evolving stars. We then subtract this 'passive' 22 μm component from the observed *WISE* 22 μm luminosity to obtain the MIR component related to SF. When the passive component of the MIR emission has been removed, we refer to the 22 μm luminosity as 'corrected'. The empirical relation for the corrected 22 μm luminosity used in this study can be found in equation 1 of Davis et al. (2014).

Calibrations of the MIR SFR have been studied extensively in the literature with instruments such as *Spitzer* (e.g. Calzetti et al. 2007; Rieke et al. 2009; Rujopakarn et al. 2013) and *WISE* (Donoso et al. 2012; Shi et al. 2012; Jarrett et al. 2013; Lee, Hwang & Ko 2013; Cluver et al. 2014; Wen et al. 2014). A number of studies have also analysed the MIR–radio relation (Elbaz et al. 2002; Gruppioni et al. 2003; Appleton et al. 2004; Beswick et al. 2008). The general consensus in the literature is that the radio and MIR emission are indeed correlated, albeit with somewhat increased scatter compared to the FIR–radio relation. Likely reasons for the increased scatter in the MIR–radio relation include the higher susceptibility to dust extinction at MIR wavelengths, as well as stronger contamination associated with evolved stars and dusty AGNs.

We investigate the MIR–radio relation for the ATLAS^{3D} sample in Fig. 3. For the MIR measurements, we required that our corrected 22 μm luminosities exceed the intrinsic scatter of the 22–2.2 μm relation defined in Davis et al. (2014) of ≈0.4 dex to be considered 'detections'. Most of the ATLAS^{3D} ETGs have only upper limits to their MIR and radio emission, and so we only show the 1.4 GHz luminosity as a function of the 22 μm luminosity for the 56 ATLAS^{3D} ETGs with molecular gas detections. The characteristics of the MIR–radio relation in these molecular gas rich ETGs is particularly relevant since they are good SF candidates. This figure shows similar behaviour to the radio–CO and radio–FIR relationships shown in Figs 1 and 2. However, we note that many of the CO-detected ETGs in Fig. 3 have high MIR-radio ratios even after the passive contribution to the 22 μm emission has been subtracted.

Fig. 3 also shows a series of linear fits to the 22 μm–20 cm relation from the literature (Shi et al. 2012; Jarrett et al. 2013; Wen et al. 2014). The closest fit to our data above 22 μm luminosities of 10^{42} erg s^{-1} is that of Jarrett et al. (2013), who studied the MIR–radio relation for a small sample of local galaxies (including three ETGs) with SFRs ranging from 0 to 3 $M_\odot$ yr^{-1}. Since the relationship between the radio and MIR emission in Jarrett et al. (2013) was

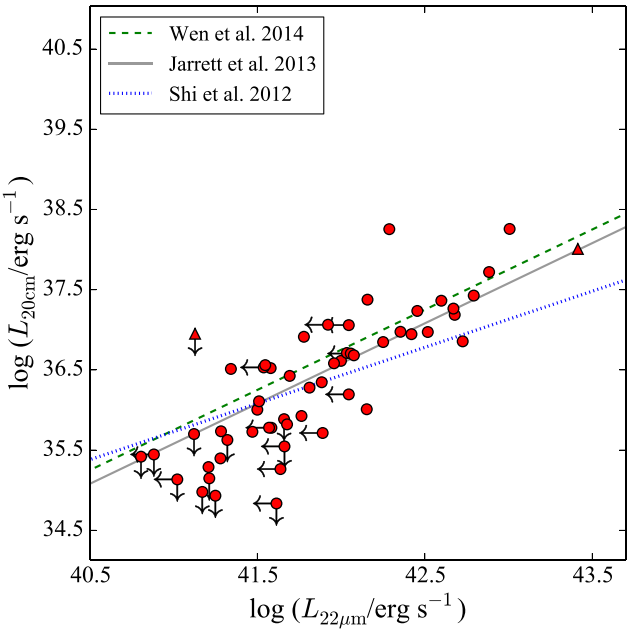

Figure 3. Global radio–22 μm relation for the molecular gas rich ATLAS^{3D} ETGs. The 22 μm fluxes have been corrected for the contribution of pAGB stars using equation 1 from Davis et al. (2014). Symbols filled in red represent the ATLAS^{3D} IRAM single-dish CO detections, while white symbols represent CO upper limits (Young et al. 2011). Circles represent fast rotators while triangles represent slow rotators (Emsellem et al. 2011). The lines represent a series of linear fits to the radio–22 μm relation from the literature (green dashed: Shi et al. 2012; solid grey: Jarrett et al. 2013; and blue dotted: Wen et al. 2014).

consistent with previous studies using 24 μm data from *Spitzer* (e.g. Rieke et al. 2009), the relationship between the 1.4 GHz and the *WISE* 22 μm emission in our sample is also in good agreement with these studies. For $L_{22\,\mu m} < 10^{42}$ erg s^{-1}, the radio luminosities measured for the ATLAS^{3D} galaxies begin to decline sharply from the literature extrapolations of the 22 μm–radio relations. This observed steepening of the MIR–radio relation for less MIR-luminous ETGs is consistent with the behaviour of the FIR–radio relation discussed in Section 5.2.1.

We show the logarithmic 22 μm-radio ratio, $q_{22} \equiv \log_{10}(S_{22\,\mu m}/S_{20\,cm})$, as a function of the corrected 22 μm luminosity in Fig. 4. A few obvious outliers associated with active nuclei have extremely low q_{22}-values, while a number of other galaxies with high 22 μm luminosities are consistent with normal SF. The majority of the galaxies have only upper limits on one or both parameters or are consistent with high q_{22} values. The median q_{22} value for the subset of CO-detected, star-forming ATLAS^{3D} galaxies shown in Fig. 4 is 1.52. For comparison, we computed the median q_{22} value of the sample of spirals studied in Yun et al. (2001) and found a substantially lower value of 0.99.

5.3 CO–IR relation

So far we have considered the global relationships of radio luminosity versus molecular gas mass and radio luminosity versus IR luminosity. In these relationships, there appears to be a relative deficiency in the radio continuum luminosity compared to normal, star-forming spirals. Before we delve into a discussion of the possible causes of this observed deficiency, we first examine the relationship between the H_2 mass and IR luminosity to check if any of the

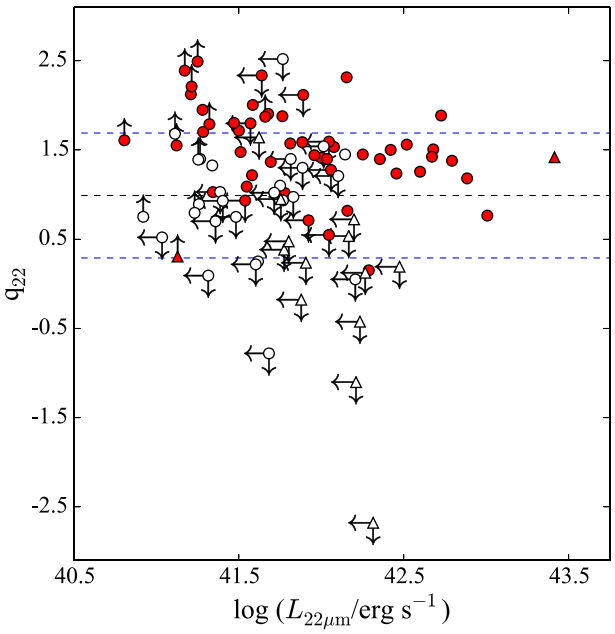

Figure 4. Logarithmic 22 μm-radio ratio (q_{22}) as a function of corrected 22 μm luminosity. Symbols filled in red represent the ATLAS^{3D} IRAM single-dish CO detections, while white symbols represent CO upper limits (Young et al. 2011). Circles represent fast rotators while triangles represent slow rotators (Emsellem et al. 2011). The upper and lower dashed blue lines denote q_{22} values of factors of 5 above and below the median value of the Yun et al. (2001) sample of $q_{22} = 0.99$ (black dashed line), respectively.

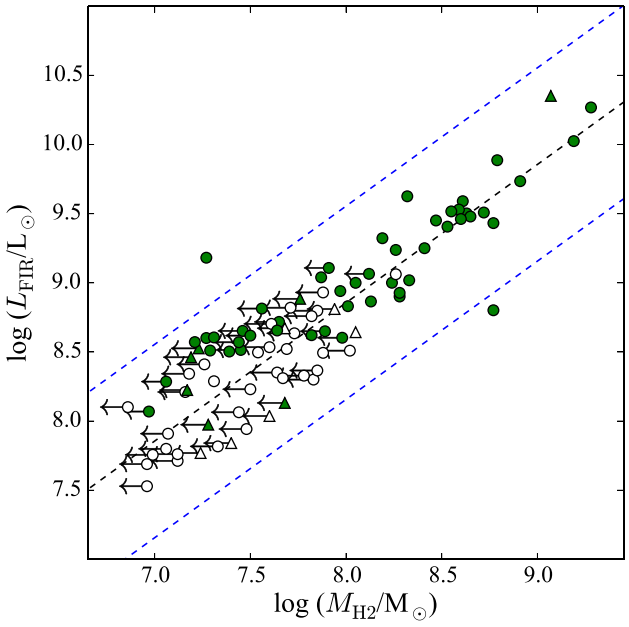

Figure 5. Global M_{H2}–L_{FIR} relation. H_2 masses were derived from the single-dish IRAM CO measurements (Young et al. 2011). CO upper limits are represented by left-pointing arrows. Green symbols are 1.4 GHz detections and white symbols are 1.4 GHz upper limits. Circles represent fast rotators and triangles represent slow rotators (Emsellem et al. 2011). The dotted black line is an extrapolation of the IR–CO relation of spirals from Gao & Solomon (2004), $L_{FIR}/L_{CO} = 33 \Rightarrow \log L_{FIR} = \log M_{H2} + 0.86$, where we have assumed a conversion factor of $\alpha \equiv M_{gas}/L_{CO} = 4.6$ M$_\odot$ (K km s^{-1} pc^2)$^{-1}$ (Solomon & Vanden Bout 2005). The upper and lower dashed blue lines denote M_{H2}/L_{FIR} ratios of factors of 5 above and below the standard relation for spirals, respectively. The two outliers to the extrapolated FIR–CO relation from Gao & Solomon (2004) are NGC3245 (above) and UGC09519 (below).

radio-deficient ETGs have extra contributions to the IR from AGN activity.

In Fig. 5, we show the FIR luminosity as a function of the H_2 mass for the 94 ATLAS^{3D} galaxies in our sample with detections at both 60 and 100 μm. The H_2 mass and FIR luminosity are tightly related, consistent with the previous conclusions of Combes et al. (2007), who examined the H_2–FIR relationship for a smaller subset of the ATLAS^{3D} galaxies. This suggests that inflation of the IR luminosities due to AGN contamination is likely not significant in our sample. Only two galaxies, NGC3245 and UGC09519, have H_2-FIR-ratios that lie slightly outside (above and below, respectively) a factor of 5 of the H_2–FIR relation from Gao & Solomon (2004). NGC3245 may have some contribution in the IR due to AGN dust heating based on AGN evidence at other wavelengths (Filho et al. 2004; Nyland et al. 2016). The low FIR luminosity of UGC09519, which is a candidate FIR-excess source, suggests the SFE in this galaxy may be significantly reduced compared to that of spirals.

6 DISCUSSION

As mentioned previously, Yun et al. (2001) reported that only 9 out of 1809 galaxies (≈0.5 per cent) in their sample were characterized by $q > 3.00$. However, we find that galaxies with high molecular gas-radio and IR-radio ratios are much more common in our sample, in agreement with the results of previous studies of the radio–IR correlation in ETGs (e.g. Wrobel & Heeschen 1991; Lucero & Young 2007; Crocker et al. 2011). As discussed in Section 5.2.1, 19 per cent, and perhaps as high as 53 per cent, of the ATLAS^{3D} galaxies with *IRAS* FIR measurements available are candidate FIR-excess sources. The fact that 39 per cent of the CO-detected ATLAS^{3D} ETGs also have $q > 3.00$ indicates that in some galaxies the FIR excess persists even in the presence of significant supplies of molecular gas. These unusually high H_2-radio and IR-radio ratios could either be caused by enhanced CO and/or IR emission, or a relative deficiency of radio continuum emission compared to normal, star-forming galaxies. Although it is difficult to definitively identify the foremost cause of the high q-values in the ATLAS^{3D} ETGs, we discuss a number of possibilities in the remainder of this section.

6.1 Excess CO emission

6.1.1 X_{CO} *factor*

The conversion factor used to derive the H_2 masses for the ATLAS^{3D} galaxies is $X_{CO} = N_{H2}/I_{CO} = 3 \times 10^{20}$ cm^{-2} (K km s^{-1})$^{-1}$ (Dickman, Snell & Schloerb 1986) and is discussed in detail in Young et al. (2011). However, if X_{CO} is in fact lower than this value, then the H_2 masses used in the analysis of Section 5.1 would be overestimates. It has long been suggested that the X_{CO} factor may depend on a variety of ISM parameters, such as metallicity and density (for a review, see Kennicutt & Evans 2012; Bolatto, Wolfire & Leroy 2013). Davis et al. (2014) explored the impact on SF due to a changing X_{CO} in the ATLAS^{3D} sample, arguing that X_{CO} variations driven by metallicity or gas density fluctuations between galaxies are unlikely to have a significant impact on SFR extrapolations and SFE estimates.

In addition to the effects of ISM properties, galaxy dynamics may also influence the X_{CO} factor. Davis et al. (2014) found that the CO in the ATLAS^{3D} ETGs generally resides in the rising part

of galactic rotation curve, indicating that much of the molecular gas in nearby ETGs is more centrally concentrated compared to spirals. Some studies have reported evidence that X_{CO} is lower in the central bulges of spiral galaxies (e.g. Sodroski et al. 1995; Meier & Turner 2004; Strong et al. 2004; Sandstrom et al. 2013), however other studies have contradicted this finding (e.g. Leroy et al. 2013). We therefore cannot rule out the possibility that the high CO-radio ratios in our sample are caused by a systematic overestimation of the H_2 masses due to a X_{CO} conversion factor that is lower than the canonical value. Further studies of the influence of galaxy dynamics on X_{CO} in ETGs will be necessary to settle this issue.

6.1.2 *Low SFE*

Martig et al. (2009, 2013) presented hydrodynamical simulations suggesting that the kinematic conditions characteristic of galaxy bulges and ETGs, such as high stellar velocity dispersions, can render molecular gas discs too stable to fragment into clumps and form stars efficiently. These studies concluded that this so-called 'morphological quenching' may be more pronounced in lower mass molecular gas discs, whereas the SFEs of larger molecular gas reservoirs should be less affected. The dynamical processes behind morphological quenching may also be responsible for decreased SFRs in the stellar bulges of spiral galaxies (Saintonge et al. 2012), although we note that this remains a controversial issue (Leroy et al. 2013). Could reduced SFEs due to a process such as morphological quenching be responsible for the deficiency of radio continuum emission relative to the molecular gas mass discussed in Section 5.1?

Davis et al. (2014) compared the Kennicutt–Schmidt (KS) relation (Kennicutt 1998) of nearby spiral galaxies with that of the CO-detected ATLAS^{3D} ETGs. They found that the ETGs had lower average SFR surface densities at a given molecular gas surface density compared to spirals, suggesting a decrease in the SFE of ETGs by a factor ≈2.5. This is in agreement with recent simulations by Martig et al. (2013) who predicted a decrease in the SFEs of ETGs by a similar amount.

In Fig. 6, we show the relationship between the FIR-radio ratio and SFE for the 44 CO-detected and candidate star-forming ATLAS^{3D} galaxies with *IRAS* FIR detections. The SFE is defined here as SFR/M_{gas}, where the SFR and M_{gas} are in units of $M_\odot$ yr^{-1} and $M_\odot$, respectively. M_{gas} is the total cold gas mass and includes gas in both the atomic (H I) and molecular (H_2) phases. The SFR and total cold gas mass for each candidate star-forming ETG were taken from table 1 of Davis et al. (2014). When possible, we selected the SFR measurements based on a combination of 22 μm and far-UV data. If far-UV data were not available, we used the 22 μm-derived SFRs instead for calculating the SFEs.

Most of the ETGs shown in Fig. 6 that are forming stars with $\log(\mathrm{SFE/yr^{-1}}) > -9.0$ have q-values within the range for typical star-forming galaxies. However, at lower SFEs, the number of ETGs with high q-value increases. We speculate that this may be due to lower SFEs in these systems. However, we emphasize that our sample is small and the difference between the incidence of high q-values at $\log(\mathrm{SFE/yr^{-1}}) > -9.0$ and $\log(\mathrm{SFE/yr^{-1}}) < -9.0$ is not statistically significant.

In Fig. 7, we show the q-value as a function of the ratio of the radius of the full extent of the interferometrically mapped molecular gas to that of the peak of the galactic rotation curve (Davis et al. 2014). Physically, this figure explores the dependence of q-value on the degree of central compactness of the molecular gas. The rotation curve of each galaxy in the ATLAS^{3D} survey has been calculated

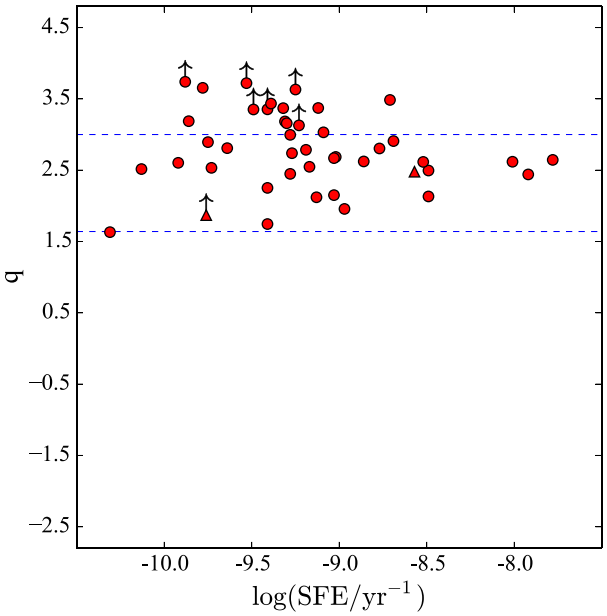

Figure 6. Logarithmic FIR-radio ratio (q) of the ATLAS^{3D} galaxies with *IRAS* 60 and 100 μm detections as a function of the star formation efficiency (SFE ≡ SFR/M_{gas}). SFEs were estimated from data provided in Davis et al. (2014). All objects shown in this figure represent the ATLAS^{3D} IRAM single-dish CO detections (Young et al. 2011). Circles represent fast rotators while triangles represent slow rotators (Emsellem et al. 2011). The upper and lower dotted blue lines denote the classic divisions between sources with excess FIR ($q > 3.00$) and radio ($q < 1.64$) emission, respectively (Yun et al. 2001).

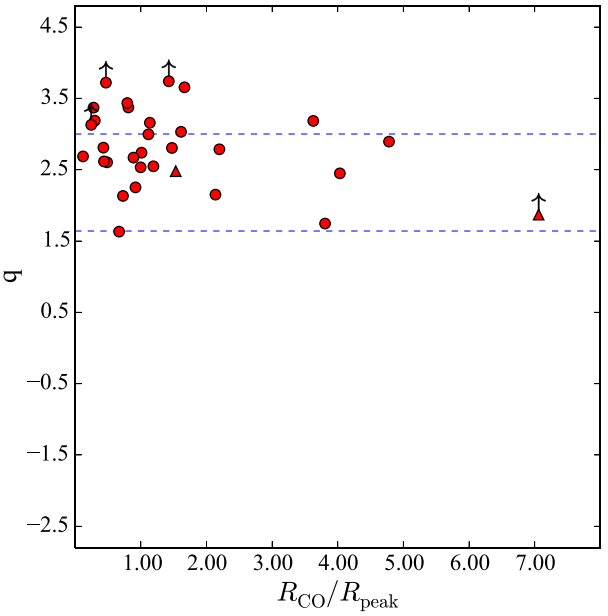

Figure 7. Logarithmic FIR-radio ratio (q) of the ATLAS^{3D} galaxies with *IRAS* 60 and 100 μm detections as a function of R_{CO}/R_{peak}, the ratio of the radius of the full extent of the molecular gas to that of the peak of the dynamically modelled galactic rotation curve (Davis et al. 2011, 2013, 2014; Cappellari et al. 2013). All objects shown in this figure represent the ATLAS^{3D} IRAM single-dish CO detections (Young et al. 2011). Circles represent fast rotators while triangles represent slow rotators (Emsellem et al. 2011). The upper and lower dotted blue lines denote the classic divisions between sources with excess FIR ($q > 3.00$) and radio ($q < 1.64$) emission, respectively (Yun et al. 2001).

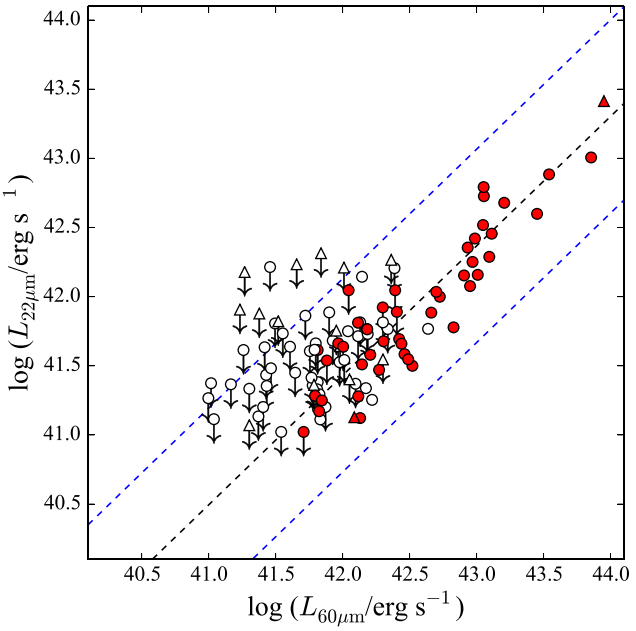

Figure 8. 60 μm *IRAS* luminosity versus corrected 22 μm *WISE* luminosity for the 106 ATLAS^{3D} ETGs with *IRAS* 60 μm detections. The 22 μm luminosities have been corrected for the contribution due to evolved stars (Section 5.2.2). Symbols filled in red represent the ATLAS^{3D} IRAM single-dish CO detections, while white symbols represent CO upper limits (Young et al. 2011). Circles represent fast rotators while triangles represent slow rotators (Emsellem et al. 2011). The dashed black line shows a linear fit between the 22 and 60 μm luminosities for the CO-detected ETGs, and the blue dashed lines denote factors of 5 above and below it. Downward-pointing arrows denote corrected 22 μm luminosities that are less than the intrinsic scatter of equation 1 from Davis et al. (2014).

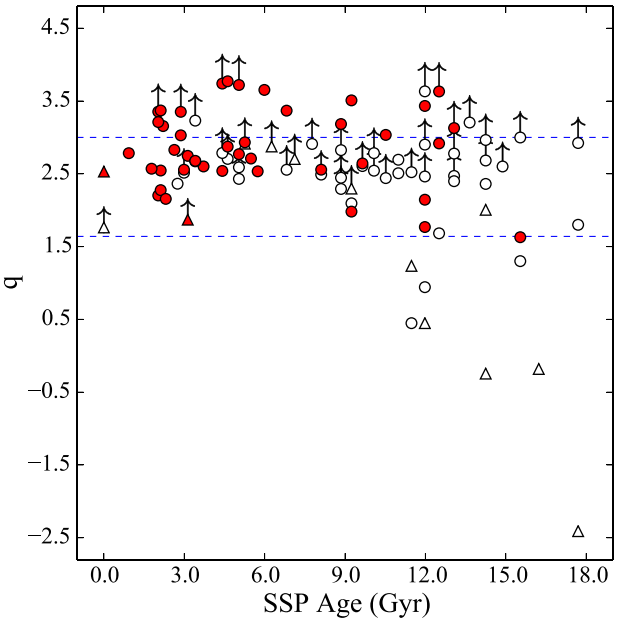

Figure 9. Logarithmic FIR-radio ratio (q) of the ATLAS^{3D} galaxies with *IRAS* 60 and 100 μm detections as a function of the SSP age measured within one effective radius (McDermid et al. 2015). Symbols filled in red represent the ATLAS^{3D} IRAM single-dish CO detections, while white symbols represent CO upper limits (Young et al. 2011). Circles represent fast rotators while triangles represent slow rotators (Emsellem et al. 2011). The upper and lower dotted blue lines denote the classic divisions between sources with excess FIR ($q > 3.00$) and radio ($q < 1.64$) emission, respectively (Yun et al. 2001).

based on dynamical models of the circular velocity. Details of this calculation, and derived parameters such as the radius at which the rotation curve peaks for each galaxy (R_{peak}), are provided in Cappellari et al. (2013). Although the number of data points is small, Fig. 7 hints at the possibility that ETGs with more centrally concentrated reservoirs of molecular gas are more likely to also have higher q-values. This would be consistent with the results of Davis et al. (2014), who found that the ATLAS^{3D} ETGs with the lowest SFEs had relatively compact distributions. However, the difference between the incidence of FIR-excesses galaxies below and above $R_{CO}/R_{peak} = 2$ is less than 2σ, and is therefore not statistically significant.

While decreased SFE may be responsible in part for the excess molecular gas relative to the radio continuum emission, it is a less viable explanation for the excess IR luminosity. This is because a decreased SFE would be expected to lead to a reduction in both radio and IR emission. We discuss possible explanations for the excess IR emission in Section 6.2.

6.2 Excess IR emission

6.2.1 Evolved stars

IR-based SFRs in ETGs may be contaminated by cool IR 'cirrus' emission and/or evolved stars, particularly in the MIR regime. IR cirrus emission at MIR and FIR wavelengths is produced by dust that has been heated by the interstellar radiation field. Since the interstellar radiation field is driven by the evolved stellar population of a galaxy, the contribution to the IR emission by IR cirrus should depend on the stellar luminosity. As demonstrated in Figs 3 and 4, most of the FIR-excess ETGs appear to also have excess MIR emission, even after the contribution due to the underlying evolved stellar population has been removed. In Fig. 8, we directly compare the 60 μm IRAS and corrected 22 μm WISE luminosities. This figure confirms that, for the majority of the CO-detected ATLAS^{3D} galaxies, the FIR and MIR luminosities are consistent with one another. Thus, we argue that the correction applied to the MIR luminosities to account for contamination by an older stellar population in Section 5.2.2 should effectively remove the cirrus component as well.

If any residual contamination is substantial, one might expect the IR-radio ratio to depend on the average age of the underlying stellar population. We test this possibility in Fig. 9. This figure shows the IR-radio ratio as a function of the single stellar population (SSP) age derived from models of the optical absorption line indices measured in IFS observations (McDermid et al. 2015). Fig. 9 shows that some of the galaxies with the highest q-values have relatively young SSP ages, suggesting that excess IR emission associated with stellar mass-loss from evolved stars is not the primary cause of the high IR-radio ratios. However, we note that the SSP ages considered here are luminosity weighted, and as a consequence, young stars may dominate the light even if they constitute a less significant fraction of the total stellar mass. Additionally, we note that Fig. 9 represents the relationship between q-value and SSP age in a globally averaged sense. Given that both bulk of the molecular gas and youngest stars tend to be centrally concentrated in ETGs (McDermid et al. 2012; Alatalo et al. 2013), a spatially resolved study of the variations of the IR-radio ratio with SSP age may lead to a different conclusion.

6.2.2 *Active nuclei*

Seyfert nuclei are known to heat dust in their surroundings that re-radiates at IR wavelengths (e.g. Ramos Almeida et al. 2011; Aalto et al. 2012). Thus, contamination from AGNs could contribute to the IR emission in IR-excess ETGs. However, since only two ETGs in the candidate FIR-excess category are classified as Seyferts (NGC3156 and NGC4324) based on the optical emission line diagnostics reported in Nyland et al. (2016), we do not expect AGN contamination in the IR to be significant in our sample.

It is possible that dust-enshrouded AGNs are present in some of the candidate IR-excess ETGs. Half of them (9/18; 50 ± 11 per cent) have nuclear radio sources identified in subarcsecond resolution 5 GHz data (Nyland et al. 2016). However, without any constraint on the bolometric luminosities associated with these low-power AGNs, it is difficult to assess just how much dust heating they might be able to provide. None of the candidate IR-excess ETGs has nuclear X-ray measurements or high-resolution IR data available in the literature. Existing high-resolution MIR studies of low-luminosity AGNs (Mason et al. 2012; Asmus et al. 2014), which include several ATLAS^{3D} ETGs with a nuclear radio source but a normal or low q-value, indicate that the MIR emission in most of these sources is still strongly host-galaxy dominated, arguing against the heating of dust by AGNs as a likely explanation for the IR-excess ETGs.

6.3 Deficient radio continuum emission

A number of physical scenarios could be responsible for the relative shortfall of radio continuum emission, including nascent SF, resolved-out radio continuum emission, a bottom-heavy stellar IMF, enhanced cosmic ray escape, weak galaxy magnetic fields, and environmental effects. We discuss each of these scenarios in the subsections that follow.

6.3.1 *Nascent SF*

Could we have serendipitously caught some of the CO-detected ETGs in the ATLAS^{3D} sample at the cusp of a newly re-ignited episode of SF? If nascent SF that only began a few million years ago were present, young stars would have had enough time to heat ambient dust and produce IR emission, but not necessarily enough time for significant numbers of supernovae to form. This lack of supernova-driven cosmic rays would subsequently reduce the observed amount of radio continuum emission at 1.4 GHz relative to the IR emission. Such a scenario has been suggested previously in the literature for disc-dominated galaxies with abnormally high IR-radio ratios (e.g. Roussel et al. 2003).

However, the incidence of galaxies with q-values in the FIR-excess range is 40 times higher in the ATLAS^{3D} ETGs compared to that of Yun et al. (2001). Therefore, it seems unlikely that young starbursts would be so much more common in ETGs compared to typical star-forming spirals. Simple statistical considerations also argue against this scenario. If we define the age of a nascent starburst to be less than 2 Myr and assume the total length of the SF episode is similar to a typical orbital time of about 100 Myr, then we would only expect to 'catch' about 2 per cent of the galaxies in this evolutionary state. Thus, the expected detection rate of galaxies in a nascent SF state is at least an order of magnitude less than the fraction of ETGs that actually have deficient levels of radio continuum emission in our sample.

Fig. 9 further argues against the nascent SF possibility. If nascent SF were a leading cause of the deficient radio continuum emission, we would expect the highest q-values to systematically correspond to the youngest SSP ages. However, as already discussed in Section 6.2, there is no trend between q-value and SSP age. Thus, we find that a dearth of cosmic rays due to a high incidence of exceptionally young SF in the ATLAS^{3D} ETGs is an unlikely explanation for the observed lack of radio continuum emission.

6.3.2 *Resolved-out radio emission*

The spatial resolution of the 1.4 GHz VLA data used in our analysis is ≈5 arcsec. Given the shortest spacing of 0.21 km in the VLA B-configuration in which these data were observed, structures on scales as large as ≈120 arcsec may be imaged given sufficient sensitivity. If the radio continuum emission in some of the sample ETGs is in fact dominated by larger scale, low-surface-brightness emission, this emission could be resolved-out or fall below our surface brightness sensitivity. As a consequence, the q-values of ETGs with radio continuum emission predominantly distributed over larger spatial scales would actually represent upper limits. This could in turn cause the q-values of some of these ETGs to be 'artificially' boosted into the FIR-excess regime.

To check whether the impact of resolved-out radio emission on the q-values is significant, in Fig. 10 we compare our VLA flux densities at lower spatial resolution with measurements from NVSS and the WSRT. The left-hand panel of Fig. 10 shows the comparison between the higher resolution VLA ($\theta_{\rm FWHM} \approx 5$ arcsec) and lower resolution NVSS ($\theta_{\rm FWHM} \approx 45$ arcsec) flux densities for the 32 ATLAS^{3D} ETGs detected in both series of 1.4 GHz observations. As mentioned in Section 3.6, the median ratio between the NVSS and VLA flux densities is 1.13 (with a range of 0.65–14.38).

The right-hand panel of Fig. 10 is similar to the left-hand panel, except here the 5 arcsec-resolution 1.4 GHz VLA flux densities are compared to the 1.4 GHz WSRT flux densities at a spatial resolution of $\theta_{\rm FWHM} \approx 35$ arcsec. The WSRT flux densities used in this panel of Fig. 10 were measured from images of the line-free channels from the ATLAS^{3D} H I observations presented in Serra et al. (2012). A detailed description of these data, including flux density measurements, will be presented in a future study. There are 25 ETGs that are detected in both the 5 arcsec-resolution VLA data and the lower resolution WSRT data. The ratio between the WSRT and VLA flux densities ranges from 0.81 to 1.93, with a median of 1.08. Thus, compared to the WSRT data, the higher resolution VLA data typically recovers about 92 per cent of the emission in the WSRT maps.

To test whether the exclusion of any large-scale radio emission is responsible for the high q-values in any individual cases, we recalculate q using the lower resolution NVSS and WSRT 1.4 GHz data. Of the four candidate FIR-excess ETGs with both 5 arcsec-resolution and lower resolution 1.4 GHz data (IC0719, NGC4694, NGC4526 and UGC09519), the q-values of IC0719 and NGC4694 decrease when q is calculated using the lower resolution radio data. The new q values of these two ETGs based on the lower resolution radio flux densities are now consistent with the range expected for 'normal star-forming' galaxies ($1.64 < q < 3.00$). Thus, it appears that the radio continuum emission associated with SF in IC0719 and NGC4694 is indeed much more extended than the spatial scales on which SF is actually occurring, perhaps similar to the situation in nearby starburst galaxies such as M82 (e.g. Seaquist & Odegard 1991). Since these two galaxies are not particularly unusual in other respects such as distance, CO flux density, angular size, or SFR, a future investigation into whether the spatially extended synchrotron emission reflects increased cosmic ray diffusion length-scales or unusual magnetic field configurations would be interesting.

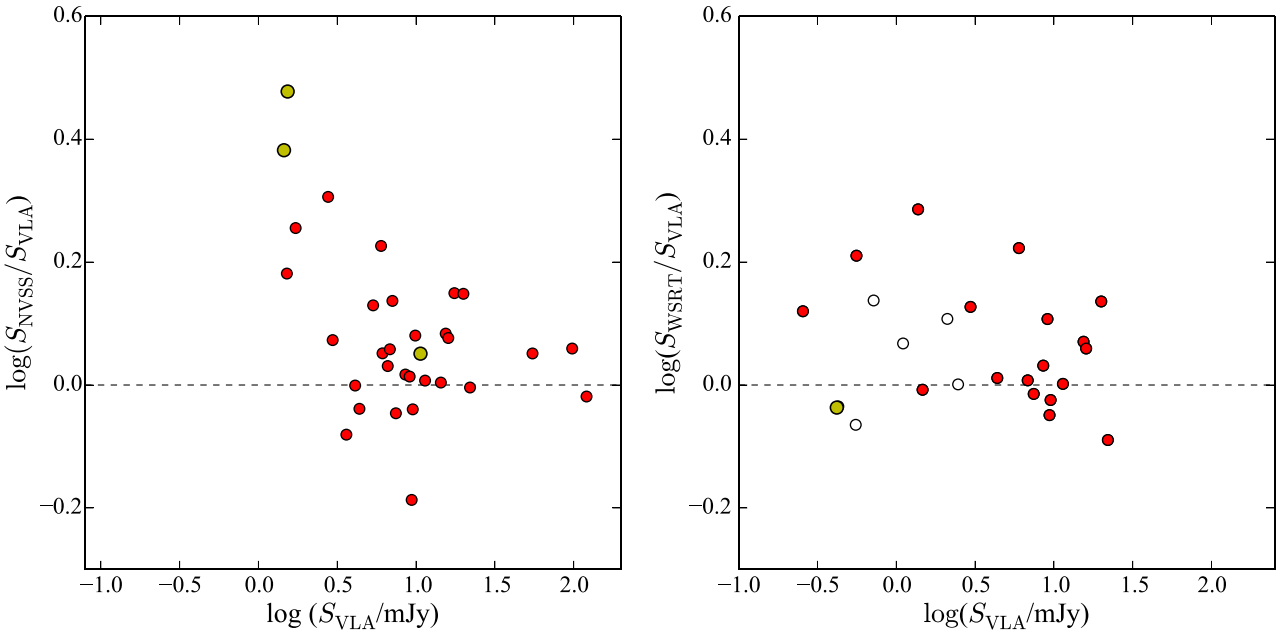

Figure 10. Left: comparison between the higher resolution ($\theta_{\rm FWHM} \approx 5$ arcsec) 1.4 GHz VLA flux densities and lower resolution ($\theta_{\rm FWHM} \approx 45$ arcsec) NVSS flux densities for the 32 ATLAS^{3D} ETGs detected in both. The *y*-axis shows the logarithmic flux ratio of the NVSS flux density to the VLA flux density and the *x*-axis shows the log of the VLA flux density at 5 arcsec spatial resolution. All of these ETGs were also detected in the ATLAS^{3D} IRAM single-dish CO observations (Young et al. 2011). The three yellow symbols highlight the galaxies initially categorized as FIR-excess sources that have both NVSS and new higher resolution VLA detections available. The black dashed line shows the expected logarithmic flux density ratio between the NVSS and VLA data, if there were a one-to-one correspondence between the two series of data. Right: same as the left-hand panel, except that the comparison is between the flux densities of the 25 ETGs that have both new, higher resolution ($\theta_{\rm FWHM} \approx 5$ arcsec), 1.4 GHz VLA detections and 1.4 GHz detections at lower spatial resolution ($\theta_{\rm FWHM} \approx 35$ arcsec) from WSRT. Symbols filled in red represent the ATLAS^{3D} IRAM single-dish CO detections, while white symbols represent CO upper limits (Young et al. 2011).

We conclude that incorporating radio emission on larger scales is important to avoid false identifications of FIR-excess galaxies. An ideal means of fully addressing this issue would be to obtain sensitive, lower resolution VLA data at 1.4 GHz in the C and D configurations for comparison with the existing higher resolution data from the VLA B configuration. However, we emphasize that some of the ATLAS^{3D} ETGs stubbornly remain in the FIR-excess category even when lower resolution data are used to calculate the *q*-value. The *q*-values of NGC4526 and UGC09519 remain high even when the radio flux density is integrated over much larger spatial scales. Thus, some of the ETGs in our sample appear to be genuinely radio deficient.

6.3.3 Bottom-heavy stellar IMF

The stellar IMF has long been regarded as a 'universal' parameter (e.g. Bastian, Covey & Meyer 2010). However, recent studies have reported that disc-dominated galaxies are best characterized by a Kroupa (Kroupa & Weidner 2003) IMF with a substantial fraction of high-mass stars, while massive ETGs are better characterized by a 'bottom heavy' IMF dominated by low- and intermediate-mass stars. These studies have argued that the IMF varies systematically as a function of galaxy parameters such as mass-to-light ratio (M/L), total stellar mass, stellar velocity dispersion, bulge fraction, and metallicity (e.g. Cappellari et al. 2012; Dutton, Mendel & Simard 2012; van Dokkum & Conroy 2012; Läsker et al. 2013; Posacki et al. 2015).

Since only stars with $M_{\rm star} \gtrsim 8$ M$_\odot$ will ultimately end their lives as supernovae (Condon 1992), a more bottom-heavy stellar IMF in massive ETGs would reduce overall supernova rates in these galaxies. Thus, an SFR tracer dominated by supernova-driven emission, such as centimetre-wave radio continuum observations, would naturally underestimate the SFR compared to both molecular gas mass and IR luminosity. Given that all stars with masses in the range of 0.5–8 M$_\odot$ pass through the AGB phase of stellar evolution in which they produce circumstellar dust that may re-radiate at IR wavelengths (Marigo et al. 2008), a bottom-heavy IMF dominated by stellar masses within this range would also be consistent with deficient radio continuum emission relative to the IR (e.g. Condon, Anderson & Helou 1991). However, we emphasize that the bottom-heavy IMF scenario for ETGs with IMFs dominated by stars with $M_{\rm star} < 0.5$ M$_\odot$ cannot explain the high *q*-values.

We now consider the relationship between *q*-value and IMF using metallicity as a proxy. The stellar IMF becomes systematically heavier with increasing metallicity (Smith, Lucey & Carter 2012; Martín-Navarro et al. 2015), and could manifest itself as a tendency for higher metallicity galaxies to be characterized by higher *q*-values due to the predominance of lower mass stars. In Fig. 11, we show the *q*-value as a function of metallicity. Only a few of the lower metallicity galaxies (e.g. [Z/H] < -0.45) have high *q*-values. As argued in McDermid et al. (2015), many of the lowest metallicity ATLAS^{3D} galaxies may have recently accreted new supplies of cold, low-metallicity gas. It is interesting to note that none of these lower metallicity ETGs have extreme *q* values. The ETGs with the highest *q* values seem to have higher, near-solar metallicities. This could be an indication that SF in higher metallicity environments in ETGs has less radio continuum emission associated with it, possibly due to a more bottom-heavy stellar IMF.

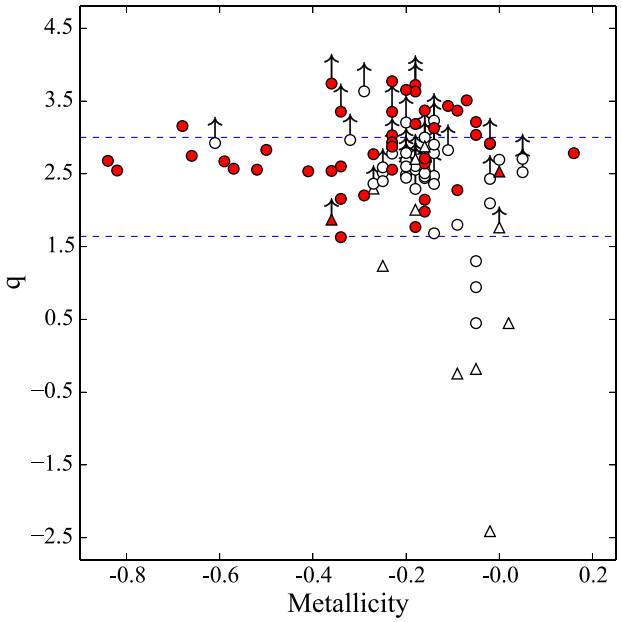

Figure 11. The logarithmic FIR-radio ratio (q) for the ATLAS^{3D} galaxies with *IRAS* 60 and 100 μm detections as a function of the metallicity, [Z/H], measured at one effective radius (McDermid et al. 2012). Symbols filled in red represent the ATLAS^{3D} IRAM single-dish CO detections, while white symbols represent CO upper limits (Young et al. 2011). Circles represent fast rotators while triangles represent slow rotators (Emsellem et al. 2011). The upper and lower dotted blue lines denote the classic divisions between sources with excess FIR ($q > 3.00$) and radio ($q < 1.64$) emission, respectively (Yun et al. 2001).

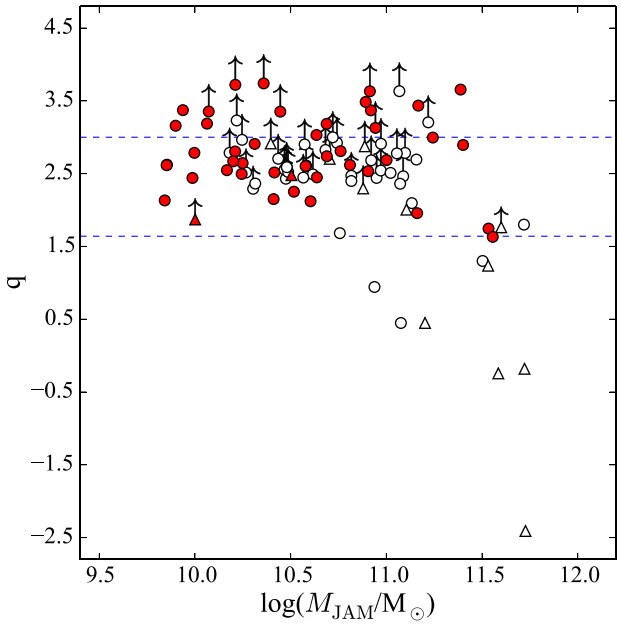

Figure 12. Logarithmic FIR-radio ratio (q) of the ATLAS^{3D} galaxies with *IRAS* 60 and 100 μm detections as a function of their dynamical mass, $M_{\rm JAM}$ (Cappellari et al. 2013). Symbols filled in red represent the ATLAS^{3D} IRAM single-dish CO detections, while white symbols represent CO upper limits (Young et al. 2011). Circles represent fast rotators while triangles represent slow rotators (Emsellem et al. 2011). The upper and lower dotted blue lines denote the classic divisions between sources with excess FIR ($q > 3.00$) and radio ($q < 1.64$) emission, respectively (Yun et al. 2001).

6.3.4 *Cosmic ray escape*

More rapid/efficient cosmic ray escape would lead to a reduction in the observed radio continuum emission. Unfortunately, robust estimates of cosmic ray diffusion rates require knowledge of many physical parameters, such as magnetic field strengths and cosmic ray production rates, that are poorly constrained at the present time, especially in bulge-dominated galaxies. This has even resulted in conflicting predictions in the literature (Condon 1992). Some theoretical studies have concluded that strong magnetic fields tend to drive cosmic rays away from their host galaxies more quickly (e.g. Chi & Wolfendale 1990), while others have reported the opposite of this effect (e.g. Lerche & Schlickeiser 1980).

Cosmic ray escape via diffusion or convection may become significant in galaxies with low luminosities and/or masses (Yun, Reddy & Condon 2001; Bell 2003; Boyle et al. 2007; Lacki, Thompson & Quataert 2010). Yun et al. (2001) pointed out that galaxies with $L_{60\,\mu\rm m} \lesssim 10^9$ L$_\odot$ tend to have high q-values, and suggested that these could be lower mass galaxies in which cosmic ray escape is more important compared to higher mass systems. Bell defined low-luminosity galaxies, which tend to have higher q-values, as those with $L \lesssim 0.01\,L_*$. Converting the optical luminosities to stellar mass using the relation from Bell et al. (2003) suggests that these low-luminosity galaxies have stellar masses of $\log(M_*/{\rm M}_\odot) < 10.8$.

We show the distribution of q-values as a function of dynamical mass for the ATLAS^{3D} sample in Fig. 12. The ATLAS^{3D} stellar masses, $M_{\rm JAM}$, are based on dynamical models that account for variations in the stellar M/L due to both age and metallicity, as well as systematic variations in the IMF (Cappellari et al. 2012, 2013). Fig. 12 shows that the radio-excess galaxies that likely house AGNs tend to have high dynamical masses, as expected. However, among the CO-rich ETGs likely to harbour SF, there is no strong dependence of the FIR-radio ratio on galaxy mass. High q-values are present in some of the gas-rich ETGs with the highest dynamical masses in the sample, well above the 'low-mass' galaxy definition suggested in Bell (2003). This suggests that cosmic ray escape due to low galaxy mass is not a dominant cause of the high q-values in our sample.

6.3.5 *Weak magnetic fields*

In addition to the presence of cosmic rays produced by recent supernovae, the level of radio continuum emission is also directly proportional to magnetic field strength. While the magnetic field properties of star-forming spiral galaxies have been studied in detail in the literature (e.g. Beck & Wielebinski 2013; Wiegert et al. 2015; Heesen et al. 2016), the magnetic field properties of star-forming, bulge-dominated ETGs are essentially unknown. Here, we estimate the minimum magnetic field strengths of the ETGs in our sample assuming near equipartition between the total cosmic ray particle and magnetic field energies. We define the minimum magnetic field strength, $B_{\rm min}$, as follows:

$$B_{\rm min} = 2.3\,[(1+a)\,AL/V]^{2/7}, \quad (4)$$

where a is the energy contribution of cosmic ray protons relative to that of electrons, A is a constant,[4] L is the radio luminosity, and V is the volume of the synchrotron emitting region. We assume a

[4] $A = C\,\frac{2\alpha+2}{2\alpha+1}\,\frac{\nu_2^{\alpha+1/2}-\nu_1^{\alpha+1/2}}{\nu_2^{\alpha+1}-\nu_1^{\alpha+1}}$, where C is a constant of value 1.057×10^{12} (g cm^{-1})$^{3/4}$ s^{-1}, α is the radio spectral index, and ν_1 and ν_2 are the lower and upper frequencies of the radio spectrum, respectively. We assume $\alpha = -0.8$, $\nu_1 = 10$ MHz, and $\nu_2 = 100$ GHz.

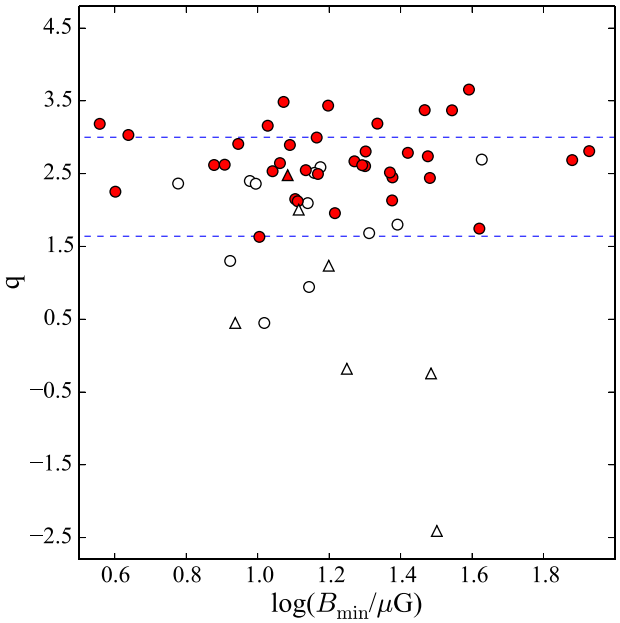

Figure 13. The logarithmic FIR-radio ratio (q) of the ATLAS^{3D} galaxies with *IRAS* 60 and 100 μm detections as a function of the minimum equipartition magnetic field. Symbols filled in red represent the ATLAS^{3D} IRAM single-dish CO detections, while white symbols represent CO upper limits (Young et al. 2011). Circles represent fast rotators while triangles represent slow rotators (Emsellem et al. 2011). The upper and lower dotted blue lines denote the classic divisions between sources with excess FIR ($q > 3.00$) and radio ($q < 1.64$) emission, respectively (Yun et al. 2001). Only sources with radio detections are shown.

standard literature value of $a = 100$ (e.g. Beck 2001), however, we note that the precise value of a, and the extent to which it varies among different galaxies or even among different environments within individual galaxies, is still poorly known. For the volume, we assume disc-like geometries similar to those used in magnetic field studies of star-forming spiral galaxies (e.g. Tabatabaei et al. 2013). These disc volumes are calculated as $V = \pi(d/2)^2 z$, where d is the major-axis diameter (Table A2) and z is the scaleheight assumed here to be 1 kpc (Beck & Wielebinski 2013). NGC3182 and NGC3665 required special geometric considerations. The 1.4 GHz emission of NGC3182 has a ring-like morphology, so an annular disc geometry was assumed. For NGC3665, which has 1.4 GHz emission with an extended, narrow, jet-like morphology, we used a cylindrical geometry.

We show the q-value as a function of the estimated (near) equipartition minimum magnetic field strength in Fig. 13. This figure shows no clear relationship between q-value and B_{min}, however we emphasize that only sources with radio detections are shown. The ETGs with the highest q-values have radio upper limits only. It is therefore possible that weak magnetic fields in these ETGs are the dominant cause of the shortfall of radio continuum emission and subsequently high q-values. Fig. 13 also shows that the B_{min} values for the ATLAS^{3D} ETGs range from about 4 to 85 μG, with a median magnetic field strength of about 15 μG. This is a factor of about 1.5 times above the average equipartition strength of the global magnetic field in the Milky Way and other similar spiral galaxies (Beck 2001; Beck & Wielebinski 2013). The galaxies with the strongest equipartition magnetic fields in our sample correspondingly have radio luminosities significantly higher than that of the Galactic Centre. In these galaxies, synchrotron emission associated with supermassive black hole accretion is likely contributing significantly to the 1.4 GHz flux density. However, we emphasize that the B_{min} estimates for our sample ETGs carry a number of caveats. The proton contribution to the particle energy budget compared to that of electrons (a), the cut-off frequencies of the radio continuum emission (ν_1 and ν_2), and the radio spectral index (α) are not precisely known for these galaxies. B_{min} is also fairly sensitive to changes in the radio source volume (e.g. if the diameter of the radio emitting region decreases by a factor of 2, then B_{min} will increase by a factor of ≈1.8). If larger scale radio continuum emission is present but resolved-out in our observations for some ETGs, our B_{min} estimates would underestimate the true values.

We conclude that decreased magnetic fields are a plausible explanation for the high q-values in our sample. However, additional observations of these galaxies over a broad range of frequencies and spatial scales, along with deep polarization measurements, would be necessary to verify that star-forming ETGs indeed have weaker magnetic fields than spirals and to quantify the magnitude of this effect on the q-values.

6.3.6 *Environment*

Galaxies residing in densely populated environments may suffer from gravitational interactions with the cluster potential or 'harassment' by other cluster galaxies, processes that could strip away loosely bound gas or even cosmic ray electrons (Moore, Lake & Katz 1998; Murphy et al. 2009). Cluster galaxies are also susceptible to 'ram pressure stripping' (Gunn & Gott 1972; Vollmer et al. 2001), in which gas is dislodged from galaxies as they travel through the hot intracluster medium (ICM). Since the ATLAS^{3D} sample includes 58 (22 per cent) Virgo cluster members, we can study the effect of the cluster environment on a number of SF-related properties. Serra et al. (2012) found that membership in the Virgo cluster has a strong impact on the detection rate and morphology of H I in the ATLAS^{3D} survey, with a decreased H I detection rate within the cluster. That study also reported that among ATLAS^{3D} ETGs in the Virgo cluster with H I detections, disturbed H I morphologies are common.

Virgo cluster ETGs also have, on average, older mass- and luminosity-weighted stellar population ages compared to field ETGs, even after controlling for galaxy mass (McDermid et al. 2015). This is an indication that SF histories are truncated earlier in Virgo cluster ETGs, and that their lower SFRs are long lived. An additional clue that the ISM contents of Virgo cluster ETGs are different is their boosted ^{13}CO/^{12}CO ratios relative to field ETGs, which may be due to preferential stripping of low-density molecular gas and/or the increased mid-plane pressure exerted on Virgo cluster galaxies by the ICM (Crocker et al. 2012; Alatalo et al. 2015). The decreased detection rate of H I, increased degree of central mass concentration of molecular gas, truncated SF histories, and boosted ^{13}CO/^{12}CO ratios of Virgo cluster ETGs are all expected consequences of ram pressure stripping (Vollmer et al. 2001; Tonnesen & Bryan 2009). Thus, ram pressure stripping is likely prevalent in at least some Virgo cluster ATLAS^{3D} ETGs, and it may therefore be an important process in shaping the residual SF in ETGs residing in cluster environments.

6.3.7 *Local galaxy density*

In Fig. 14, we show the q-value as a function of the local galaxy volume density to test whether a dense cluster environment has an effect on the FIR-radio ratio. Although this figure shows no clear

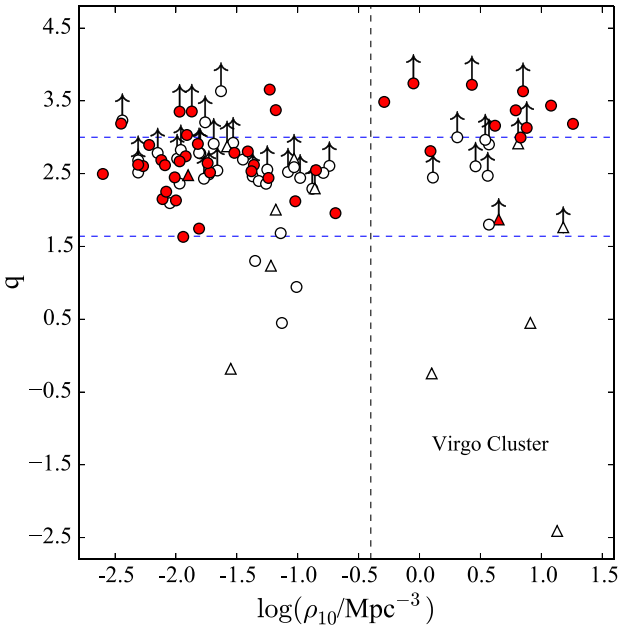

Figure 14. Logarithmic FIR-radio ratio (q) of the ATLAS^{3D} galaxies with *IRAS* 60 and 100 μm detections as a function of the mean volume density of galaxies within a sphere centred on each galaxy and containing the 10 nearest neighbours with $M_K < -21$ (ρ_{10}; Cappellari et al. 2011b). The vertical dotted black line at $\log(\rho_{10}/\mathrm{Mpc}^{-3}) = -0.4$ separates Virgo and non-Virgo cluster members to the right and left, respectively. Symbols filled in red represent the ATLAS^{3D} IRAM single-dish CO detections, while white symbols represent CO upper limits (Young et al. 2011). Circles represent fast rotators while triangles represent slow rotators (Emsellem et al. 2011). The upper and lower dotted blue lines denote the classic divisions between sources with excess FIR ($q > 3.00$) and radio ($q < 1.64$) emission, respectively (Yun et al. 2001).

relationship, we note that galaxies with high q-values populate environments with both high and low local galaxy densities, but there are very few galaxies in the Virgo cluster with q-values consistent with normal SF. In lower density environments, on the other hand, ETGs tend to have more moderate q-values.

The lack of Virgo cluster ETGs with moderate q-values could be due to tidal interactions and/or ram pressure stripping that has reduced the level of radio emission associated with SF. This would be in contrast to the results of previous studies of the FIR-radio ratio in ram pressure-stripped spiral galaxies, which have reported enhanced radio luminosities presumably due to the compression of magnetic fields via ram pressure and/or the thermal pressure of the ambient ICM (Miller & Owen 2001) and cosmic ray re-acceleration in shock regions (Reddy & Yun 2004; Murphy et al. 2009). However, a direct comparison of ram pressure stripping effects between spirals and ETGs may not be straightforward, and is further complicated by the fact that spirals have resided in the Virgo cluster for less time than the ETGs, and are thus not yet virialized in the cluster potential.

An alternative explanation for the deficit of Virgo ETGs that follow the radio–IR correlation is that the FIR emission is boosted by collisional dust heating due to ICM X-rays. However, prior studies of the FIR–radio relation in clusters have failed to find evidence that such dust heating plays a significant role in generating excess emission at FIR wavelengths (e.g. Reddy & Yun 2004), so we find this scenario unlikely.

6.3.8 Ram pressure stripping

We study the effects of ram pressure stripping in Fig. 15. In the left-hand panel of this figure, the q-value is shown as a function of the FIR luminosity for the 62 ATLAS^{3D} ETGs with both FIR and interferometric H I data (Serra et al. 2012). Symbols are coded to represent the various neutral gas morphologies defined in Serra et al. (2012). This figure shows no relationship between q-value and unsettled H I morphologies, although this could be due to the small number of galaxies (5/62) with this particular H I morphology. Instead, disc-like H I morphologies, as well as H I non-detections, are more prevalent among the high-q-value sources. Of the 22 galaxies with q-values in the normal range, 14 (64 ± 10 per cent) of them contain H I distributed in a disc. On the other hand, 24/33 (73 ± 8 per cent) of the ETGs with $q > 3.00$, or q-values that are lower limits, lack any detectable H I emission. The lack of H I in galaxies with high q-values could be a result of ram pressure stripping. However, we note that these ETGs do not necessarily reside in dense environments, and additional studies will therefore be necessary to verify or refute this claim.

In the right-hand panel of Fig. 15, we show the q-value as a function of FIR luminosity to study the relationship between the q-value and the molecular gas morphology for the 34 ETGs that have interferometric CARMA maps (Alatalo et al. 2013). We find no clear pattern between the CO morphology and q-value. Of the seven galaxies identified as having disrupted molecular gas morphologies in Alatalo et al. (2013), three have q-values consistent with normal SF while four are characterized by $q > 3.00$. Thus, we do not find compelling evidence that ETGs with signs of a recent gravitational disruption in their molecular gas distributions are more likely to have high FIR-radio ratios.

6.4 Origin of the CO–radio and IR–radio relations?

6.4.1 Radio-deficient ETGs

We now review the plausibility of explanations that could conceivably cause both high CO-radio and IR-radio ratios seen in some ATLAS^{3D} ETGs. Although variations in X_{CO} and decreased SFE could be responsible for the high CO-radio ratios, they cannot explain the high IR-radio ratios. Thus, we find these explanations unlikely to be dominant factors in the deficient radio continuum emission, though it is possible that the high CO-radio and IR-radio ratios are caused by different mechanisms.

Since both FIR-radio and MIR-radio ratios tend to be high for ETGs with lower luminosities, systematic effects in the IR data sets (e.g. confusion noise at low IR luminosities and contamination from dust associated with evolved stars) are likely not the root of the observed trends. Thus, we conclude that the high q-values in some ETGs are likely the result of a genuine deficiency in the level of radio continuum emission that especially affects the lower IR luminosity and H_2 mass ETGs in our study.

In some cases, the apparent deficient radio emission is due to resolved-out emission that could not be imaged by our $\theta_{FWHM} = 5$ arcsec resolution 1.4 GHz data. However, the radio deficiency does persist in some ETGs even when data much more sensitive to extended, low-surface-brightness emission are included. Although the radio continuum emission does appear to be genuinely suppressed in some ETGs, including those with substantial reservoirs of molecular gas, the underlying cause remains unclear. Some scenarios, such as nascent SF, are highly unlikely. We

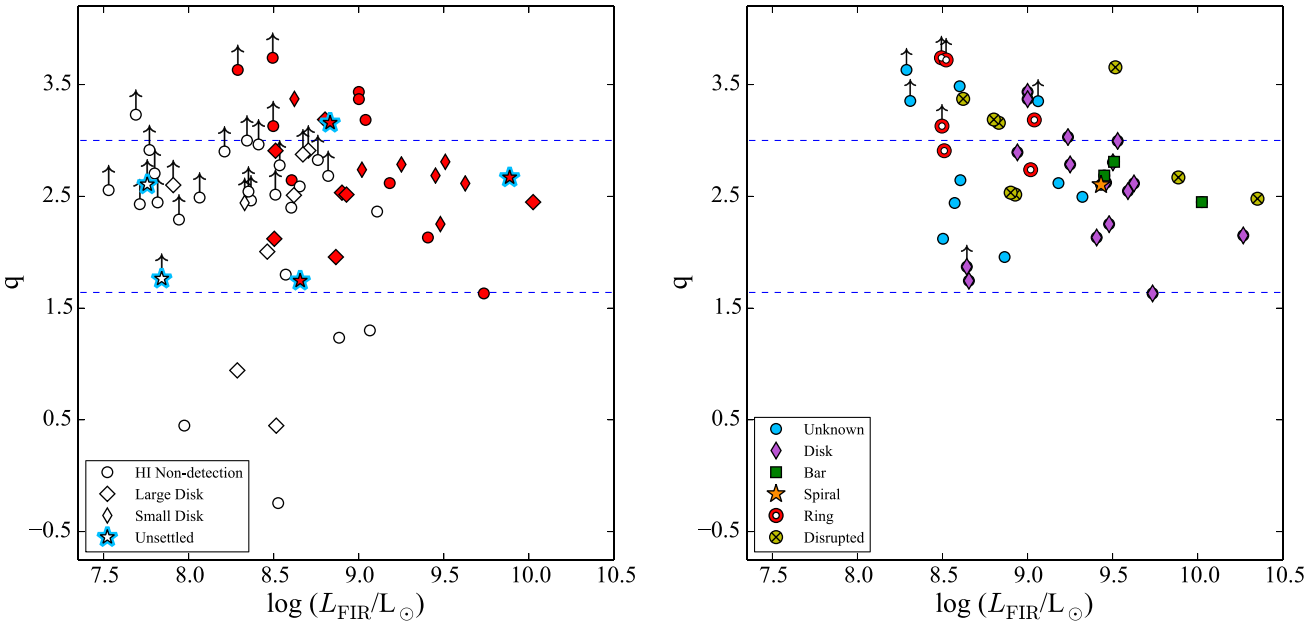

Figure 15. Logarithmic FIR-radio ratio (q) as a function of the FIR luminosity for the ATLAS^{3D} galaxies with atomic and/or molecular gas morphological information. The upper and lower dotted blue lines denote the classic divisions between sources with excess FIR ($q > 3.00$) and radio ($q < 1.64$) emission, respectively (Yun et al. 2001). Left: symbols correspond to the H I morphologies (Serra et al. 2012), defined in the legend in the bottom-left corner of the figure. Symbols representing ETGs with unsettled H I morphologies are highlighted in light blue. Symbols filled in red represent the ATLAS^{3D} IRAM single-dish CO detections, while white symbols represent CO upper limits (Young et al. 2011). Right: same as the left-hand panel, except the symbols represent the interferometric CO morphologies (Alatalo et al. 2013) as defined in the legend in the bottom-left corner of the figure.

consider the following possibilities to be the most plausible at this time: (i) weak magnetic fields, (ii) ram pressure stripping of cosmic ray electrons/gravitational harassment in dense environments, and (iii) bottom-heavy stellar IMFs. Further studies of the relationship between radio continuum emission and other SF tracers will be necessary to improve our understanding of how SF proceeds in ETGs.

6.4.2 ETGs that follow the Radio–IR relation

While some nearby ETGs are deficient in their radio continuum emission compared to the IR, we note that many of the ATLAS^{3D} galaxies, particularly those with the highest molecular gas masses, do follow the radio–IR correlation. In these systems, the radio–IR correlation likely originates from SF as it does in spirals. However, a substantial fraction of the radio emission in some of the ETGs that lie on the radio–IR relation could have an AGN rather than an SF origin. Previous studies of the radio–IR relation in low-luminosity AGNs have indeed shown that, unlike more powerful, radio-loud AGNs that show clear radio excesses when placed on the radio–IR correlation, many of these systems have q-values within the scatter of normal star-forming galaxies (Obrić et al. 2006; Mauch & Sadler 2007; Morić et al. 2010; Nyland et al. 2016).

There is evidence that some ATLAS^{3D} ETGs with normal q-values may be dominated by AGN rather than SF emission at radio and IR wavelengths. Some of the 1.4–5 GHz spectral index estimates reported in Table A6 are flat (i.e. $\alpha > -0.5$), a possible indication of self-absorbed synchrotron emission associated with an active nucleus (Condon 1992). However, these spectral indices are based on observations taken a few decades apart in time and at very different sensitivities, and we regard these crude estimates as highly uncertain.

An example of an ATLAS^{3D} ETG with strong multiwavelength evidence for the presence of an AGN that is characterized by a normal q-value is NGC1266 (Nyland et al. 2013, 2016). In this galaxy, the majority of the radio continuum emission is associated with kpc-scale radio lobes that may be interacting with the ISM of the host galaxy, yet its q-value of 2.15 is consistent with normal star-forming galaxies on the radio–IR relation. In other systems with evidence for radio AGN emission that lack extended jets/lobes and also follow the radio–IR relation, such as NGC5273 (Nyland et al. 2016), some portion of the radio continuum emission could even originate from coronal outflows from accretion discs, as recently suggested by Wong et al. (2016).

7 SUMMARY AND CONCLUSIONS

We have presented new, sensitive 1.4 GHz VLA observations of the kpc-scale radio continuum emission in 72 ETGs from the volume- and magnitude-limited ATLAS^{3D} survey. Combined with data from FIRST, we have studied the 1.4 GHz properties of 97 per cent of the ATLAS^{3D} ETGs. We detected radio continuum emission in 71 per cent of our new 1.4 GHz VLA observations on scales ranging from ≈200 to 900 pc in compact sources to as large as 18 kpc in the most extended source. For the majority of the ETGs in our sample, the 1.4 GHz emission has a morphology that is similar in appearance to the discs of radio emission associated with SF in spiral galaxies. In at least two cases, the radio morphology is characterized by extended jets, and is clearly associated with an active nucleus rather than SF.

We compared these radio data with existing molecular gas and IR observations to study the CO–radio and IR–radio relations in the largest sample of nearby ETGs to date. The main conclusions from this study are as follows.

(1) The most molecular gas rich ATLAS^{3D} ETGs have radio luminosities consistent with expectations from radio–SFR calibrations and SFRs derived from molecular gas masses (Gao & Solomon 2004; Murphy et al. 2011). The gas-rich ETGs in our sample also follow the radio–IR correlation. These ETGs may be in the process of efficiently forming stars, and SF likely proceeds in a manner similar to that in typical star-forming spiral galaxies. The radio–IR relation in these systems likely arises from SF, but for some sources harbouring low-luminosity radio AGNs, the correlation may be driven by AGN activity.

(2) ETGs with lower H_2 masses tend to emit less radio continuum emission than expected based on the standard H_2–SFR relations. This population of ETGs is also characterized by high IR-radio ratios compared to 'normal' star-forming galaxies. Correlations between the radio continuum and IR emission are similar for both FIR and MIR emission. High q-values persist in the MIR even after correction for the contribution to the 22 μm emission made by an underlying dusty, evolved stellar population.

(3) The incidence of high q-values is much higher in this sample than in previous studies of the IR–radio relation in samples dominated by late-type galaxies. About 19 per cent of our sample ETGs have high q-values and are candidate FIR-excess sources. Considering ATLAS^{3D} ETGs with only upper limits of the level of radio continuum emission, this fraction may even be as high as ≈50 per cent.

(4) By comparing to lower resolution archival radio data, we conclude that the amount of large-scale radio emission that would have been resolved-out by our higher resolution data is modest. While there are some ETGs in our study that have normal star-forming q-values when measurements are made using the lower resolution radio data, the high q-values persist in other ETGs even when data more sensitive to extended, low-surface-brightness emission are included.

(5) The high q-values in our sample tend to occur at low-IR luminosities but are not associated with low dynamical mass or metallicity. This is in contrast to previous studies that were dominated by late-type star-forming galaxies.

(6) Possible explanations that could explain both high CO-radio and IR-radio ratios in our sample of ETGs include bottom-heavy IMFs, weak magnetic fields, and a higher prevalence of environmental effects leading to enhanced cosmic ray electron escape compared to spirals.

Although our data indicate that some ETGs are deficient in their overall radio continuum emission compared to their CO and IR emission, further studies are needed to verify the underlying cause. Improved estimates of SF rates, SFEs, ISM conditions, and galactic magnetic fields in ETGs will also help improve our understanding and interpretation of the correlations discussed in this work. Examples of future studies include spectral energy distribution modelling, deep high-resolution imaging of denser molecular gas species with the Atacama Large Millimeter Array, and deep radio continuum polarization studies capable of tracing the strength and structure of the weak magnetic fields of nearby ETGs.

ACKNOWLEDGEMENTS

We thank the anonymous referee for the many thoughtful comments that have strengthened this work. The National Radio Astronomy Observatory is a facility of the National Science Foundation operated under cooperative agreement by Associated Universities, Inc. This publication makes use of data products from the *WISE*, which is a joint project of the University of California, Los Angeles, and the Jet Propulsion Laboratory/California Institute of Technology, funded by the National Aeronautics and Space Administration. We also used the NASA/IPAC Extragalactic Database (NED), which is operated by the Jet Propulsion Laboratory, California Institute of Technology, under contract with the National Aeronautics and Space Administration. Funding for this project was provided in part by National Science Foundation grant 1109803. The research leading to these results has also received funding from the European Research Council under the European Union's Seventh Framework Programme (FP/2007-2013)/ERC Advanced Grant RADIOLIFE-320745. KA is supported through Hubble Fellowship grant #HST-HF2-51352.001 awarded by the Space Telescope Science Institute, which is operated by the Association of Universities for Research in Astronomy, Inc., for NASA, under contract NAS5-26555.

Facilities: NRAO

REFERENCES

Aalto S., Muller S., Sakamoto K., Gallagher J. S., Martín S., Costagliola F., 2012, A&A, 546, A68
Adler D. S., Allen R. J., Lo K. Y., 1991, ApJ, 382, 475
Alatalo K. et al., 2013, MNRAS, 432, 1796
Alatalo K. et al., 2015, MNRAS, 450, 3874
Appleton P. N. et al., 2004, ApJS, 154, 147
Asmus D., Hönig S. F., Gandhi P., Smette A., Duschl W. J., 2014, MNRAS, 439, 1648
Athey A., Bregman J., Bregman J., Temi P., Sauvage M., 2002, ApJ, 571, 272
Bacon R. et al., 2001, MNRAS, 326, 23
Baldi R. D., Giroletti M., Capetti A., Giovannini G., Casasola V., Pérez-Torres M. A., Kuno N., 2015, A&A, 574, A65
Bastian N., Covey K. R., Meyer M. R., 2010, ARA&A, 48, 339
Beck R., 2001, Space Sci. Rev., 99, 243
Beck R., Wielebinski R., 2013, Planets, Stars and Stellar Systems Vol. 5. Springer, Dordrecht, p. 641
Becker R. H., White R. L., Helfand D. J., 1995, ApJ, 450, 559
Bell E. F., 2003, ApJ, 586, 794
Bell E. F., McIntosh D. H., Katz N., Weinberg M. D., 2003, ApJS, 149, 289
Beswick R. J., Muxlow T. W. B., Thrall H., Richards A. M. S., Garrington S. T., 2008, MNRAS, 385, 1143
Bois M. et al., 2011, MNRAS, 416, 1654
Bolatto A. D., Wolfire M., Leroy A. K., 2013, ARA&A, 51, 207
Boyle B. J., Cornwell T. J., Middelberg E., Norris R. P., Appleton P. N., Smail I., 2007, MNRAS, 376, 1182
Briggs D. S., 1995, Am. Astron. Soc. Meeting Abstr.27, 112.02
Calzetti D. et al., 2007, ApJ, 666, 870
Cappellari M. et al., 2011a, MNRAS, 413, 813
Cappellari M. et al., 2011b, MNRAS, 416, 1680
Cappellari M. et al., 2012, Nature, 484, 485
Cappellari M. et al., 2013, MNRAS, 432, 1862
Chi X., Wolfendale A. W., 1990, MNRAS, 245, 101
Cluver M. E. et al., 2014, ApJ, 782, 90
Combes F., Young L. M., Bureau M., 2007, MNRAS, 377, 1795
Condon J. J., 1992, ARA&A, 30, 575
Condon J. J., Anderson M. L., Helou G., 1991, ApJ, 376, 95
Condon J. J., Cotton W. D., Greisen E. W., Yin Q. F., Perley R. A., Taylor G. B., Broderick J. J., 1998, AJ, 115, 1693
Condon J. J., Cotton W. D., Broderick J. J., 2002, AJ, 124, 675
Conway J. E., Cornwell T. J., Wilkinson P. N., 1990, MNRAS, 246, 490
Cornwell T. J., 2008, IEEE J. Sel. Top. Signal Process., 2, 793
Crocker A. F., Bureau M., Young L. M., Combes F., 2011, MNRAS, 410, 1197
Crocker A. et al., 2012, MNRAS, 421, 1298
Cutri R. M. et al., 2013, Explanatory Supplement to the AllWISE Data Release Products. Available at: http://adsabs.harvard.edu/abs/2013wise.rept....1C

Davis T. A., Bureau M., 2016, MNRAS, 457, 272
Davis T. A. et al., 2011, MNRAS, 417, 882
Davis T. A. et al., 2013, MNRAS, 429, 534
Davis T. A. et al., 2014, MNRAS, 444, 3427
de Zeeuw P. T. et al., 2002, MNRAS, 329, 513
Dickman R. L., Snell R. L., Schloerb F. P., 1986, ApJ, 309, 326
Donoso E. et al., 2012, ApJ, 748, 80
Duc P.-A. et al., 2011, MNRAS, 417, 863
Duc P.-A. et al., 2015, MNRAS, 446, 120
Dutton A. A., Mendel J. T., Simard L., 2012, MNRAS, 422, L33
Elbaz D., Cesarsky C. J., Chanial P., Aussel H., Franceschini A., Fadda D., Chary R. R., 2002, A&A, 384, 848
Emsellem E. et al., 2007, MNRAS, 379, 401
Emsellem E. et al., 2011, MNRAS, 414, 888
Faber S. M., Gallagher J. S., 1976, ApJ, 204, 365
Filho M. E., Fraternali F., Markoff S., Nagar N. M., Barthel P. D., Ho L. C., Yuan F., 2004, A&A, 418, 429
Ford H. A., Bregman J. N., 2013, ApJ, 770, 137
Gao Y., Solomon P. M., 2004, ApJ, 606, 271
Gruppioni C., Pozzi F., Zamorani G., Ciliegi P., Lari C., Calabrese E., La Franca F., Matute I., 2003, MNRAS, 341, L1
Gunn J. E., Gott J. R., III, 1972, ApJ, 176, 1
Heesen V., Dettmar R.-J., Krause M., Beck R., Stein Y., 2016, MNRAS, 458, 332
Helou G., Soifer B. T., Rowan-Robinson M., 1985, ApJ, 298, L7
Helou G., Khan I. R., Malek L., Boehmer L., 1988, ApJS, 68, 151
Ho L. C., 2008, ARA&A, 46, 475
Jarrett T. H. et al., 2013, AJ, 145, 6
Jeong H. et al., 2009, MNRAS, 398, 2028
Kaviraj S. et al., 2007, ApJS, 173, 619
Kennicutt R. C., Evans N. J., 2012, ARA&A, 50, 531
Kennicutt R. C., Jr1998, ApJ, 498, 541
Khochfar S. et al., 2011, MNRAS, 417, 845
Knapp G. R., Rupen M. P., 1996, ApJ, 460, 271
Knapp G. R., Gunn J. E., Wynn-Williams C. G., 1992, ApJ, 399, 76
Kroupa P., Weidner C., 2003, ApJ, 598, 1076
Lacki B. C., Thompson T. A., Quataert E., 2010, ApJ, 717, 1
Läsker R., van den Bosch R. C. E., van de Ven G., Ferreras I., La Barbera F., Vazdekis A., Falcón-Barroso J., 2013, MNRAS, 434, L31
Lee J. C., Hwang H. S., Ko J., 2013, ApJ, 774, 62
Lerche I., Schlickeiser R., 1980, ApJ, 239, 1089
Leroy A. K. et al., 2013, AJ, 146, 19
Liu F., Gao Y., 2010, ApJ, 713, 524
Liu L., Gao Y., Greve T. R., 2015, ApJ, 805, 31
Lucero D. M., Young L. M., 2007, AJ, 134, 2148
McDermid R. M. et al., 2012, in Tuffs R. J., Popescu C. C., eds, Proc. IAU Symp. 284, The Spectral Energy Distribution of Galaxies. Cambridge Univ. Press, Cambridge, p. 244
McDermid R. M. et al., 2015, MNRAS, 448, 3484
Madau P., Dickinson M., 2014, ARA&A, 52, 415
Marigo P., Girardi L., Bressan A., Groenewegen M. A. T., Silva L., Granato G. L., 2008, A&A, 482, 883
Martig M., Bournaud F., Teyssier R., Dekel A., 2009, ApJ, 707, 250
Martig M. et al., 2013, MNRAS, 432, 1914
Martín-Navarro I. et al., 2015, ApJ, 806, L31
Marvil J., Owen F., Eilek J., 2015, AJ, 149, 32
Mason R. E. et al., 2012, AJ, 144, 11
Mathews W. G., Brighenti F., 2003, ApJ, 590, L5
Mauch T., Sadler E. M., 2007, MNRAS, 375, 931
Meier D. S., Turner J. L., 2004, AJ, 127, 2069
Miller N. A., Owen F. N., 2001, AJ, 121, 1903
Moore B., Lake G., Katz N., 1998, ApJ, 495, 139
Morganti R. et al., 2006, MNRAS, 371, 157
Morić I., Smolčić V., Kimball A., Riechers D. A., Ivezić Ž., Scoville N., 2010, ApJ, 724, 779
Murgia M., Crapsi A., Moscadelli L., Gregorini L., 2002, A&A, 385, 412
Murgia M., Helfer T. T., Ekers R., Blitz L., Moscadelli L., Wong T., Paladino R., 2005, A&A, 437, 389
Murphy E. J., Kenney J. D. P., Helou G., Chung A., Howell J. H., 2009, ApJ, 694, 1435
Murphy E. J. et al., 2011, ApJ, 737, 67
Naab T. et al., 2014, MNRAS, 444, 3357
Nyland K. et al., 2013, ApJ, 779, 173
Nyland K. et al., 2016, MNRAS, 458, 2221
Obrić M. et al., 2006, MNRAS, 370, 1677
Oosterloo T. et al., 2010, MNRAS, 409, 500
Perley R. A., Butler B. J., 2013, ApJS, 204, 19
Posacki S., Cappellari M., Treu T., Pellegrini S., Ciotti L., 2015, MNRAS, 446, 493
Ramos Almeida C. et al., 2011, MNRAS, 417, L46
Rau U., Cornwell T. J., 2011, A&A, 532, A71
Reddy N. A., Yun M. S., 2004, ApJ, 600, 695
Rieke G. H., Alonso-Herrero A., Weiner B. J., Pérez-González P. G., Blaylock M., Donley J. L., Marcillac D., 2009, ApJ, 692, 556
Roussel H., Helou G., Beck R., Condon J. J., Bosma A., Matthews K., Jarrett T. H., 2003, ApJ, 593, 733
Rujopakarn W., Rieke G. H., Weiner B. J., Pérez-González P., Rex M., Walth G. L., Kartaltepe J. S., 2013, ApJ, 767, 73
Sadler E. M., Jenkins C. R., Kotanyi C. G., 1989, MNRAS, 240, 591
Saintonge A. et al., 2012, ApJ, 758, 73
Sandstrom K. M. et al., 2013, ApJ, 777, 5
Sargent M. T. et al., 2010, ApJS, 186, 341
Sarzi M. et al., 2006, MNRAS, 366, 1151
Sarzi M. et al., 2010, MNRAS, 402, 2187
Scott N. et al., 2013, MNRAS, 432, 1894
Seaquist E. R., Odegard N., 1991, ApJ, 369, 320
Serra P. et al., 2012, MNRAS, 422, 1835
Serra P. et al., 2014, MNRAS, 444, 3388
Shi F., Kong X., Wicker J., Chen Y., Gong Z.-Q., Fan D.-X., 2012, J. Astrophys. Astron., 33, 213
Skrutskie M. F. et al., 2006, AJ, 131, 1163
Smith R. J., Lucey J. R., Carter D., 2012, MNRAS, 426, 2994
Sodroski T. J. et al., 1995, ApJ, 452, 262
Soifer B. T., Neugebauer G., Houck J. R., 1987, ARA&A, 25, 187
Solomon P. M., Vanden Bout P. A., 2005, ARA&A, 43, 677
Strong A. W., Moskalenko I. V., Reimer O., Digel S., Diehl R., 2004, A&A, 422, L47
Tabatabaei F. S. et al., 2013, A&A, 552, A19
Temi P., Brighenti F., Mathews W. G., 2007, ApJ, 660, 1215
Temi P., Brighenti F., Mathews W. G., 2009, ApJ, 707, 890
Tonnesen S., Bryan G. L., 2009, ApJ, 694, 789
van Dokkum P. G., Conroy C., 2012, ApJ, 760, 70
Vollmer B., Cayatte V., van Driel W., Henning P. A., Kraan-Korteweg R. C., Balkowski C., Woudt P. A., Duschl W. J., 2001, A&A, 369, 432
Walsh D. E. P., Knapp G. R., Wrobel J. M., Kim D.-W., 1989, ApJ, 337, 209
Welch G. A., Sage L. J., 2003, ApJ, 584, 260
Wen X.-Q., Wu H., Zhu Y.-N., Lam M. I., Wu C.-J., Wicker J., Long R. J., Zhao Y.-H., 2014, MNRAS, 438, 97
Werner N. et al., 2014, MNRAS, 439, 2291
Wiegert T. et al., 2015, AJ, 150, 81
Wong O. I. et al., 2016, MNRAS, 460, 1588
Wright E. L. et al., 2010, AJ, 140, 1868
Wrobel J. M., 1991, AJ, 101, 127
Wrobel J. M., Heeschen D. S., 1991, AJ, 101, 148
Xilouris E. M., Madden S. C., Galliano F., Vigroux L., Sauvage M., 2004, A&A, 416, 41
Yi S. K. et al., 2005, ApJ, 619, L111
York D. G. et al., 2000, AJ, 120, 1579
Young L. M., Bureau M., Cappellari M., 2008, ApJ, 676, 317
Young L. M. et al., 2011, MNRAS, 414, 940
Yun M. S., Reddy N. A., Condon J. J., 2001, ApJ, 554, 803

APPENDIX A: DATA TABLES

Table A1. 1.4 GHz VLA image properties.

Galaxy	D (Mpc)	Virgo	F/S	rms (μJy beam^{-1})	$S_{\rm peak}$ (mJy beam^{-1})	$S_{\rm int}$ (mJy)	log(L) (W Hz^{-1})
(1)	(2)	(3)	(4)	(5)	(6)	(7)	(8)
IC0676	24.6	0	F	43	3.44 ± 0.04	6.78 ± 0.23	20.69
IC0719[a]	29.4	0	F	28	0.18 ± 0.02	2.15 ± 0.28	20.35
IC1024	24.2	0	F	67	3.57 ± 0.03	17.52 ± 0.56	21.09
NGC0474	30.9	0	F	40	<0.20	–	<19.36
NGC0509	32.3	0	F	28	<0.14	–	<19.24
NGC0516	34.7	0	F	27	<0.14	–	<19.29
NGC0524	23.3	0	F	29	1.36 ± 0.02	1.63 ± 0.07	20.02
NGC0525	30.7	0	F	29	<0.14	–	<19.21
NGC0680	37.5	0	F	27	0.99 ± 0.02	1.12 ± 0.05	20.28
NGC0770	36.7	0	F	34	<0.17	–	<19.44
NGC0821	23.4	0	F	31	<0.15	–	<19.01
NGC1023	11.1	0	F	36	0.23 ± 0.03	0.56 ± 0.11	18.92
[b]NGC1222	33.3	0	S	70	16.24 ± 0.02	48.64 ± 1.46	21.81
NGC1266	29.9	0	F	70	62.52 ± 0.03	106.60 ± 3.20	22.06
NGC2685[a]	16.7	0	F	29	1.05 ± 0.01	44.91 ± 1.40	21.18
NGC2764	39.6	0	F	40	2.44 ± 0.03	15.13 ± 0.51	21.45
NGC2768	21.8	0	F	42	13.48 ± 0.02	13.65 ± 0.41	20.89
NGC2824	40.7	0	F	42	6.95 ± 0.04	–	21.14
NGC2852	28.5	0	F	35	0.71 ± 0.03	–	19.84
NGC3032	21.4	0	F	39	0.78 ± 0.03	5.42 ± 0.27	20.47
NGC3073	32.8	0	F	52	<0.26	–	<19.52
NGC3182[a]	21.8	0	F	30	0.13 ± 0.01	4.29 ± 0.47	20.39
NGC3193	34.0	0	F	30	0.24 ± 0.03	0.48 ± 0.08	19.82
NGC3156	33.1	0	F	32	<0.16	–	<19.32
NGC3245	20.3	0	F	33	6.28 ± 0.03	7.05 ± 0.22	20.54
NGC3489	11.7	0	F	35	0.43 ± 0.03	0.84 ± 0.10	19.14
NGC3599	19.8	0	F	40	<0.20	–	<18.97
NGC3605	20.1	0	F	27	<0.14	–	<18.81
NGC3607	22.2	0	F	28	4.37 ± 0.02	5.47 ± 0.17	20.51
NGC3608	22.3	0	S	27	0.33 ± 0.03	–	19.29
[b]NGC3619[a]	26.8	0	F	36	1.03 ± 0.03	3.00 ± 0.14	20.41
NGC3626	19.5	0	F	40	2.92 ± 0.03	4.55 ± 0.15	20.32
NGC3648	31.9	0	F	30	0.36 ± 0.02	0.54 ± 0.06	19.82
[b]NGC3665[a]	33.1	0	F	40	11.99 ± 0.02	88.46 ± 2.66	22.06
NGC3945[a]	23.2	0	F	34	1.63 ± 0.03	–	20.02
NGC4036	24.6	0	F	50	8.96 ± 0.03	10.76 ± 0.33	20.89
NGC4111	14.6	0	F	48	4.55 ± 0.05	7.69 ± 0.26	20.29
NGC4119	16.5	1	F	35	<0.17	–	<18.76
NGC4150	13.4	0	F	29	0.66 ± 0.02	0.82 ± 0.05	19.25
NGC4203	14.7	0	F	78	8.49 ± 0.06	–	20.34
NGC4324	16.5	1	F	39	<0.20	–	<18.80
NGC4429	16.5	1	F	40	0.48 ± 0.03	1.12 ± 0.10	19.56
NGC4459	16.1	1	F	40	1.14 ± 0.03	1.39 ± 0.07	19.63
NGC4526	16.4	1	F	30	1.89 ± 0.02	9.75 ± 0.33	20.50
NGC4550	15.5	1	S	50	<0.25	–	<18.86
NGC4551	16.1	1	F	44	<0.22	–	<18.83
NGC4564	15.8	1	F	31	<0.15	–	<18.67
NGC4596	16.5	1	F	28	<0.14	–	<18.66
NGC4643	16.5	1	F	29	0.24 ± 0.03	0.41 ± 0.07	19.13
NGC4684	13.1	0	F	45	3.51 ± 0.05	5.31 ± 0.19	20.04
NGC4694	16.5	1	F	35	0.90 ± 0.03	1.44 ± 0.07	19.67
NGC4697	11.4	0	F	38	<0.19	–	<18.47
NGC4710	16.5	1	F	28	2.63 ± 0.02	13.30 ± 0.42	20.64
NGC4753	22.9	0	F	40	0.33 ± 0.03	1.14 ± 0.12	19.85
NGC5173	38.4	0	F	32	1.24 ± 0.03	–	20.34
NGC5273[c]	16.1	0	F	–	–	–	–
NGC5379	30.0	0	F	30	0.46 ± 0.03	–	19.69
[b]NGC5866[a]	14.9	0	F	40	12.14 ± 0.04	14.14 ± 0.43	20.57

Table A1 – *continued*

Galaxy	D (Mpc)	Virgo	F/S	rms (μJy beam^{-1})	$S_{\rm peak}$ (mJy)	$S_{\rm int}$ (mJy)	log(L) (W Hz^{-1})
(1)	(2)	(3)	(4)	(5)	(6)	(7)	(8)
NGC6014[a]	35.8	0	F	38	2.75 ± 0.03	3.63 ± 0.12	20.75
NGC6547	40.8	0	F	37	1.74 ± 0.03	2.48 ± 0.10	20.69
NGC6798	37.5	0	F	29	0.25 ± 0.03	–	19.62
NGC7457	23.2	0	S	29	<0.14	–	<18.97
NGC7454	12.9	0	F	27	<0.14	–	<18.43
NGC7465	29.3	0	F	32	7.98 ± 0.03	13.38 ± 0.41	21.14
PGC016060	37.8	0	F	60	<0.30	–	<19.71
PGC029321	40.9	0	F	45	9.04 ± 0.04	–	21.26
PGC056772	39.5	0	F	28	2.18 ± 0.03	3.14 ± 0.11	20.77
PGC058114	23.8	0	F	30	6.12 ± 0.03	8.83 ± 0.27	20.78
PGC061468	36.2	0	F	36	<0.18	–	<19.45
UGC05408	45.8	0	F	41	2.58 ± 0.03	3.78 ± 0.13	20.98
UGC06176	40.1	0	F	29	4.81 ± 0.03	6.17 ± 0.19	21.07
UGC09519	27.6	0	F	27	0.25 ± 0.02	0.45 ± 0.06	19.61

Notes. Column 1: galaxy name. Column 2: official ATLAS^{3D} distance (Cappellari et al. 2011a). Column 3: Virgo membership. Column 4: kinematic class (Emsellem et al. 2011) of either fast rotator (F) or slow rotator (S). Column 5: average rms noise in the image. Column 6: peak flux density. Column 7: integrated flux density. Note that measurements of the integrated flux density are only given for sources that were resolved by JMFIT. Column 8: log of the 1.4 GHz radio luminosity. When an integrated flux density is given, log (L) is based on the integrated flux density. If only a peak flux density is given (either a measurement or an upper limit), then log (L) is based on the peak flux density.

[a]Multicomponent source. The integrated flux density refers to the sum of all components. See Table A3 for information on individual components.

[b]Extended source not well represented by a single two-dimensional Gaussian model. The peak and integrated flux densities were calculated by drawing an aperture at the 3σ level around the source in the CASA VIEWER and then using the IMSTAT task to determine the flux density.

[c]The NGC5273 data set was of poor quality and the resultant flux density measurements were deemed unreliable. This galaxy is, however, detected robustly in the FIRST survey and is therefore included in the analysis in this work as a 'detection'.

Table A2. Spatial parameters of 1.4 GHz detections.

Galaxy	Morph.	RA (J2000)	Dec. (J2000)	Beam (arcsec)	B.P.A. (°)	$\theta_{\rm M} \times \theta_{\rm m}$ (arcsec)	P.A. (°)	$M \times m$ (kpc)
(1)	(2)	(3)	(4)	(5)	(6)	(7)	(8)	(9)
IC0676	R	11:12:39.764	09:03:23.19	3.68×3.06	18.04	$4.39 \pm 0.13 \times 2.25 \pm 0.14$	164.95 ± 2.65	0.52×0.27
IC0719[a]	R	11:40:18.411	09:00:34.36	6.31×4.16	−64.62	$29.96 \pm 4.76 \times 8.21 \pm 2.05$	49.74 ± 4.88	4.27×1.17
IC1024	R	14:31:27.142	03:00:30.94	6.32×4.15	−52.95	$13.17 \pm 0.17 \times 6.88 \pm 0.15$	27.68 ± 1.04	1.55×0.81
NGC0524	R	01:24:47.737	09:32:20.02	5.56×3.76	−53.95	$2.31 \pm 0.41 \times 1.48 \pm 0.61$	70.08 ± 25.00	0.26×0.17
NGC0680	R	01:49:47.297	21:58:15.06	5.16×3.80	−65.91	$1.74 \pm 0.47 \times 1.07 \pm 0.83$	86.66 ± 38.48	0.32×0.19
NGC1023	R	02:40:23.860	39:03:47.20	5.17×3.79	−66.08	$13.26 \pm 2.79 \times 0.00 \pm 0.00$	70.50 ± 2.96	0.71×0.00
[b]NGC1222	R	03:08:56.786	−02:57:18.40	4.96×3.85	−68.11	24.99×19.77	–	4.03×3.19
NGC1266	R	03:16:0.739	−02:25:39.21	4.95×3.85	−68.43	$4.92 \pm 0.01 \times 2.15 \pm 0.01$	174.44 ± 0.14	0.71×0.31
NGC2685[a]	R	08:55:25.186	58:44:42.47	4.05×3.85	24.36	$95.24 \pm 1.04 \times 5.19 \pm 0.08$	117.10 ± 0.06	7.71×0.42
NGC2764	R	09:08:17.526	21:26:35.88	3.88×3.57	79.60	$13.78 \pm 0.27 \times 5.79 \pm 0.18$	28.96 ± 1.10	2.65×1.11
NGC2768	R	09:11:37.413	60:02:14.91	3.85×3.73	65.61	$0.55 \pm 0.11 \times 0.25 \pm 0.19$	87.33 ± 16.89	0.06×0.03
NGC2824	U	09:19:2.231	26:16:11.85	3.91×3.46	62.14	<2.36	–	<0.47
NGC2852	U	09:23:14.637	40:09:49.76	5.23×4.14	−30.76	<2.30	–	<0.32
NGC3032	R	09:52:8.169	29:14:11.46	5.77×3.28	30.77	$12.10 \pm 0.74 \times 9.60 \pm 0.70$	42.38 ± 13.45	1.26×1.00
NGC3182[a]	R	10:19:32.749	58:12:28.65	4.36×3.11	−70.13	$34.51 \pm 4.64 \times 13.25 \pm 1.97$	151.68 ± 5.23	3.65×1.40
NGC3193	R	10:18:24.896	21:53:38.51	5.35×3.16	72.76	$6.50 \pm 2.02 \times 2.95 \pm 2.46$	153.57 ± 30.05	1.07×0.49
NGC3245	R	10:27:18.377	28:30:26.60	4.36×3.12	−66.76	$1.76 \pm 0.13 \times 0.98 \pm 0.29$	0.92 ± 80.34	0.17×0.10
NGC3489	R	11:00:18.532	13:54:4.51	5.26×3.80	62.20	$5.96 \pm 1.36 \times 2.73 \pm 1.47$	66.77 ± 18.03	0.34×0.15
NGC3607	R	11:16:54.677	18:03:6.43	5.55×3.78	−87.13	$2.04 \pm 0.09 \times 1.51 \pm 0.13$	118.13 ± 8.48	0.22×0.16
NGC3608	U	11:16:58.947	18:08:55.19	5.46×3.64	−81.04	<2.68	–	<0.29
[b]NGC3619[a]	R	11:19:21.586	57:45:27.83	5.75×3.01	80.71	13.57×9.18	–	1.76×1.19
NGC3626	R	11:20:3.810	18:21:24.54	4.74×3.16	−80.60	$4.82 \pm 0.14 \times 2.66 \pm 0.11$	107.13 ± 2.33	0.46×0.25
NGC3648	R	11:22:31.448	39:52:37.01	6.02×4.02	−71.00	$4.90 \pm 1.09 \times 0.44 \pm 1.34$	143.52 ± 16.66	0.76×0.07
[b]NGC3665[a]	R	11:24:43.662	38:45:46.13	8.37×3.42	51.92	112.76×20.12	–	18.09×3.23
NGC3945[a]	U	11:53:13.624	60:40:32.15	5.49×3.59	62.63	<1.59	–	<0.18
NGC4036	R	12:01:26.656	61:53:44.03	6.11×3.10	43.70	$3.61 \pm 0.15 \times 1.76 \pm 0.07$	67.04 ± 2.53	0.43×0.21
NGC4111	R	12:07:3.146	43:03:56.24	4.40×3.58	−81.89	$3.43 \pm 0.10 \times 2.62 \pm 0.10$	60.88 ± 5.07	0.24×0.19
NGC4150	R	12:10:33.656	30:24:5.80	3.92×3.37	44.45	$2.44 \pm 0.70 \times 1.59 \pm 1.19$	28.58 ± 47.71	0.16×0.10
NGC4203	U	12:15:5.055	33:11:50.34	3.92×3.37	44.42	<0.85	–	<0.06
NGC4429	R	12:27:26.482	11:06:27.67	3.91×3.37	44.50	$8.68 \pm 1.17 \times 3.62 \pm 0.71$	105.47 ± 7.29	0.69×0.29

Table A2 – *continued*

Galaxy	Morph.	RA (J2000)	Dec. (J2000)	Beam (arcsec)	B.P.A. (°)	$\theta_M \times \theta_m$ (arcsec)	P.A. (°)	$M \times m$ (kpc)
(1)	(2)	(3)	(4)	(5)	(6)	(7)	(8)	(9)
NGC4459	R	12:29:0.027	13:58:42.53	5.42 × 3.15	86.60	2.51 ± 0.63 × 1.64 ± 1.08	69.42 ± 36.22	0.20 × 0.13
NGC4526	R	12:34:2.994	07:41:58.03	5.85 × 3.99	− 71.56	12.14 ± 0.22 × 3.13 ± 0.13	110.82 ± 0.62	0.97 × 0.25
NGC4643	R	12:43:20.133	01:58:41.83	5.77 × 3.84	− 85.22	8.47 ± 2.19 × 1.48 ± 1.27	41.53 ± 9.63	0.68 × 0.12
NGC4684	R	12:47:17.522	−02:43:38.38	6.45 × 3.80	− 77.47	3.67 ± 0.16 × 1.88 ± 0.19	11.63 ± 4.20	0.23 × 0.12
NGC4694	R	12:48:14.994	10:59:2.12	4.43 × 4.26	63.35	5.74 ± 0.41 × 2.02 ± 0.39	113.85 ± 4.01	0.46 × 0.16
NGC4710	R	12:49:38.821	15:09:56.32	9.92 × 3.45	57.78	10.96 ± 0.13 × 3.55 ± 0.07	27.03 ± 0.46	0.88 × 0.28
NGC4753	R	12:52:21.907	−01:11:58.60	3.73 × 3.53	64.43	14.68 ± 1.70 × 2.23 ± 1.65	97.95 ± 3.42	1.63 × 0.25
NGC5173	U	13:28:25.271	46:35:29.81	6.79 × 3.39	50.66	<2.92	–	<0.54
NGC5379	U	13:55:34.343	59:44:34.17	3.68 × 2.64	− 29.64	<3.04	–	<0.44
[b]NGC5866[a]	R	15:06:29.491	55:45:47.62	6.16 × 4.08	− 54.85	65.63 × 10.21	–	4.74 × 0.74
NGC6014[a]	R	15:55:57.389	05:55:54.98	6.57 × 3.73	− 68.92	3.14 ± 0.29 × 2.70 ± 0.36	169.26 ± 56.73	0.54 × 0.47
NGC6547	R	18:05:10.806	25:13:40.71	5.18 × 3.94	− 73.00	5.78 ± 0.68 × 0.00 ± 0.75	73.16 ± 7.97	1.14 × 0.00
NGC6798	U	19:24:3.133	53:37:29.78	3.70 × 3.16	− 177.60	<2.81	–	<0.51
NGC7465	R	23:02:0.973	15:57:53.16	3.70 × 3.14	33.77	5.11 ± 0.07 × 4.01 ± 0.04	75.91 ± 2.25	0.73 × 0.57
PGC029321	U	10:05:51.178	12:57:40.45	3.69 × 3.14	33.80	<1.29	–	<0.26
PGC056772	R	16:02:11.606	07:05:9.79	3.54 × 3.11	− 166.44	3.42 ± 0.24 × 2.20 ± 0.21	23.05 ± 8.50	0.65 × 0.42
PGC058114	R	16:26:4.235	02:54:23.82	3.58 × 3.11	− 5.81	2.67 ± 0.08 × 2.10 ± 0.10	79.27 ± 6.10	0.31 × 0.24
UGC05408	R	10:03:51.896	59:26:10.48	6.83 × 3.27	44.89	3.02 ± 0.20 × 2.62 ± 0.10	82.00 ± 28.46	0.67 × 0.58
UGC06176	R	11:07:24.674	21:39:25.46	4.18 × 3.54	− 7.27	2.34 ± 0.08 × 1.56 ± 0.10	31.29 ± 5.14	0.45 × 0.30
UGC09519	R	14:46:21.106	34:22:13.73	5.61 × 3.99	− 70.15	4.65 ± 0.93 × 1.05 ± 1.20	107.28 ± 12.18	0.62 × 0.14

Notes. Column 1: galaxy name. Column 2: radio morphology based on the output of the JMFIT task in AIPS. R = resolved and U = unresolved. Column 3: right ascension of the emission at the peak flux density. For sources with multiple components denoted by a † symbol, the position listed is that of the component closest to the optical nuclear position. The format is sexagesimal and the epoch is J2000. The positional uncertainty of each image is 0.1 arcsec and is dominated by the positional uncertainty of the phase reference calibrator. Column 4: declination of the central position of the emission, determined in the same manner as the right ascension in Column 3. Column 5: angular dimensions of the synthesized beam (major × minor axis). Column 6: synthesized beam position angle, measured anticlockwise from north. Column 7: angular dimensions of the emission (major × minor axis). If JMFIT was only able to deconvolve the major axis of the source, then the minor axis extent is given as 0.00. The errors are from JMFIT and are only given if the emission was successfully deconvolved in at least one dimension and categorized as resolved. For non-Gaussian sources, source dimensions were determined using the CASA VIEWER and no error is reported. Column 8: position angle of the emission from JMFIT. For non-Gaussian, inherently complex sources, no position angle is reported. Column 9: linear dimensions of the emission (major × minor axis) in physical units.

[a]Multicomponent source. The integrated flux density refers to the sum of all components. See Table A3 for information on all components.

[b]Extended source not well represented by a single two-dimensional Gaussian model. The peak and integrated flux densities were calculated by drawing an aperture at the 3σ level around the source in the CASA VIEWER and then using the IMSTAT task to determine the flux density.

Table A3. Image properties of sources with multiple components.

Galaxy	Component	RA (J2000)	Dec. (J2000)	$S_{\rm peak}$ (mJy beam^{-1})	$S_{\rm int}$ (mJy)	log(L) (W Hz^{-1})
(1)	(2)	(3)	(4)	(5)	(6)	(7)
IC0719	[a]Central source	11:40:18.588	09:00:36.77	0.20 ± 0.03	0.37 ± 0.06	19.58
	[a]Southern source	11:40:18.154	09:00:31.71	0.20 ± 0.03	0.32 ± 0.05	19.52
	[a]Northern source	11:40:18.862	09:00:41.68	0.17 ± 0.03	–	19.25
NGC2685	Northern source	08:55:33.694	58:44:8.43	0.33 ± 0.02	0.61 ± 0.05	19.31
	Southern source	08:55:34.477	58:44:4.09	0.15 ± 0.02	1.08 ± 0.15	19.56
NGC3182	[a]Northern source	10:19:33.043	58:12:25.17	0.23 ± 0.03	0.52 ± 0.16	19.47
	[a]Western source	10:19:33.589	58:12:15.74	0.19 ± 0.03	0.50 ± 0.19	19.45
	[a]Eastern source	10:19:32.474	58:12:20.16	0.16 ± 0.03	0.41 ± 0.18	19.37
NGC3619	[a]Southern source	11:19:21.755	57:45:25.90	1.13 ± 0.05	1.43 ± 0.12	20.09
	[a]Northern source	11:19:21.476	57:45:29.14	0.89 ± 0.05	1.18 ± 0.11	20.01
NGC3665	[a]Eastern jet	11:24:43.277	38:45:49.79	13.35 ± 0.40	37.94 ± 1.60	21.70
	[a]Western jet	11:24:44.221	38:45:40.84	13.38 ± 0.40	38.24 ± 1.40	21.70
	[a]Core	11:24:43.012	38:45:52.23	12.21 ± 0.37	18.72 ± 0.64	21.39
NGC3945	Northern source	11:53:13.625	60:40:32.15	1.64 ± 0.03	–	20.02
	Southern source	11:53:13.473	60:40:21.17	0.42 ± 0.03	–	19.43
NGC5866	Central source	15:06:29.491	55:45:47.62	12.14 ± 0.04	14.14 ± 0.43	20.57
	[a]Northern source	15:06:34.984	55:45:20.19	0.64 ± 0.04	4.28 ± 1.50	20.06
	[a]Southern source	15:06:23.306	55:46:29.15	0.95 ± 0.05	2.26 ± 1.08	19.78
NGC6014	Central source	15:55:57.389	05:55:54.98	2.75 ± 0.03	3.63 ± 0.12	20.75
	Northern source	15:55:56.695	05:56:11.46	0.47 ± 0.03	–	19.86

Notes. Column 1: galaxy name. Column 2: radio component name. Column 3: right ascension of the central position of the component as determined by IMFIT in CASA. The format is sexagesimal and the epoch is J2000. The positional uncertainty of each image is 0.1 arcsec and is dominated by the positional uncertainty of the phase reference calibrator. Column 4: declination of the central position of the emission, determined in the same manner as the right ascension in Column 3. Column 5: peak flux density. Column 6: integrated flux density. Note that measurements of the integrated flux density are only given for sources that were resolved by JMFIT. Column 7: log of the 1.4 GHz radio luminosity. When an integrated flux density is given, log (L) is based on the integrated flux density. If only a peak flux density is given (either a measurement or an upper limit), then log (L) is based on the peak flux density.

[a]Extended source not well represented by a single two-dimensional Gaussian model. The peak and integrated flux densities were calculated by drawing an aperture at the 3σ level around the source in the CASA VIEWER and then using the IMSTAT task to determine the flux density.

Table A4. Spatial properties of sources with multiple components.

Galaxy	Component	Morph.	$\theta_M \times \theta_m$ (arcsec)	P.A. (°)	$M \times m$ (kpc)
(1)	(2)	(3)	(4)	(5)	(6)
IC0719	[a]Central source	R	10.67×9.59	–	1.52×1.37
	[a]Southern source	R	13.55×9.95	–	1.93×1.42
	[a]Northern source	R	8.49×6.37	–	1.21×0.91
NGC2685	Northern source	R	$4.34 \pm 0.76 \times 2.32 \pm 0.92$	75.75 ± 18.24	0.35×0.19
	Southern source	R	$18.54 \pm 3.07 \times 3.96 \pm 1.04$	105.15 ± 3.79	1.50×0.32
NGC3182	[a]Northern source	R	8.78×4.38	–	0.93×0.46
	[a]Western source	R	7.52×3.28	–	0.79×0.35
	[a]Eastern source	R	11.11×3.62	–	1.17×0.38
NGC3619	[a]Southern source	R	9.22×6.59	–	1.20×0.86
	[a]Northern source	R	9.83×6.78	–	1.28×0.88
NGC3665	[a]Eastern jet	R	28.78×14.23	–	4.62×2.28
	[a]Western jet	R	42.01×15.72	–	6.74×2.52
	[a]Core	R	20.12×7.33	–	3.23×1.18
NGC3945	Northern source	U	<1.57	–	<0.18
	Southern source	U	<2.62	–	<0.29
NGC5866	Central source	R	$2.69 \pm 0.08 \times 1.18 \pm 0.07$	116.29 ± 2.20	0.19×0.09
	[a]Northern source	R	25.95×10.47	–	1.87×0.76
	[a]Southern source	R	19.88×6.97	–	1.44×0.50
NGC6014	Central source	R	$3.13 \pm 0.29 \times 2.67 \pm 0.37$	170.19 ± 57.68	0.54×0.46
	Northern source	U	<3.56	–	<0.62

Notes. Column 1: galaxy name. Column 2: radio component name. Column 3: radio morphology based on the output of the JMFIT task in AIPS. R = resolved and U = unresolved. Column 4: angular dimensions of the emission (major × minor axis). If JMFIT was only able to deconvolve the major axis of the source, then the minor axis extent is given as 0.00. The errors are from JMFIT and are only given if the emission was successfully deconvolved in at least one dimension and categorized as resolved. For non-Gaussian sources, source dimensions were determined using the CASA VIEWER and no error is reported. Column 5: position angle of the emission from JMFIT. For non-Gaussian, inherently complex sources, no position angle is reported. Column 6: linear dimensions of the emission (major × minor axis) in physical units.

[a]Extended source not well represented by a single two-dimensional Gaussian model. The peak and integrated flux densities were calculated by drawing an aperture at the 3σ level around the source in the CASA VIEWER and then using the IMSTAT task to determine the flux density.

Table A5. Summary of radio, CO and IR data.

Galaxy	$S_{\rm NVSS}$ (mJy)	$S_{\rm FIRST}$ (mJy)	$S_{\rm VLA}$ (mJy)	$S_{\rm Wrobel}$ (mJy)	$\alpha_{1.4\,\rm GHz}^{5\,\rm GHz}$	$\log(M_{\rm H2})$ ($M_\odot$)	$S_{60\,\mu\rm m}$ (Jy)	$S_{100\,\mu\rm m}$ (Jy)	q	$S_{22\,\mu\rm m}$ (mJy)	$\log(L_{22\,\mu\rm m})$ (erg s^{-1})	$q_{22\,\mu\rm m}$
(1)	(2)	(3)	(4)	(5)	(6)	(7)	(8)	(9)	(10)	(11)	(12)	(13)
IC0560[a]	–	<0.74	–	–	–	<7.67	–	–	–	18.53	41.26	>1.24
IC0598	–	<0.67	–	–	–	<8.02	0.10	0.39	>2.52	7.81	<41.20	–
IC0676	9.7 ± 0.5	7.25 ± 0.73	6.78 ± 0.31	3.60 ± 0.20	1.73	8.63	3.21	5.15	2.80	544.46	42.73	1.89
IC0719[bc]	4.6 ± 0.5	<0.68	1.54 ± 0.35	<0.50	<0.09	8.26	0.87	2.65	3.03	59.26	41.88	1.59
IC0782	–	<0.76	–	–	–	<7.92	–	–	–	1.24	<40.97	–
IC1024[c]	24.7 ± 1.2	16.69 ± 1.67	17.52 ± 0.77	11.30 ± 1.00	2.68	8.61	4.10	7.80	2.55	301.69	42.46	1.24
IC3631	–	<0.74	–	–	–	<7.94	–	–	–	4.17	40.92	>1.43
NGC0448	–	<0.70	–	–	–	<7.74	0.24	0.34	–	5.04	<41.37	–
NGC0474	–	<0.62	<0.20	<0.50	<0.09	<7.68	0.03	0.10	–	8.86	<41.73	–
NGC0502	–	<0.59	–	<0.50	–	<7.88	0.07	0.10	–	1.80	<41.38	–
NGC0509	–	<0.66	<0.14	–	–	7.48	–	–	–	5.68	40.81	>1.07
NGC0516	–	<0.59	<0.14	–	–	<7.82	–	–	–	1.18	<41.05	–
NGC0524	3.1 ± 0.4	0.73 ± 0.07	1.63 ± 0.09	1.40 ± 0.10	0.94	7.97	0.76	2.05	2.89	67.54	<42.05	<1.59
NGC0525	–	<0.66	<0.14	–	–	<7.75	–	–	–	2.85	<40.91	–
NGC0661	–	–	–	–	–	<7.75	0.04	0.26	–	5.89	<41.44	–
NGC0680	–	–	1.12 ± 0.06	0.60 ± 0.10	0.24	<7.87	0.05	0.11	–	10.40	<41.83	<0.97
NGC0770	–	–	<0.17	–	–	<7.89	–	–	–	1.38	<41.19	–
NGC0821	–	–	<0.15	<0.50	<0.09	<7.52	0.04	0.50	–	30.67	<41.76	–
NGC0936	–	3.67 ± 0.37	–	–	–	<7.47	0.04	0.10	–	59.37	<42.10	<0.24
NGC1023[c]	–	–	0.56 ± 0.11	–	–	<6.79	0.03	0.08	–	110.04	<41.77	<1.21
NGC1121	–	<0.70	–	–	–	<7.81	–	–	–	1.54	<41.24	–
NGC1222	61.7 ± 1.9	–	55.75 ± 3.84	–	–	9.07	13.06	15.41	2.48	1438.67	43.41	2.52
NGC1248	–	–	–	–	–	<7.68	–	–	–	6.32	<41.32	–
NGC1266	115.6 ± 3.5	113.18 ± 11.32	106.60 ± 4.52	–	–	9.28	13.13	16.89	2.15	701.39	43.01	1.42
NGC1289	–	<0.74	–	–	–	<7.89	0.22	1.27	–	5.41	<41.55	–
NGC1665	–	–	–	–	–	<7.95	–	–	–	2.81	<41.61	–
NGC2481	–	<0.66	–	–	–	<7.79	–	–	–	12.25	<41.51	–
NGC2549	–	<0.69	–	–	–	<7.06	0.26	0.37	>2.70	31.94	<41.13	–
NGC2577	–	<1.16	–	–	–	<7.71	0.16	1.25	>2.68	13.14	<41.53	–
NGC2592	–	<0.68	–	–	–	<7.54	0.04	0.38	–	6.93	<41.31	–
NGC2594	–	<0.73	–	–	–	<7.83	–	–	–	2.73	<41.11	–
NGC2679	–	<0.70	–	–	–	<7.87	–	–	–	9.94	<41.29	–
NGC2685[c]	–	<0.78	1.10 ± 0.37	–	–	7.29	0.36	1.87	2.91	58.55	41.28	0.76
NGC2695	–	<0.72	–	–	–	<8.01	0.03	0.11	–	6.85	<41.62	–
NGC2698[a]	–	<0.70	–	–	–	<7.50	–	–	–	12.14	<41.49	–
NGC2699	–	<0.73	–	–	–	<7.54	–	–	–	4.73	<41.25	–
NGC2764	28.1 ± 1.2	12.94 ± 1.29	17.96 ± 1.64	–	–	9.19	3.67	7.22	2.45	303.36	42.88	1.70
NGC2768	14.5 ± 0.6	12.26 ± 1.23	13.65 ± 0.58	–	–	7.64	0.39	1.37	1.74	50.77	<42.05	<1.18
NGC2778[a]	–	<0.71	–	<0.60	–	<7.48	0.04	0.51	–	4.84	<41.05	–
NGC2824	8.9 ± 0.5	8.17 ± 0.82	8.09 ± 0.35	–	–	8.65	1.03	1.89	2.25	56.33	42.16	0.55
NGC2852	–	<0.69	0.72 ± 0.05	–	–	<7.68	–	–	–	2.38	<41.03	<0.82
NGC2859	–	<0.71	–	<0.50	–	<7.61	0.31	0.93	>2.91	19.43	<41.81	–
NGC2880[a]	–	<0.70	–	–	–	<7.44	0.10	0.38	>2.49	6.26	<41.35	–
NGC2950	–	<0.77	–	–	–	<7.12	0.16	0.20	>2.43	37.84	<41.33	–
NGC2962[a]	–	<0.75	–	–	–	<7.85	0.22	0.79	>2.78	19.43	<41.77	–
NGC2974	10.4 ± 0.5	8.06 ± 0.81	–	–	–	<7.65	0.42	1.90	2.09	101.57	41.75	2.34
NGC3032[c]	7.2 ± 0.5	6.55 ± 0.66	5.42 ± 0.32	3.70 ± 0.70	1.75	8.41	1.94	4.70	2.79	138.66	42.00	0.52
NGC3073	–	<1.01	<0.26	<0.50	<0.09	7.52	0.21	0.19	–	9.25	41.12	>0.48
NGC3098	–	<0.70	–	–	–	<7.47	0.11	0.46	–	8.50	<41.25	–
NGC3156[b]	–	<0.77	<0.16	<0.50	<0.09	7.67	0.18	0.61	>3.35	12.76	<41.02	–
NGC3182[c]	2.3 ± 0.5	<0.70	1.41 ± 0.15	–	–	8.33	0.38	1.26	2.70	31.94	41.69	1.10
NGC3193[c]	–	<0.70	0.48 ± 0.08	<0.50	<0.09	<7.91	0.03	0.36	–	14.87	<42.01	<1.41
NGC3226	–	4.42 ± 0.44	–	3.60 ± 0.20	−0.17	<7.41	0.60	–	–	34.51	41.26	1.45
NGC3230	–	<0.70	–	–	–	<8.00	–	–	–	9.20	<41.83	–
NGC3245[c]	6.7 ± 0.5	6.12 ± 0.61	7.05 ± 0.31	3.30 ± 0.20	1.65	7.27	2.03	3.97	2.62	186.88	42.03	1.37
NGC3248	–	<0.70	–	<0.50	–	<7.55	0.03	0.04	–	0.22	<41.13	–
NGC3301	4.2 ± 0.4	1.87 ± 0.19	–	–	–	<7.46	0.48	0.92	2.59	39.66	41.34	1.57
NGC3377[a]	–	<0.67	–	<0.50	–	<6.96	0.14	0.35	>2.56	43.45	<41.27	–
NGC3379[a]	2.4 ± 0.5	<0.68	–	0.70 ± 0.10	>0.02	<6.72	0.04	0.11	–	97.27	<41.68	–
NGC3384	–	<0.67	–	<0.50	–	<7.11	0.04	0.45	–	55.61	<41.57	–
NGC3400	–	<0.71	–	–	–	<7.63	–	–	–	4.20	<40.89	–
NGC3412	–	<0.69	–	<0.50	–	<6.96	–	–	–	20.60	<41.18	–

Table A5 – *continued*

Galaxy	$S_{\rm NVSS}$ (mJy)	$S_{\rm FIRST}$ (mJy)	$S_{\rm VLA}$ (mJy)	$S_{\rm Wrobel}$ (mJy)	$\alpha_{1.4\,\rm GHz}^{5\,\rm GHz}$	$\log(M_{\rm H2})$ ($M_\odot$)	$S_{60\,\mu\rm m}$ (Jy)	$S_{100\,\mu\rm m}$ (Jy)	q	$S_{22\,\mu\rm m}$ (mJy)	$\log(L_{22\,\mu\rm m})$ (erg s^{-1})	$q_{22\,\mu\rm m}$
(1)	(2)	(3)	(4)	(5)	(6)	(7)	(8)	(9)	(10)	(11)	(12)	(13)
NGC3414	4.4 ± 0.4	4.00 ± 0.40	–	5.00 ± 0.20	0.19	<7.19	0.25	0.56	2.01	35.58	<41.75	<1.90
NGC3457	–	<0.73	–	<0.50	–	<7.35	0.04	0.31	–	5.62	<40.92	–
NGC3458	–	<0.67	–	<0.50	–	<7.73	0.03	0.09	–	5.44	<41.41	–
NGC3489[c]	–	<0.67	0.84 ± 0.10	<0.50	<0.09	7.20	–	–	–	112.92	41.21	1.54
NGC3499	–	<0.79	–	–	–	<7.62	–	–	–	6.90	<40.91	–
NGC3522	–	<0.73	–	–	–	<7.28	–	–	–	2.38	<40.83	–
NGC3530	–	<0.75	–	–	–	<7.78	–	–	–	2.32	<40.96	–
NGC3595	–	<0.69	–	<0.50	–	<7.84	0.05	0.17	–	2.75	<41.47	–
NGC3599	–	<0.72	<0.20	<0.50	<0.09	7.36	–	–	–	32.51	41.21	>0.94
NGC3605	–	<0.72	<0.14	<0.50	<0.09	<7.48	–	–	–	4.22	<40.89	–
NGC3607	6.9 ± 0.4	5.62 ± 0.56	5.47 ± 0.24	2.60 ± 0.10	1.46	8.42	–	–	–	115.87	<42.06	<0.89
NGC3608	–	<0.68	0.36 ± 0.05	<0.50	<0.09	<7.58	–	–	–	18.01	<41.62	<1.40
NGC3610	–	<0.72	–	<0.50	–	<7.40	0.03	0.28	–	27.16	<41.64	–
NGC3613	–	<0.76	–	<0.50	–	<7.66	0.03	0.09	–	10.74	<41.87	–
NGC3619	5.6 ± 0.5	2.74 ± 0.27	2.62 ± 0.27	0.90 ± 0.10	0.58	8.28	0.38	1.83	2.53	45.62	41.58	1.33
NGC3626	10.1 ± 0.9	7.27 ± 0.73	6.44 ± 1.02	1.40 ± 0.10	0.94	8.21	–	–	–	165.79	41.96	0.95
NGC3630	–	<0.77	–	<0.50	–	<7.60	0.06	0.11	–	7.78	<41.43	–
NGC3640	–	<0.78	–	<0.50	–	<7.59	0.04	0.07	–	50.81	<42.00	–
NGC3641	–	<0.77	–	<0.50	–	<7.66	0.04	0.15	–	0.56	<40.90	–
NGC3648[d]	–	<0.66	0.54 ± 0.06	–	–	<7.77	0.03	0.11	–	5.92	<41.39	<2.12
NGC3658	–	<0.67	–	<0.50	–	<7.82	0.16	0.92	>2.83	14.71	<41.54	–
NGC3665	112.2 ± 3.7	8.89 ± 0.89	98.38 ± 8.75	–	–	8.91	1.91	7.53	1.63	138.66	42.29	1.28
NGC3674	–	<0.71	–	<0.50	–	<7.78	0.04	0.14	–	1.32	<41.45	–
NGC3694	4.5 ± 0.5	3.65 ± 0.36	–	0.80 ± 0.10	−1.26	<7.91	0.57	1.04	2.36	31.42	41.77	1.45
NGC3757	–	<0.71	–	<0.50	–	<7.48	0.11	0.13	>2.29	2.08	<41.02	–
NGC3796	–	<0.77	–	–	–	<7.51	–	–	–	7.05	<40.90	–
NGC3838	–	<0.72	–	–	–	<7.53	0.03	0.11	–	4.23	<41.17	–
NGC3941[a]	–	<0.72	–	<0.50	–	<6.89	–	–	–	52.67	<41.39	–
NGC3945	–	1.09 ± 0.11	2.12 ± 0.32	1.00 ± 0.10	0.66	<7.50	0.26	1.36	2.51	42.11	<41.89	<1.64
NGC3998	98.4 ± 3.0	98.51 ± 9.85	–	–	–	<7.06	0.55	1.15	0.94	175.53	41.62	2.31
NGC4026	–	<0.68	–	1.40 ± 0.10	>0.60	<6.99	0.10	0.56	>2.61	31.13	<41.37	–
NGC4036	11.6 ± 0.5	9.42 ± 0.94	10.76 ± 0.46	2.90 ± 0.20	1.55	8.13	0.56	1.63	1.96	58.72	<41.92	<1.22
NGC4078	–	0.94 ± 0.09	–	0.60 ± 0.10	−0.37	<7.98	0.07	0.52	2.40	4.72	<41.36	<1.09
NGC4111	9.4 ± 0.5	9.42 ± 0.94	7.69 ± 0.35	2.30 ± 0.10	1.36	7.22	–	–	–	97.09	41.34	1.44
NGC4119[b]	–	<0.75	<0.17	–	–	7.88	0.43	1.75	>3.74	54.20	41.25	>0.91
NGC4143	9.9 ± 0.9	5.04 ± 0.50	–	6.70 ± 0.30	0.24	<7.20	–	–	–	42.93	<41.40	<0.48
NGC4150[bc]	–	<0.69	0.82 ± 0.06	<0.50	<0.09	7.82	1.22	2.67	3.37	73.92	41.28	1.03
NGC4168	5.6 ± 0.4	5.66 ± 0.57	–	4.50 ± 0.20	−0.19	<7.74	0.04	0.66	–	13.66	<41.77	<1.48
NGC4179	–	<0.77	–	<0.50	–	<7.28	0.03	0.07	–	9.08	<41.43	–
NGC4191	–	<0.69	–	<0.50	–	<7.94	0.12	0.72	>2.70	6.35	<41.40	–
NGC4203	6.1 ± 0.5	7.72 ± 0.77	8.87 ± 0.39	12.50 ± 0.40	2.76	7.39	0.59	2.16	2.12	80.38	<41.54	<0.15
NGC4215	–	<0.73	–	<0.50	–	<7.83	0.03	0.10	–	8.55	<41.53	–
NGC4233	–	1.42 ± 0.14	–	1.90 ± 0.10	0.24	<7.89	0.19	0.48	2.36	14.91	<41.71	<0.12
NGC4249	–	<0.66	–	–	–	<7.97	–	–	–	0.50	<40.95	–
NGC4251	–	<0.75	–	<0.50	–	<7.11	0.12	0.09	–	33.91	<41.63	–
NGC4255	–	<0.78	–	<0.50	–	<7.78	0.04	0.13	–	2.29	<41.36	–
NGC4259	–	<0.69	–	–	–	<7.97	–	–	–	3.26	<41.04	–
NGC4261	–	181.82 ± 18.18	–	–	–	<7.68	0.08	0.15	-0.18	68.42	<42.23	<0.05
NGC4262	–	<0.72	–	<0.50	–	<7.07	0.18	0.39	>2.60	12.61	<41.20	–
NGC4264	–	<1.82	–	<10.00	–	<7.94	0.04	0.12	–	3.84	<41.36	–
NGC4267	–	<0.69	–	<0.50	–	<7.16	0.18	1.16	>2.90	18.81	<41.43	–
NGC4268	–	<0.73	–	–	–	<7.83	0.40	0.80	>2.92	5.42	<41.38	–
NGC4270	–	<0.77	–	<0.50	–	<7.79	0.04	0.09	–	5.24	<41.64	–
NGC4278	385.0 ± 11.6	402.00 ± 40.20	–	–	–	<7.45	0.58	1.86	0.45	66.74	<41.68	<1.88
NGC4281[b]	–	<0.75	–	<0.50	–	<7.88	0.61	2.00	>3.20	58.77	<41.77	–
NGC4283	–	<0.67	–	<2.00	–	7.10	0.03	0.08	–	10.86	<40.88	–
NGC4324[b]	–	<0.73	<0.20	<0.50	<0.09	7.69	0.41	1.99	>3.72	47.77	41.17	>2.30
NGC4339	–	<0.70	–	<0.50	–	<7.15	0.03	0.22	–	11.63	<41.16	–
NGC4340	–	<0.72	–	<0.50	–	<7.33	0.09	0.37	>2.45	12.73	<41.37	–
NGC4342	–	<0.72	–	<0.50	–	<7.24	0.07	0.18	–	4.11	<40.99	–
NGC4346	–	<0.71	–	<1.00	–	<7.12	–	–	–	22.22	<41.18	–
NGC4350	–	<0.68	–	<0.50	–	<7.18	0.36	1.09	>3.00	35.81	<41.41	–

Table A5 – *continued*

Galaxy	$S_{\rm NVSS}$ (mJy)	$S_{\rm FIRST}$ (mJy)	$S_{\rm VLA}$ (mJy)	$S_{\rm Wrobel}$ (mJy)	$\alpha_{1.4\,\rm GHz}^{5\,\rm GHz}$	$\log(M_{\rm H2})$ ($M_\odot$)	$S_{60\,\mu\rm m}$ (Jy)	$S_{100\,\mu\rm m}$ (Jy)	q	$S_{22\,\mu\rm m}$ (mJy)	$\log(L_{22\,\mu\rm m})$ (erg s^{-1})	$q_{22\,\mu\rm m}$
(1)	(2)	(3)	(4)	(5)	(6)	(7)	(8)	(9)	(10)	(11)	(12)	(13)
NGC4365	–	<0.72	–	<0.50	–	<7.62	0.04	0.65	–	62.00	<42.25	–
NGC4371	–	<0.74	–	<0.50	–	<7.29	0.05	0.16	–	30.36	<41.54	–
NGC4374	–	1446.87 ± 144.69	–	–	–	<7.23	0.50	1.16	-0.24	114.49	<42.21	<0.09
NGC4377	–	<0.74	–	<0.50	–	<7.26	0.36	1.10	>2.96	35.54	41.11	>0.41
NGC4379	–	<0.70	–	<0.50	–	<7.19	0.05	0.13	–	6.10	<41.06	–
NGC4382	–	<0.68	–	<0.50	–	<7.39	0.15	0.08	–	131.33	<42.21	–
NGC4387	–	<4.17	–	<0.50	–	<7.39	0.05	0.18	–	7.35	<41.01	–
NGC4406	–	<3.56	–	<0.50	–	<7.40	0.11	0.33	>1.76	84.72	<42.18	–
NGC4417	–	<0.70	–	<0.50	–	<7.22	0.04	0.12	–	23.14	<41.31	–
NGC4425	–	<0.83	–	<0.50	–	<7.20	0.06	0.17	–	4.87	<41.00	–
NGC4429[b]	–	<0.79	1.12 ± 0.11	<0.50	<0.09	8.05	1.56	5.15	3.43	148.58	<41.89	<0.93
NGC4434	–	<0.74	–	<0.50	–	<7.60	0.04	0.16	–	4.99	<41.18	–
NGC4435[b]	–	2.16 ± 0.22	–	1.20 ± 0.10	-0.49	7.87	1.99	4.68	3.18	112.61	41.50	0.72
NGC4442	–	<0.70	–	<0.50	–	<7.12	0.13	0.28	>2.47	47.42	<41.61	–
NGC4452	–	<1.12	–	–	–	<7.19	0.03	0.10	–	2.89	<40.91	–
NGC4458	–	<0.86	–	<0.50	–	<7.31	0.03	0.14	–	3.28	<40.87	–
NGC4459[b]	–	1.83 ± 0.18	1.39 ± 0.08	0.80 ± 0.10	0.48	8.24	1.87	4.82	3.37	139.82	41.58	1.30
NGC4461	–	<1.04	–	<0.50	–	<7.20	0.02	0.09	–	15.67	<41.39	–
NGC4472	219.9 ± 7.8	123.70 ± 12.37	–	–	–	<7.25	0.07	0.11	–	192.29	<42.47	<1.40
NGC4473	–	<0.77	–	<2.00	–	<7.07	0.06	0.11	–	44.09	<41.67	–
NGC4474	–	<0.71	–	<0.50	–	<7.16	0.05	0.09	–	11.92	<41.07	–
NGC4476	–	<16.06	–	<10.00	–	8.05	0.66	1.84	>1.87	32.48	41.13	>0.99
NGC4477[b]	–	<0.72	–	<0.50	–	7.54	0.57	1.41	>3.13	51.14	<41.66	–
NGC4478	–	<18.39	–	<5.00	–	<7.28	0.04	0.08	–	17.09	<41.28	–
NGC4483	–	<0.74	–	–	–	<7.20	0.04	0.47	–	5.05	<40.90	–
NGC4486	138487.0 ± 4858.7	122193.84 ± 12219.38	–	–	–	<7.17	0.39	0.41	-2.41	256.31	<42.31	<0.54
NGC4486A	–	<24.85	–	–	–	<0.00	0.03	0.26	–	6.01	<40.89	–
NGC4489	–	<0.74	–	<0.50	–	<7.15	0.04	0.13	–	4.10	<40.80	–
NGC4494[a]	–	<0.67	–	<0.50	–	<7.25	0.19	0.17	–	50.81	<41.81	–
NGC4503	–	<0.80	–	<0.50	–	<7.22	0.04	0.19	–	21.07	<41.45	–
NGC4521	–	<0.76	–	–	–	<7.97	0.16	0.17	–	16.55	<41.73	–
NGC4526	12.0 ± 0.5	12.00 ± 1.20	9.78 ± 0.73	3.10 ± 0.20	1.60	8.59	5.56	17.10	3.00	364.39	42.08	0.25
NGC4528	–	<0.79	–	<0.50	–	<7.15	0.04	0.15	–	7.74	<40.98	–
NGC4546	10.5 ± 0.5	10.90 ± 1.09	–	–	–	<6.97	0.26	0.89	1.68	61.37	<41.48	<1.02
NGC4550	–	<0.78	<0.25	<1.00	<0.66	<7.24	0.14	0.25	>2.91	11.63	<41.07	–
NGC4551	–	<0.77	<0.22	<0.50	<0.09	<7.24	0.04	0.16	–	6.91	<41.03	–
NGC4552	100.1 ± 3.0	112.78 ± 11.28	–	–	–	<7.28	0.16	0.53	0.45	74.88	<41.88	<1.50
NGC4564	–	<0.75	<0.15	<0.50	<0.09	<7.25	0.06	0.19	–	19.61	<41.39	–
NGC4570	–	<0.73	–	<0.50	–	<7.47	0.05	0.11	–	32.09	<41.55	–
NGC4578	–	<0.74	–	<0.50	–	<7.20	0.03	0.11	–	20.03	<41.23	–
NGC4596[b]	–	<0.72	<0.14	<0.50	<0.09	7.31	0.40	0.75	>3.63	41.61	<41.61	–
NGC4608	–	<0.74	–	<1.00	–	<7.30	0.03	0.24	–	12.12	<41.34	–
NGC4612	–	<0.72	–	<0.50	–	<7.20	0.04	0.09	–	14.16	<41.18	–
NGC4621[a]	–	<0.70	–	<0.50	–	<7.13	0.05	0.09	–	55.41	<41.82	–
NGC4623	–	<0.73	–	<0.50	–	<7.21	0.02	0.12	–	14.11	<40.86	–
NGC4624	–	<0.68	–	–	–	<7.30	0.03	0.05	–	38.16	<41.63	–
NGC4636	77.8 ± 2.8	56.91 ± 5.69	–	–	–	<6.87	0.14	0.17	–	97.99	<41.91	<0.22
NGC4638	–	<0.73	–	<0.50	–	<7.30	–	–	–	12.78	<41.37	–
NGC4643[b]	–	<0.70	0.41 ± 0.07	–	–	7.27	0.62	2.06	3.48	87.17	<41.64	<0.71
NGC4649	29.1 ± 1.3	16.54 ± 1.65	–	–	–	<7.44	0.78	1.09	1.80	465.97	42.14	1.80
NGC4660	–	<0.72	–	<0.50	–	<7.19	0.05	0.10	–	22.49	<41.24	–
NGC4684	7.1 ± 0.5	5.57 ± 0.56	5.31 ± 0.25	–	–	7.21	1.27	2.15	2.44	247.27	41.81	0.70
NGC4690	–	<0.70	–	–	–	<8.01	0.06	0.15	–	3.49	<41.35	–
NGC4694[bc]	3.5 ± 0.5	<0.70	1.44 ± 0.08	<0.50	<0.09	8.01	1.24	3.02	3.16	116.51	41.68	1.03
NGC4697[ba]	–	<0.79	<0.19	–	–	<6.86	0.46	1.24	>3.63	92.89	<41.73	–
NGC4710	18.7 ± 1.0	14.80 ± 1.48	13.53 ± 0.83	8.80 ± 1.10	2.47	8.72	5.73	14.79	2.81	434.47	42.25	0.93
NGC4733	–	<0.69	–	<0.50	–	<7.28	0.04	0.11	–	7.72	<40.88	–
NGC4753[bc]	–	<0.72	1.14 ± 0.12	–	–	8.55	2.57	9.01	3.65	239.86	42.15	1.95
NGC4754	–	<0.76	–	<0.50	–	<7.18	0.04	0.12	–	39.23	<41.62	–
NGC4762	–	<0.71	–	<0.50	–	<7.48	0.05	0.08	–	31.45	<41.95	–
NGC4803	–	<0.76	–	–	–	<7.98	–	–	–	0.29	<41.07	–
NGC5103	–	<0.81	–	–	–	<7.58	–	–	–	4.36	<41.11	–

Table A5 *– continued*

Galaxy	$S_{\rm NVSS}$ (mJy)	$S_{\rm FIRST}$ (mJy)	$S_{\rm VLA}$ (mJy)	$S_{\rm Wrobel}$ (mJy)	$\alpha_{1.4\,\rm GHz}^{5\,\rm GHz}$	$\log(M_{\rm H2})$ ($M_\odot$)	$S_{60\,\mu\rm m}$ (Jy)	$S_{100\,\mu\rm m}$ (Jy)	q	$S_{22\,\mu\rm m}$ (mJy)	$\log(L_{22\,\mu\rm m})$ (erg s^{-1})	$q_{22\,\mu\rm m}$
(1)	(2)	(3)	(4)	(5)	(6)	(7)	(8)	(9)	(10)	(11)	(12)	(13)
NGC5173	–	1.02 ± 0.10	1.37 ± 0.08	–	–	8.28	0.35	0.53	2.52	18.06	41.55	0.38
NGC5198	3.6 ± 0.4	2.80 ± 0.28	–	1.50 ± 0.10	-0.52	<7.89	0.04	0.08	–	8.37	<41.80	<1.26
NGC5273	3.5 ± 0.4	2.90 ± 0.29	2.80 ± 0.26	1.20 ± 0.10	0.81	7.31	0.90	1.56	2.64	88.71	41.51	0.93
NGC5308	–	<0.78	–	<0.50	–	<7.88	0.04	0.09	–	12.37	<41.81	–
NGC5322	78.4 ± 2.8	40.78 ± 4.08	–	–	–	<7.76	0.42	1.00	1.23	54.30	<42.27	<1.38
NGC5342	–	<0.76	–	–	–	<7.79	–	–	–	1.76	<41.21	–
NGC5353	40.5 ± 1.3	38.30 ± 3.83	–	–	–	<8.12	0.32	1.45	1.30	42.97	<42.21	<1.40
NGC5355	–	<0.71	–	<0.50	–	<7.94	0.04	0.07	–	5.29	<41.12	–
NGC5358	–	<0.68	–	–	–	<7.92	–	–	–	1.00	<40.97	–
NGC5379	–	<0.77	0.55 ± 0.06	–	–	8.33	0.28	1.30	–	42.22	41.76	1.02
NGC5422	–	<0.67	–	<0.50	–	<7.78	0.07	0.37	>2.44	10.48	<41.64	–
NGC5473	–	<0.69	–	<0.50	–	<7.85	0.09	0.36	>2.46	16.87	<41.86	–
NGC5475	7.9 ± 0.5	7.61 ± 0.76	–	–	–	<7.72	–	–	–	9.41	<41.31	<1.56
NGC5481	–	<0.70	–	<0.50	–	<7.60	0.03	0.20	–	2.42	<41.23	–
NGC5485[a]	–	<0.76	–	<1.00	–	<7.60	0.15	0.96	>2.78	22.18	<41.61	–
NGC5493	–	<0.76	–	–	–	<7.98	0.04	0.11	–	14.53	<41.96	–
NGC5500	–	<0.72	–	–	–	<7.82	–	–	–	2.04	<40.93	–
NGC5507	–	<0.66	–	–	–	<7.70	0.38	0.66	–	6.64	<41.44	–
NGC5557	–	<0.70	–	–	–	<7.92	0.04	0.09	–	17.77	<42.11	–
NGC5574	–	<0.75	–	<0.50	–	<7.51	0.04	0.50	–	8.91	<41.08	–
NGC5576	–	<0.75	–	<0.50	–	<7.60	0.09	0.21	>2.30	20.04	<41.82	–
NGC5582	–	<0.69	–	<0.50	–	<7.67	0.04	0.10	–	5.31	<41.47	–
NGC5611	–	<0.52	–	<0.50	–	<7.57	0.04	0.11	–	3.09	<41.04	–
NGC5631[a]	–	<0.72	–	<0.50	–	<7.68	0.22	1.04	>2.88	22.99	<41.64	–
NGC5638	–	<0.77	–	<0.50	–	<7.60	0.03	0.45	–	15.95	<41.68	–
NGC5687	–	<0.73	–	<1.00	–	<7.64	0.10	0.50	>2.54	8.28	<41.45	–
NGC5770	–	<0.76	–	<0.50	–	<7.34	0.03	0.14	–	6.17	<41.02	–
NGC5813	14.8 ± 1.0	5.94 ± 0.59	–	2.10 ± 0.10	−0.86	<7.69	0.02	0.10	–	31.33	<42.20	<1.51
NGC5831	–	<0.74	–	<0.50	–	<7.85	–	–	–	13.94	<41.64	–
NGC5838	2.6 ± 0.4	2.42 ± 0.24	–	2.00 ± 0.10	−0.16	<7.56	0.73	1.67	2.69	60.64	<41.81	<1.42
NGC5839	–	<0.72	–	<0.50	–	<7.38	0.04	0.09	–	6.20	<41.17	–
NGC5845	–	<0.68	–	<0.50	–	<7.50	0.17	0.23	>2.52	9.14	<41.33	–
NGC5846	21.0 ± 1.3	13.69 ± 1.37	–	5.30 ± 0.30	−0.79	<7.78	0.04	0.13	–	46.94	<42.17	<1.80
NGC5854	–	<0.76	–	<0.50	–	<7.60	0.03	0.19	–	14.70	<41.48	–
NGC5864	–	<0.75	–	<0.50	–	<7.74	0.03	0.38	–	11.90	<41.61	–
NGC5866	21.8 ± 1.1	16.86 ± 1.69	20.83 ± 3.81	7.40 ± 0.30	2.33	8.47	5.07	18.68	2.69	229.07	41.78	−0.42
NGC5869	–	<0.76	–	–	–	<7.63	–	–	–	10.31	<41.47	–
NGC6010	–	<0.72	–	–	–	<7.78	–	–	–	10.63	<41.57	–
NGC6014	4.1 ± 0.4	3.74 ± 0.37	4.13 ± 0.35	1.20 ± 0.10	0.81	8.77	1.18	1.86	2.60	130.25	42.42	−0.78
NGC6017	–	<0.70	–	<0.50	–	<7.73	0.33	0.43	>2.79	17.38	41.25	>2.04
NGC6149	–	<0.73	–	–	–	<7.90	–	–	–	5.83	<41.20	–
NGC6278[a]	–	<0.72	–	1.20 ± 0.10	>0.42	<7.98	0.02	0.32	–	11.92	<41.84	–
NGC6547[c]	–	–	2.48 ± 0.12	–	–	<8.00	–	–	–	4.08	<41.60	<−1.10
NGC6548	–	–	–	–	–	<7.58	0.04	0.12	–	17.41	<41.44	–
NGC6703	–	–	–	–	–	<7.62	0.07	0.20	–	19.80	<41.70	–
NGC6798	–	–	0.23 ± 0.05	–	–	7.83	–	–	–	16.07	<41.57	<2.12
NGC7280	–	–	–	<0.50	–	<7.49	0.20	0.42	–	14.03	<41.29	–
NGC7332	–	–	–	–	–	<7.41	0.21	0.41	–	30.25	<41.66	–
NGC7454	–	–	<0.14	<0.50	<0.09	<7.39	0.19	0.24	–	2.29	<41.36	–
NGC7457[b]	–	–	<0.14	–	–	<6.96	0.11	0.45	>3.23	16.02	<41.11	–
NGC7465	19.1 ± 1.1	–	15.80 ± 0.87	3.70 ± 0.20	1.75	8.79	5.47	8.14	2.67	288.91	42.60	1.72
NGC7693	–	<0.67	–	–	–	<7.86	–	–	–	0.16	<40.79	–
NGC7710	–	<1.85	–	–	–	<7.80	–	–	–	1.61	<40.96	–
PGC016060[b]	–	–	<0.30	–	–	8.26	0.32	1.18	>3.35	22.38	41.66	>1.15
PGC028887	–	<0.70	–	–	–	<8.03	–	–	–	0.46	<41.07	–
PGC029321	8.7 ± 0.5	8.30 ± 0.83	9.02 ± 0.39	–	–	8.53	1.14	0.90	2.13	228.22	42.79	2.00
PGC035754	–	<0.78	–	–	–	<7.90	–	–	–	0.26	<40.92	–
PGC042549	–	<1.42	–	–	–	<8.07	–	–	–	8.90	41.23	>−0.56
PGC044433	–	<0.67	–	–	–	<7.98	–	–	–	0.18	<41.06	–
PGC050395	–	<0.68	–	–	–	<7.87	–	–	–	1.52	<40.93	–
PGC051753	–	<0.69	–	–	–	<7.92	–	–	–	0.55	<40.93	–
PGC054452	–	<0.73	–	–	–	<7.73	–	–	–	1.70	<40.80	–

Table A5 – *continued*

Galaxy	$S_{\rm NVSS}$ (mJy)	$S_{\rm FIRST}$ (mJy)	$S_{\rm VLA}$ (mJy)	$S_{\rm Wrobel}$ (mJy)	$\alpha_{1.4\,\rm GHz}^{5\,\rm GHz}$	log ($M_{\rm H2}$) ($M_\odot$)	$S_{60\,\mu\rm m}$ (Jy)	$S_{100\,\mu\rm m}$ (Jy)	q	$S_{22\,\mu\rm m}$ (mJy)	log($L_{22\,\mu\rm m}$) (erg s^{-1})	$q_{22\,\mu\rm m}$
(1)	(2)	(3)	(4)	(5)	(6)	(7)	(8)	(9)	(10)	(11)	(12)	(13)
PGC056772	3.0 ± 0.4	3.30 ± 0.33	3.14 ± 0.14	–	–	8.19	0.92	0.99	2.50	90.36	42.35	0.19
PGC058114	11.9 ± 0.9	–	8.83 ± 0.38	–	–	8.60	3.19	4.11	2.62	359.39	42.52	−2.68
PGC061468	–	–	<0.18	–	–	8.00	–	–	–	11.07	41.32	>0.98
PGC071531	–	–	–	–	–	<7.65	–	–	–	1.90	<40.86	–
PGC170172	–	<0.70	–	–	–	<7.97	–	–	–	1.33	<40.92	–
UGC03960	–	<0.70	–	–	–	<7.81	–	–	–	1.28	<40.92	–
UGC04551	–	<0.71	–	–	–	<7.62	0.03	0.06	–	1.76	<41.33	–
UGC05408	4.0 ± 0.4	2.58 ± 0.26	3.78 ± 0.17	–	–	8.32	1.37	1.84	2.62	140.46	42.68	1.53
UGC06062	–	<0.85	–	–	–	<7.93	–	–	–	5.13	<41.29	–
UGC06176	7.8 ± 0.5	6.04 ± 0.60	6.17 ± 0.27	–	–	8.58	–	–	–	181.28	42.67	0.75
UGC08876	–	<0.70	–	–	–	<7.80	–	–	–	0.53	<41.11	–
UGC09519[bc]	–	<0.65	0.45 ± 0.06	–	–	8.77	0.38	0.94	3.19	26.67	41.47	−0.18

Notes. Column 1: galaxy name. Column 2: 1.4 GHz flux density from the NVSS catalogue. The spatial resolution of these data is $\theta_{\rm FWHM} \approx 45$ arcsec and their typical sensitivity is ≈0.5 mJy beam^{-1}. Column 3: 1.4 GHz flux density from the FIRST survey. The spatial resolution of these data is $\theta_{\rm FWHM} \approx 5$ arcsec and their typical sensitivity is ≈0.15 mJy beam^{-1}. Column 4: 1.4 GHz flux density from this work. Column 5: 5 GHz flux density from Wrobel & Heeschen (1991). Column 6: radio spectral index estimates or limits from 1.4 GHz (Column 4 or Column 3) to 5 GHz (Column 5) at near-matched spatial resolution. A value is only reported if the source is detected in at least one of the two frequencies. Column 7: IRAM single-dish H_2 mass from Young et al. (2011). Column 8: *IRAS* 60 μm flux density. Column 9: *IRAS* 100 μm flux density. Column 10: logarithmic FIR-radio ratio. Column 11: *WISE* 22 μm flux density. Column 12: corrected *WISE* 22 μm luminosity (see equation 1 in Davis et al. 2014). Column 13: logarithmic 22 μm radio ratio.

[a]Source detected at 5 GHz with $\theta_{\rm FWHM} \approx 0.5$ arcsec in Nyland et al. (2016), but not in the 1.4 GHz data used in this work with $\theta_{\rm FWHM} \approx 5$ arcsec.

[b]Candidate FIR-excess source.

[c]Source detected in the 1.4 GHz observations presented in this work with $\theta_{\rm FWHM} \approx 5$ arcsec, but not at 5 GHz with $\theta_{\rm FWHM} \approx 0.5$ arcsec in Nyland et al. (2016).

[d]While NGC3648 is reported as a detection in Wrobel (1991), we believe that measurement is actually associated with a nearby background source at an angular separation of about 25 arcsec from NGC3648.

APPENDIX B: RADIO CONTINUUM MAPS

For each ETG included in our new 1.4 GHz VLA observations, we provide a map of the radio continuum emission with contours in Fig. B1. The rms noise level and relative contours of each detected ETG are listed in Table B1. Optical images with radio continuum contours are shown in Fig. B2 for the 19 well-resolved sources.

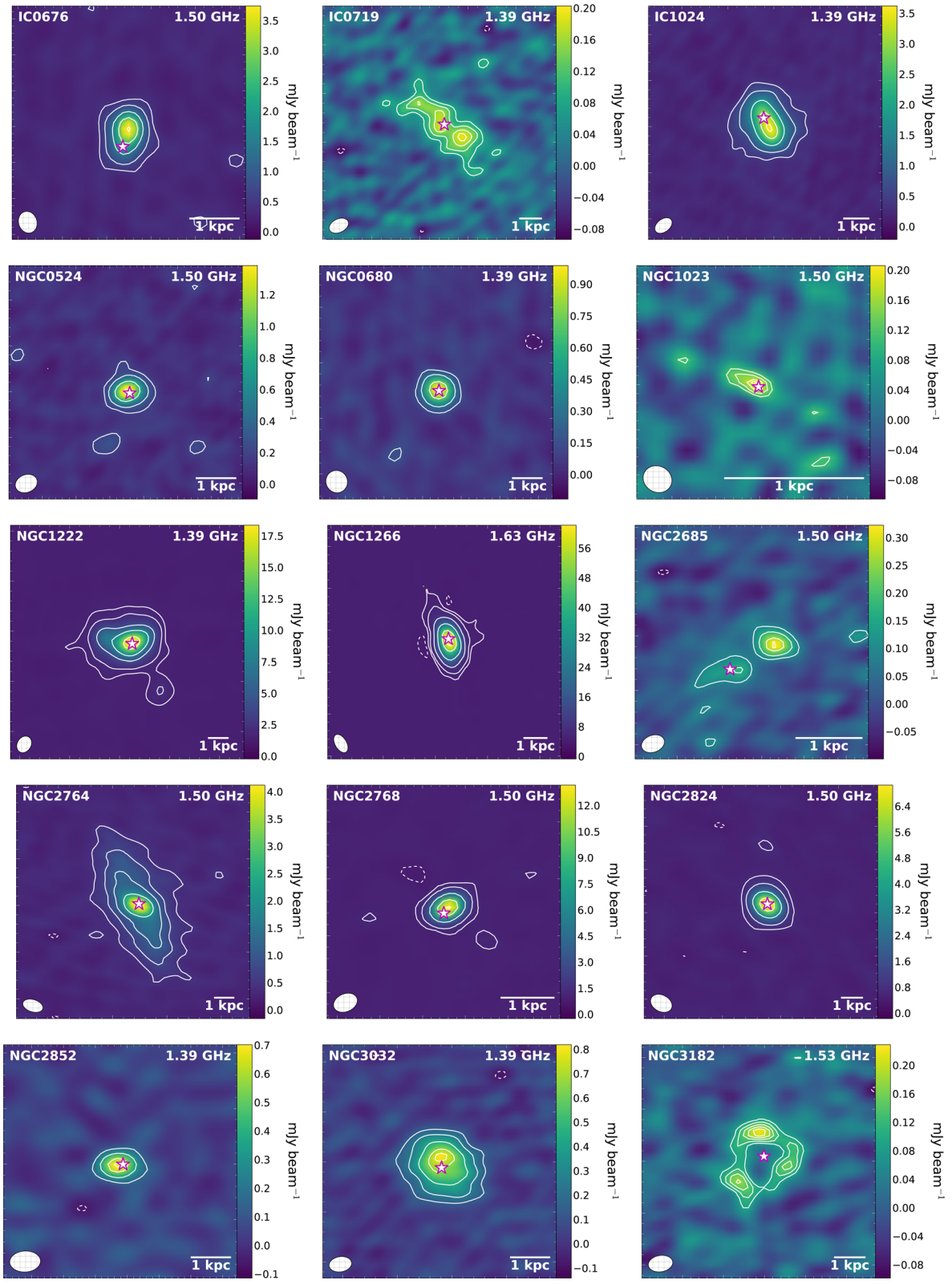

Figure B1. 1.4 GHz continuum images with contours. Negative contours are dashed. The contour levels are spaced as multiples of the rms noise in each image. Relative contour levels and rms noises are listed in Table B1. The synthesized beam is shown as a filled magenta ellipse in the lower left corner of each image. In the upper right corner of each image the central observing frequency is shown. A magenta star denotes the official optical position in the ATLAS^{3D} survey (Cappellari et al. 2011a). A scale bar denoting a size of 1 kpc is shown in the lower left corner of each image. We note that the bright component to the southwest of NGC3648 is most likely associated with a background source about 25″ away.

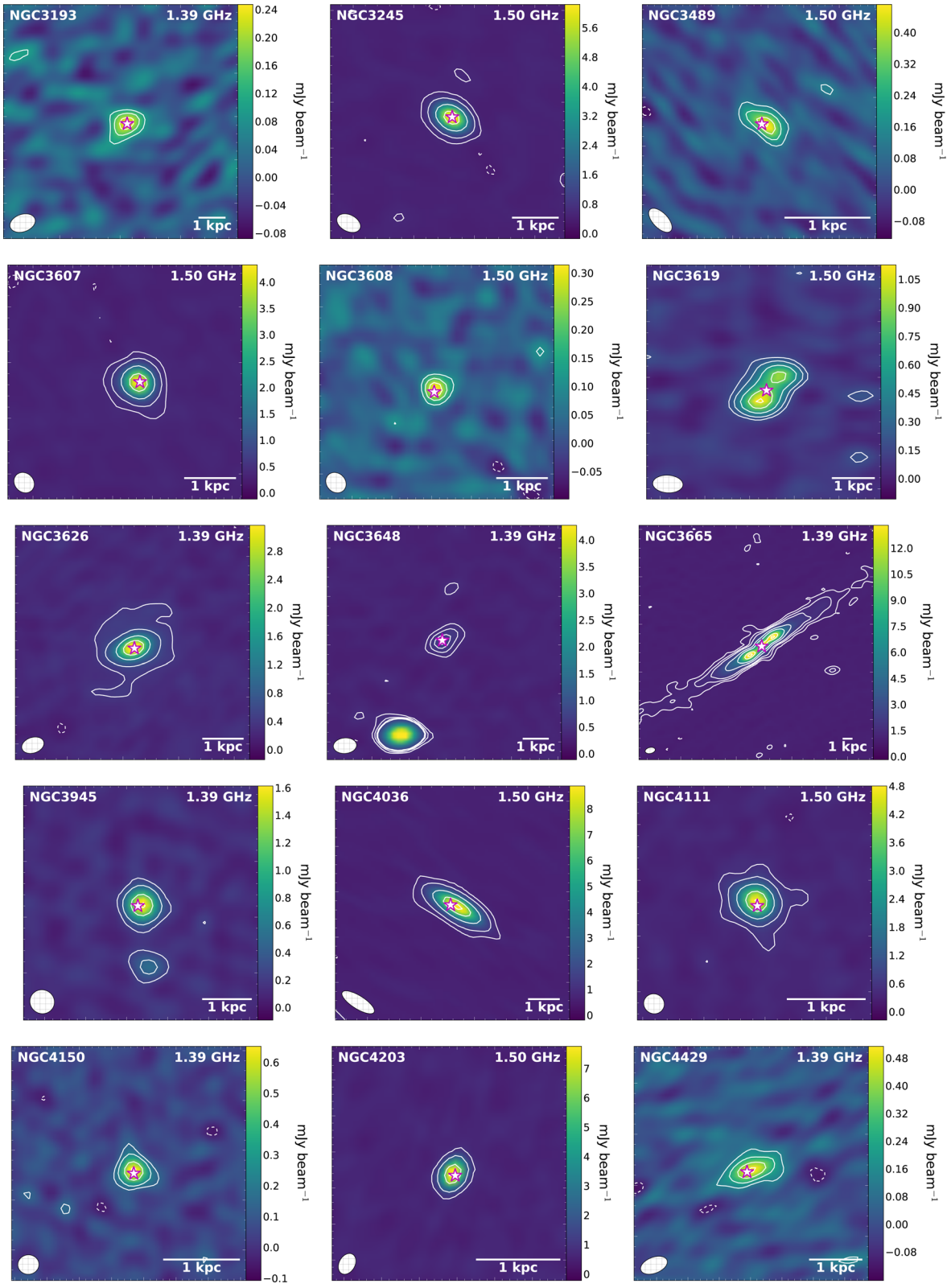

Figure B1 – *continued*

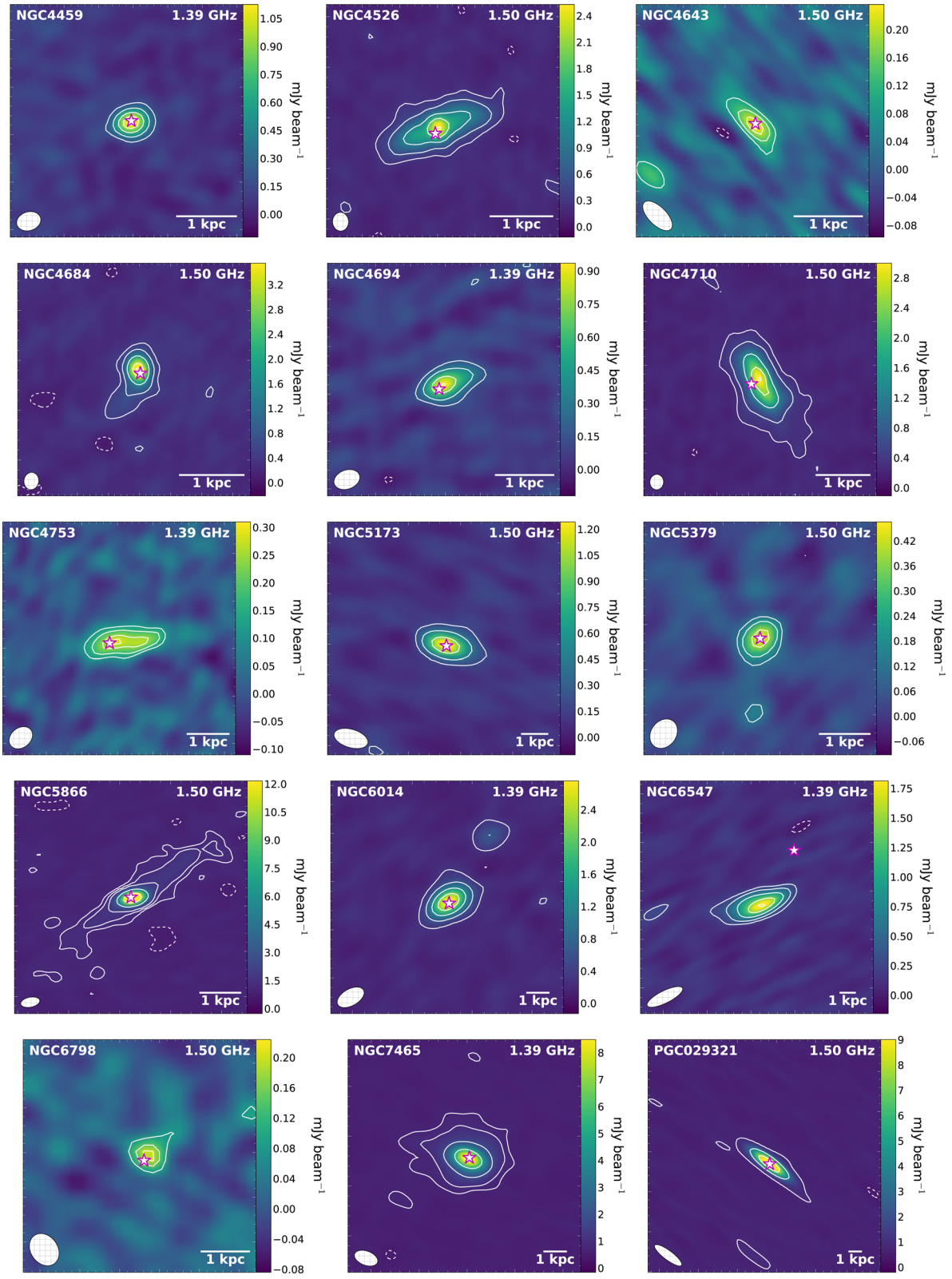

Figure B1 – *continued*

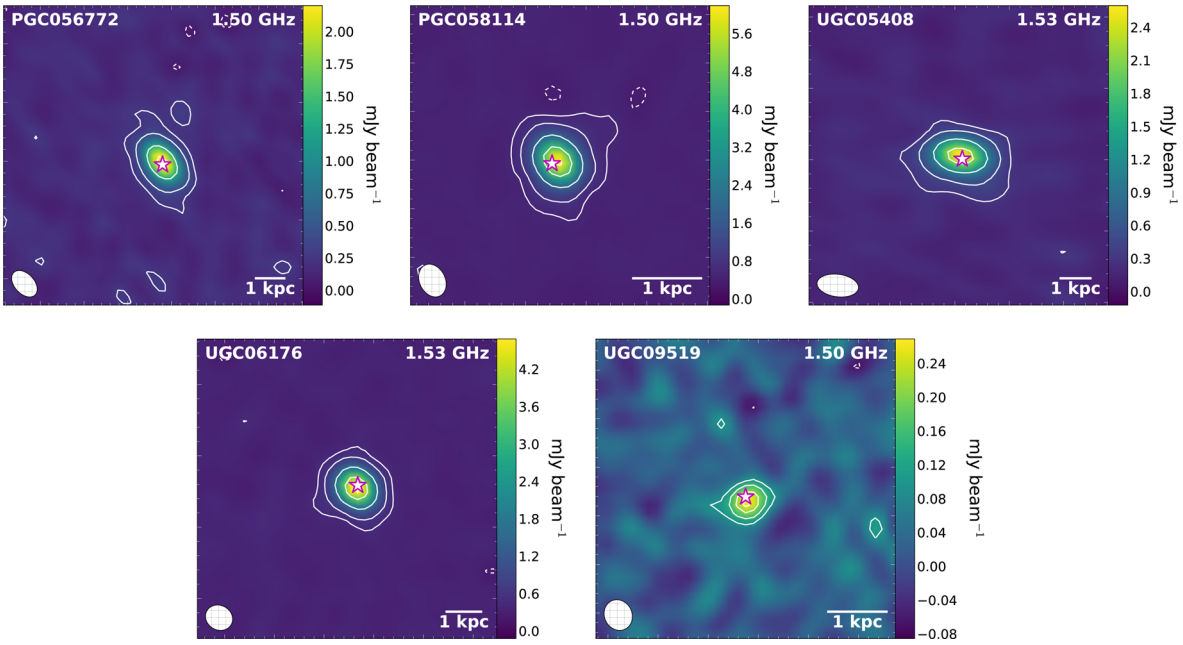

Figure B1 – *continued*

Table B1. Relative contour levels in the 1.4 GHz continuum maps.

Galaxy	rms (μJy beam^{-1})	Relative contours
IC0676	43	[−3, 3, 9, 25, 50, 83]
IC0719	28	[−3, 3, 4.5, 6, 7]
IC1024	67	[−3, 3, 9, 24, 43, 53]
NGC0524	29	[−3, 3, 8, 22, 44]
NGC0680	27	[−3, 3, 9, 24, 35]
NGC1023	36	[−3, 3, 4, 5, 5.5]
NGC1222	70	[−3, 3, 9, 40, 90, 198, 258]
NGC1266	74	[−3, 3, 12, 60, 200, 500, 740]
NGC2685	29	[−3, 3, 5.5, 9, 11]
NGC2764	40	[−3, 3, 9, 18, 40, 100]
NGC2768	42	[−3, 3, 15, 72, 192, 302]
NGC2824	42	[−3, 3, 12, 50, 120, 164]
NGC2852	35	[−3, 3, 8, 15, 19]
NGC3032	39	[−3, 3, 6, 11, 17, 20]
NGC3182	30	[−3, 3, 4, 5, 6, 7]
NGC3193	30	[−3, 3, 5, 7, 8]
NGC3245	33	[−3, 3, 14, 58, 140, 185]
NGC3489	35	[−3, 3, 6, 10, 13]
NGC3607	28	[−3, 3, 9, 36, 100, 150]
NGC3608	27	[−3, 3, 6, 9, 11]
NGC3619	36	[−3, 3, 6, 12, 22, 30]
NGC3626	40	[−3, 3, 8, 25, 50, 76]
NGC3648	30	[−3, 3, 6, 9, 11]
NGC3665	40	[−3, 3, 8, 16, 50, 100, 250, 316]
NGC3945	34	[−3, 3, 9, 28, 45]
NGC4036	50	[−3, 3, 12, 48, 115, 170]
NGC4111	48	[−3, 3, 9, 25, 60, 96]
NGC4150	29	[−3, 3, 6, 14, 21]
NGC4203	78	[−3, 3, 15, 60, 96]
NGC4429	40	[−3, 3, 5.5, 9, 12.5]
NGC4459	40	[−3, 3, 8, 15, 22, 27]
NGC4526	30	[−3, 3, 10, 28, 50, 82]
NGC4643	29	[−3, 3, 5, 7, 8]
NGC4684	45	[−3, 3, 8, 24, 60, 77]
NGC4694	35	[−3, 3, 8, 18, 26]
NGC4710	28	[−3, 3, 9, 36, 72, 103]
NGC4753	40	[−3, 3, 4.5, 6.5, 7.5]
NGC5173	32	[−3, 3, 10, 25, 37]
NGC5273	20	[−3, 3, 5, 8, 9.75]
NGC5379	30	[−3, 3, 6, 12, 15]
NGC5866	44	[−3, 3, 6, 12, 52, 160, 282]
NGC6014	38	[−3, 3, 12, 28, 50, 70]
NGC6547	37	[−3, 3, 8, 18, 34, 47]
NGC6798	29	[−3, 3, 5.5, 7.5]
NGC7465	32	[−3, 3, 9, 36, 130, 250]
PGC029321	45	[−3, 3, 48, 130, 190]
PGC056772	28	[−3, 3, 9, 36, 72]
PGC058114	30	[−3, 3, 12, 50, 128, 198]
UGC05408	41	[−3, 3, 8, 24, 51, 62]
UGC06176	29	[−3, 3, 10, 42, 110, 158]
UGC09519	27	[−3, 3, 5, 7.5, 9.5]

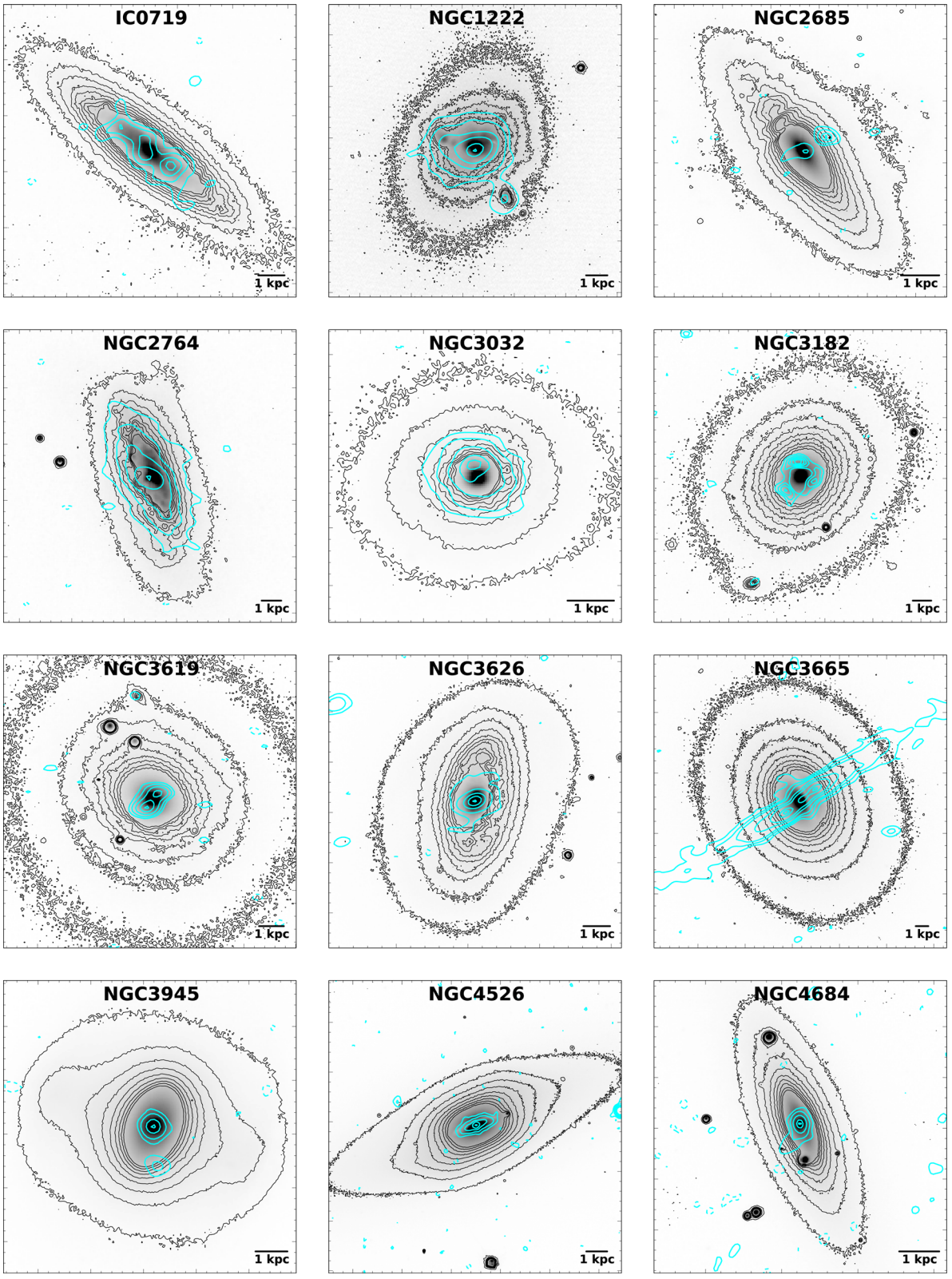

Figure B2. Optical r-band images (grey-scale and black contours) with 1.4 GHz radio continuum contours overlaid in cyan for the 19 well-resolved radio sources from our new VLA observations. The radio contour levels are the same as those shown in Fig. B1 and listed in Table B1.

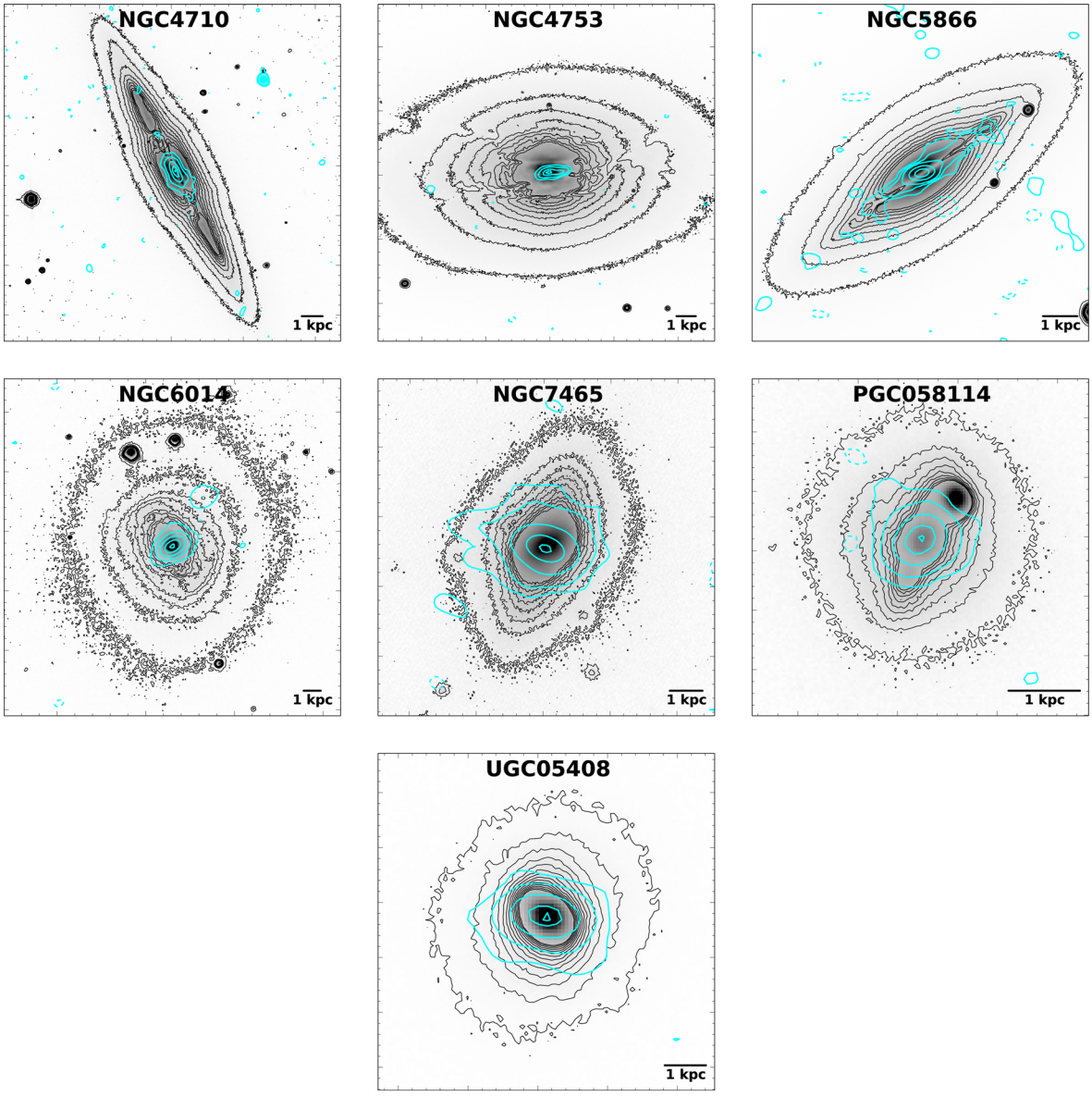

Figure B2 – *continued*

[1]*National Radio Astronomy Observatory, Charlottesville, VA 22903, USA*
[2]*Netherlands Institute for Radio Astronomy (ASTRON), Postbus 2, NL-7990 AA Dwingeloo, the Netherlands*
[3]*Physics Department, New Mexico Institute of Mining and Technology, Socorro, NM 87801, USA*
[4]*National Radio Astronomy Observatory, Socorro, NM 87801, USA*
[5]*School of Physics & Astronomy, Cardiff University, Queens Buildings, The Parade, Cardiff CF24 3AA, UK*
[6]*Sub-Department of Astrophysics, Department of Physics, University of Oxford, Denys Wilkinson Building, Keble Road, Oxford OX1 3RH, UK*
[7]*Observatories of the Carnegie Institution of Washington, 813 Santa Barbara Street, Pasadena, CA 91101, USA*
[8]*Kapteyn Astronomical Institute, University of Groningen, Postbus 800, NL-9700 AV Groningen, The Netherlands*
[9]*Observatoire de Paris, LERMA and CNRS, 61 Av. de l'Observatoire, F-75014 Paris, France*
[10]*European Southern Observatory, Karl-Schwarzschild-Str. 2, D-85748 Garching, Germany*
[11]*Sterrewacht Leiden, Leiden University, Postbus 9513, NL-2300 RA Leiden, the Netherlands*
[12]*Department of Physics and Astronomy, Macquarie University, Sydney, NSW 2109, Australia*
[13]*Australian Astronomical Observatory, PO Box 915, North Ryde, NSW 1670, Australia*
[14]*Physics Department, Reed College, Portland, OR 97202, USA*

This paper has been typeset from a TEX/LATEX file prepared by the author.